UNIVERSITÀ DEGLI STUDI DI PADOVA

Dipartimento di Territorio e Sistemi Agro-Forestali

TESI DI LAUREA IN Scienze Forestali e Ambientali

ANALYSIS OF VEGETATION DISTRIBUTION IN RELATION TO SURFACE MORPHOLOGY: THE CASE STUDY OF MIOZZA AND CETUS CATCHMENTS

Relatore

Prof. Paolo Tarolli

Correlatore

Prof.ssa Maria Cristina Rulli

Laureanda

Francesca Savio

Matricola n.

1015150

ANNO ACCADEMICO 2012/2013

"We may one day perhaps understand the self-organizing processes of a universe which is not determined by the blind selection of initial conditions, but has the potential of partial self-determination."

E. Jantsch, *The Self-Organizing Universe,* Pergamon, Oxford, 1980.

Riassunto

Gli attributi topografici sono in grado di descrivere accuratamente differenti morfologie di superficie, attribuendo particolare importanza alle analisi topografiche. In particolare, il rapporto di scala tra pendenza locale e area drenata, così come la relazione esistente tra curvatura media del profilo e area drenata, può fornire un'utile interpretazione dei principali processi morfologici. A questo riguardo, è importante tenere in considerazione l'influenza che su di essi ha l'attività biotica, che viene spesso esercitata dalla vegetazione mediante la capacità di modificare la stabilità dei versanti e i processi erosivi attivi su di essi. Ai fini di tale osservazione, sono stati considerati due bacini idrografici appartenenti ad aree geografiche differenti: il bacino alpino del torrente Miozza, localizzato nella regione carnica delle Alpi orientali, e il bacino del torrente Cetus, posizionato sulla costa tirrenica dell'Italia meridionale. Le aree di studio differiscono principalmente per altitudine, condizioni climatiche e requisiti di umidità, così da essere caratterizzate da un diverso tipo di vegetazione. Dati LiDAR ad alta risoluzione e topografia ottenuta da cartografia ordinaria, sono stati utilizzati per creare modelli digitali del terreno (DTMs) e derivare alcuni attributi topografici, come gradienti di pendenza, area drenata, esposizione, curvatura media, indice topografico, diagrammi logaritmici di pendenza-area drenata (S-A) e curvatura-area drenata (C-A). Sono state dunque analizzate le statistiche relative alla distribuzione della vegetazione in base a differenti modelli morfologici. I risultati hanno mostrato delle differenze nelle relazioni S-A e C-A per ciascuna tipologia di vegetazione, in riferimento alle caratteristiche ecologiche di ognuna. Entrambe le aree di studio hanno mostrato una distribuzione delle specie legnose maggiormente rivolta su pendenze maggiori, accompagnata da un incremento nei valori di pendenza che varia dalle praterie, alle zone arbustive e infine ai boschi. In aggiunta, è stato possibile individuare una corrispondenza tra le specie pioniere tipiche dei bacini alpini orientali e le aree dei versanti maggiormente soggette a fenomeni franosi.
Questa indagine preliminare suggerisce quindi che, laddove si possano utilizzare dati topografici ad alta risoluzione, l'analisi delle superfici può fornire un utile strumento di identificazione dei processi morfologici e del ruolo svolto dalla vegetazione sull'evoluzione del paesaggio.

Abstract

Topographic attributes are able to describe different surface morphologies, thus implying an increasing relevance in topographically-derived analysis. In particular, the scaling relationship between local slope and drainage area, as well as the curvature and drainage area coupling, has been found to provide a useful interpretation of the dominant landform processes. Within this contest, is also important to evaluate the influence of biotic activity on landforms, which often is exerted by vegetation through its role on slope stability and erosion dynamics. In such way, the distribution patterns relative to different types of vegetation are supposed to have some relations with surface morphologies. To the purposes of such investigation, two basins located in two different geographical areas have been considered: the Miozza basin, which is an Alpine headwater catchment in Carnia region of the Eastern Alps, and the Cetus basin, a Mediterranean coastal basin of the south-western Tyrrhenian coast. Differences in these study areas mainly consist in altitudinal ranges, moisture regimes and climatic conditions, thus influencing their vegetation characterization. High resolution LiDAR data and topography from conventional cartography provided support to derive Digital Terrain Models (DTMs) and topographic attributes of landscape morphology including slope gradient, drainage area, aspect, landform curvature, topographic wetness index, slope – area and curvature – area loglog diagrams. Statistics related to vegetation distribution and different morphological patterns have been analyzed.

The results reveal differences in the curvature-area and slope-area relationships for each vegetation type, according to their ecologies. In both basins, woody vegetation has been found to better distribute on steepest slopes, with a gradual increase in slope values from grasslands to shrublands and woods. Moreover, pioneer species typical of the eastern Alpine basins can be related to landslide-dominated regions through their specific distribution patterns.

This preliminary study suggested that, when high resolution topography is available, analysis on surface morphology provide a useful tool for better understanding the processes and the role of vegetation in landscape evolution.

Index

1 INTRODUCTION 9

1.1 The effectiveness of surface morphology 10

1.1.1 The role of vegetation on landscape morphology 13

1.2 Goals of the thesis 30

2 MATERIALS AND METHODS 33

2.1 LiDAR technology: overview and applications 33

2.2 Surface representation 39

2.3 Morphometric parameters 44

2.3.1 Aspect 45

2.3.2 Slope 47

2.3.2.1 Topographic slope 47

2.3.2.2 Local slope 49

2.3.3 Upslope drainage area 49

2.3.3.1 DEM depitting 50

2.3.3.2 Flow directions calculation algorithms 51

2.3.4 Specific Catchment Area 55

2.3.5 Landform curvature 55

2.3.6 Topographic Wetness Index 58

2.4 S-A and C-A relationships 59

2.4.1 Slope-Area relation 59

2.4.2 Curvature-Area relation 63

3 STUDY AREAS DESCRIPTION: THE MIOZZA AND CETUS CASE STUDIES 65

3.1 Miozza basin: general characteristics 65

3.1.1 Geological characteristics 67

3.1.2 Geomorphology of the basin 69

3.1.3 Climatic conditions 71
3.1.4 Vegetation and soil use description 72
3.2 Headwater catchment A 74
3.3 Headwater catchment B 76
3.4 Cetus basin: general characteristics 79
3.4.1 Geological characteristics 82
3.4.2 Geomorphology of the basin 83
3.4.3 Climatic conditions 83
3.4.4 Vegetation characterization of the study area 84
3.5 Analysis of surface morphology 91
3.5.1 Cetus basin 91
3.5.1.1 Procedure of data analysis 93
3.5.2 Miozza basin 97
3.5.2.1 Procedure of data analysis 99
4 RESULTS AND DISCUSSIONS 103
4.1 Cetus basin 103
4.2 Miozza basin 116
4.2.1 Study area A 117
4.2.2 Study area B 119
4.2.3 Comparison between the two study areas: differences among vegetation typologies 122
5 FINAL REMARKS 131
6 REFERENCES 133

1 INTRODUCTION

The state of the art in landscape morphology has shown that biological processes have a fundamental influence on land formation, as the biosphere is an integrant part of the continuously evolving ecosystem which develops all over the Earth's surface. Besides that, there is also a specific feedback between the alterations that living beings entail on their surrounding environment, in order to establish better conditions to their lives, and the physical laws they are, at the same time, exposed to. To this end, Reinhardt et al., (2009), define such bio-physical forms of co-evolution as "*feedbacks in which the physical environment regulates the numbers and types of organisms that can coexist in a community and shape the selective environment that drives evolution, while, at the same time, the organisms themselves modify the environment in a way that enhances their own persistence*". This statement can be useful to define the concept, reported by the same authors, of *ecosystem engineering* which expresses the species behavior to physically modify and create their habitat. Reinhardt et al. (2009) also noted that it is plausible for group of organisms that comprise biological communities to simultaneously cause and respond to a changing landform. This can be thought to as a scale-independent approach to a biophysical evolution of the landscape, which can be found both at the basin scale and at a global scale, even over the relatively short biologic timescale or the much longer geomorphic one. From here the necessity, particularly difficult and still far from being accomplished, of incorporating bio-physical, non-linear feedbacks into numerical, physical and conceptual models (Reinhardt et al., 2009).

Such a foreword can be inserted in the context of the "evolutionary geomorphology" approach proposed by Phillips (2006) to study surface processes and landforms, which recognizes multiple possible historical pathways rather than an inexorable progression toward some equilibrium state or along a cyclic pattern (Corenblit and Steiger, 2009). The term "evolutionary" is supposed to recall the non-linear behavior of natural selection, prone to dynamic instability and deterministic chaos and sensitive to initial conditions and perturbations. In this new field of investigation, vegetation represents a major component since it can be considered as the most important biotic agent on the Earth surface. This is well explained in a commentary paper by Corenblit and Steiger, 2009. The authors argue that, in a simplified model where geomorphic forces are controlled only by chemical and physical

factors and the only energy sources are gravity and solar energy, which control sediment transport processes and the endogenic geothermal activity, as well as tectonic uplift, vegetation is capable to convert solar energy into geomorphic forces. Vegetation produce both biomechanical and biochemical impacts on rocks, sediment and soil dynamics and also represents the only source of energy for nearly all organisms, letting them further influence biogeomorphic processes through their *engineering* activities (Butler, 1995). In this perspective, the elemental biological process of photosynthesis is the fundamental trigger of the shift from abiotic geomorphology toward biotic biogeomorphic dynamics on the Earth surface.

In such context, this work is aimed to investigate the role of vegetation distribution over the landscape, giving particular attention to identify possible relations between the disposition of different vegetation patterns, referring to various vegetation types, and the descriptive parameters of surface morphology. To what concerns vegetation distribution, it is highly recognized the role played by the elevation in furnishing the altitudinal conditions specific to each forest type, but many others morphological features take an effective part in generating environmental conditions. From the fundamental ecological point of view, the highest influence on vegetation distribution is exerted by water and nutrients availability, besides solar energy radiated (Stephenson, 1990; Poorter and Nagel, 2000; Gerten et al., 2004). Certainly, these ecological factors are strictly related to surface morphology since parameters as aspect, local slope and landform curvature directly control the shape of the landscape, thus creating great variability of ecosystem dynamics through different environments.

1.1 The effectiveness of surface morphology

Investigations involving both landscape ecology and geomorphology have always been based on topographical analysis. This is because topography can be considered one of the most important issues for the evaluation of hydro-geomorphological processes. Respect to previous topographic survey techniques, the recent development of remote sensing have given a strong contribution to topographic analysis, by supporting the digital representation of surface morphology and the extraction of its morphometric parameters. Researches on different fields as hydrology, geology, geomorphology, landscape and forest management, shear the common base of a high-resolution digital surface representation, that allows numerical computations

and modeling to accomplish their purposes. Digital Terrain Models (DTMs), Digital Surface Models (DSMs) and Triangulated Irregular Network (TIN) are the most widespread types of surface representation. They result from the elaboration of digital elevation data that can be collected by different remote sensing systems such as the Terrestrial Laser Scanner (TLS), Airborne LiDAR (Light Detection And Ranging), Shuttle Radar Topographic Mission (SRTM), Synthetic Aperture Radar (SAR) and the Advanced Spaceborne Thermal Emission and Reflection Radiometer (ASTER) technologies. Their applications have been stressed in many studies, which have been collected by Tarolli et al. (2009) and Tarolli and Cavalli (2013) to provide the scientific community with a comparison among different topographic data collection approaches. Moreover, Pirotti et al. (2013) presented a review about the state of the art of terrestrial and aerial laser scanner sensors with a critical discussion about quality of the surveyed dataset. The importance of accuracy for high resolution topographic surveys has been analyzed in terms of the factors that influence positional accuracy, range, point density and quality of the final product (Tarolli and Cavalli, 2013). The interpolation and subsequent elaboration of topographic data collected are usually carried out through the use of a GIS (Geographic Information System) software. Godone and Garnero (2013) analyzed different algorithms, usually available in GIS environment, with the aim to point out an optimal interpolation methodology and to define, by classification techniques, which morphological variable affects more the interpolation quality. Their classification has drawn the attention to surface roughness as the main factor affecting interpolation accuracy. High resolution topographic data can be processed in order to obtain, from bare elevation data, topographic attributes of a certain surface, very useful to numerical modeling. With a focus on geomorphology, topographic signatures of different erosion processes can be identified by specific analysis carried out through the use of high resolution topographic data. Topographic attributes were classified by Moore at al. (1991, 1993) as primary and secondary attributes by describing the former as directly derived by a DEM, while the latter as computed through the use of primary attributes. In particular, local slope and upslope drainage area (Willgoose et al, 1991, 1994; Ijjasz-Vasquez and Bras, 1995), but also landform curvature (Lashmers et al., 2007; Istanbulluoglu et al. 2008; Tarolli and Dalla Fontana, 2009), have a fundamental relevance in the investigation over erosion dynamics.

The relation between local slope and drainage area was deeply explored by Montgomery and Foufoula-Georgiou (1993), who suggested a partitioning of the landscape into drainage and

slope regimes that can be directly estimated from DEMs. The authors critically examined two different methods used to identify the extent of channel network and to simulate network sources in DTMs. The *constant threshold area* method (O'Callagan and Mark, 1984; Band, 1986; Mark, 1988; Tarboton et al., 1991), which assumes the channel heads to be representative of the transition in the dominant sediment transport process, was found to be more appropriate to depict the hillslope to valley transition than to identify channel heads. Conversely, the *slope-dependent critical support area* method (Dietrich and Dunne, 1993; Montgomery and Dietrich, 1994), assuming that channel heads represent an erosional threshold, was depicted as to be more appropriate to define the extent of channel network in soil-mantled landscapes. Additionally, relations between local slope and drainage area derived from DEMs showed two distinct inflection points, that allowed the authors to develop a schematic illustration of the slope-area plot showed in *Figure 1.1*.

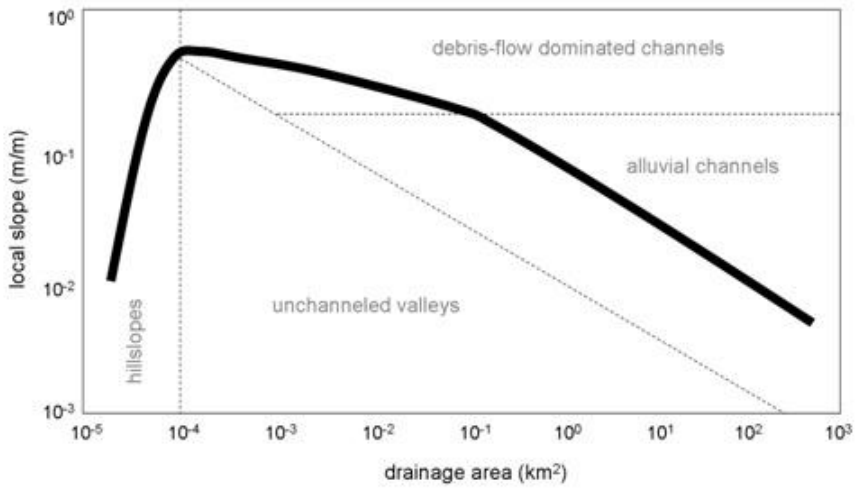

Figure 1.1 - Schematic illustration of relations between drainage area and local slope depicting hillslope to valley transition and the channel initiation criteria (Montgomery and Foufoula-Georgiou, 1993).

The first inflection point characterizes the hillslope to valley transition and it has been proven to coincide to the transition from divergent to convergent topography. At the same time, the second inflection point shows a correspondence to the transition from debris-flow dominated channels to alluvial channels. The authors also stated that "*the boundary between unchanneled valleys and fluvial channels is defined by slope-dependent threshold that reflects both critical shear stress and climate*" (Montgomery and Foufoula-Georgiou, 1993).

Another morphometric parameter used for the interpretation of dominant erosion processes is the landform curvature (i.e. Laplacian of elevation z, $C = \nabla^2 z$), composed by both the planar curvature and profile curvature (Gallant and Wilson, 2000; Lashermes et al., 2007;

Istanbulluoglu et al., 2008). Through the analysis of this parameter, hillslope diffusive processes are associated to the convex-divergent landforms, while fluvial-dominated processes are associated to concave-convergent profiles. Recently, landform curvature has also been used as part of an objective methodology for channel network extraction, which is based on threshold values for curvature calculated as multiplies of standard deviation of curvature (Tarolli and Dalla Fontana, 2009; Pirotti and Tarolli, 2010). Furthermore these researches have given the chance to explore the utility of different resolution topographic data. The analysis of the slope-area relations over DTMs of different resolutions (1 to 30 m), to determine the change in the dominant geomorphic process and to detect the channel head location throughout its scaling regimes, led to reliable results in the case of DTMs finer than 5 m; high resolution DTMs are required to obtain curvature values to depict convergent hollows as well (Tarolli and Dalla Fontana, 2009). Conversely, DTMs just as fine as 10 m allow to recognize topographic signatures of debris flow and landslides erosion from the slope-area diagram. This resolution was found to be optimal also for the comparison of most likely landslide initiation point density ratios (Tarolli and Tarboton, 2006**)**. The individuation of the appropriate data resolution needed is certainly a key issue for geomorphologic researches. In general terms, the more accurate the data are, the more can be easy to detect specific processes with reduced uncertainties. It is also important to keep in mind that high resolution topography requires the use of quite expensive technology, besides higher cost and time consuming data elaborations. Therefore it is always beneficial to well identify the correct level of detail supported by the model that it is going to be applied, prior to data collection, thus avoiding worthless resources consumption.

1.1.1 The role of vegetation on landscape morphology

The linkage between vegetation and geomorphology has been deeply stressed since the early nineteenth century when Alexander von Humboldt (1769-1859) explored the Andes in Colombia, Equador and Peru to observe the influence of elevation, climate and slope on vegetation and land use. Charles Darwin investigated how plant distribution changes are affected by geologic events and he also recognized that climate change exerts a greater influence on vegetation than landforms, processes and earth materials do, but he rarely mentioned how plant distributions were affected by geological attributes (Kruckeberg, 2002). Even other researchers as Clements (1928) and Cain (1944) in North America and Braun-

Blanquet (1932) in Europe confirm climate as the primary variable affecting plant distribution (Marston, 2010). However, vegetation was considered to be totally dependent on geomorphic processes until the half of the past century, when Hack and Goodlett (1960) published their paper "*Geomorphology and forest ecology of a mountain region in the central Appalachians*". They found out a positive relationship between topographic position, moisture regime and prevailing forest type. After Hack and Goodlett's work, many other authors addressed their researches toward the complex and interdisciplinary field of the interactions between vegetation, hydrology and landscape development. As well, many other studies reveal the existence of a complex relationship between climate and sediment yields, modulated by vegetation (Langbein and Schumm, 1958; Wilson, 1973; Istanbulluoglu and Bras, 2005); as a consequence, this complexity is reflected on the issue of formulating landscape models which can include the biotic influence. Analyzing these relations means to get involved into vegetation-erosion coupling, vegetation control over topography, sediment transport processes and all the relative dynamics and implications over the landscape.

Besides the more commonly known ecological control of vegetation on biodiversity in animal and plant communities, microscopic life forms, habitat and ecosystems characterization, soil production and protection, carbon dioxide retention, hydrologic cycle, atmospheric composition and climatic conditions, a lot is still to study about its geomorphic functions. Marston (2010) proposed a summary table on the key geomorphic functions created by vegetation on hillslopes that it is worth to be reported here in *Table 1.1*.

Table 1.1 - Main geomorphic functions implemented by vegetation on hillslopes (Marston, 2010).

Processes	**Selected examples**
Modify soil moisture, through interception loss and transpiration, controlling mass movement.	(Haneberg, 1991; Harden, 2006)
Leaves and litter intercept raindrops, dissipating erosive energy.	(Walsh and Voight, 1977; Parsons et al., 1996; Marston and Dolan, 1999; Keim and Skaugset, 2003)
Organic matter in the soil increases water storage, infiltration, and percolation thereby promoting vegetation growth and inhibiting erosion.	Bryan (2000)
Roots bind soil against piping, land surface erosion, and shallow mass movement.	(Greenway, 1987; Wu et al., 1988; Riestenberg, 1994;Schmidt et al., 2001; Roering et al., 2003)
Aboveground biomass creates micro-topography on land surface that affects overland flow; roughness in the profile direction (upslope–downslope) slows overland flow; roughness along the contour concentrates sheetflow into rillflow, rills into gullies.	(Parsons et al., 1992; Abrahams et al., 1995; Wainwright et al., 2000; Stavi et al., 2009)
Aboveground biomass creates hydraulic roughness against overland flow.	Abrahams et al. (1994, 1995)
Treefall exposes soil for erosion.	Gabet et al. (2003)

Going deeply in detail, Sidle and Ochiai (2006) summarized some of the main effects of woody vegetation on slope stability, classifying them as beneficial or adverse to stability on the basis of their influence on shallow or deep-seated landslides. According to this classification, hydrological mechanisms such as interception of rainfall and snow by tree canopies and root system extraction of water from the soil are helpful to slope stability. The former promotes evaporation, thus reducing water available for infiltration, while the latter leads to lower soil moisture levels. Conversely, a negative influence on slope stability is due to an increase of soil infiltration capacity, owing to an intensified ground surface roughness and more frequent desiccation cracks caused by the depletion of soil moisture. Additionally, mechanical processes such as soil cohesion due to root reinforcement, the increase in soil shear strength, tie mechanisms across planes of weakness of potential landslides, are all supplementary reinforcements to slope stability from woody vegetation. However, the presence of trees allows the transmission of wind dynamic forces to the soil mantle and the weight of trees increases both the normal and downhill force components. However, both mechanical and hydrological processes affected by vegetation contribute to shape the landscape morphology.

In his study on vegetation influences on landforms, Kirkby (1995) states that "*vegetation is the most important intermediate through which climate and land use modify geomorphic processes and landforms*" and that "*for uncultivated areas, the indirect effects of this [climate change mediated by vegetation] are more important that direct effects*". It is also undeniable the control that vegetation cover plays over hydrologic processes, since the partition between surface and subsurface runoff is strongly influenced by vegetation, and in turns strongly influences sediment transport rates (Kirkby, 1995). The author explored three types of models to simulate the relationships between vegetation, climate and erosion rates for a fixed topography and soil cover, taking also into account longer term interactions with soil properties and finally looked at geological time spans finding a response in the pattern of erosion rates to differences in vegetation and landforms. Some of the main linkages connecting landscape form to vegetation, which are at the basis of Kirkby's models, are shown in *Figure 1.2*.

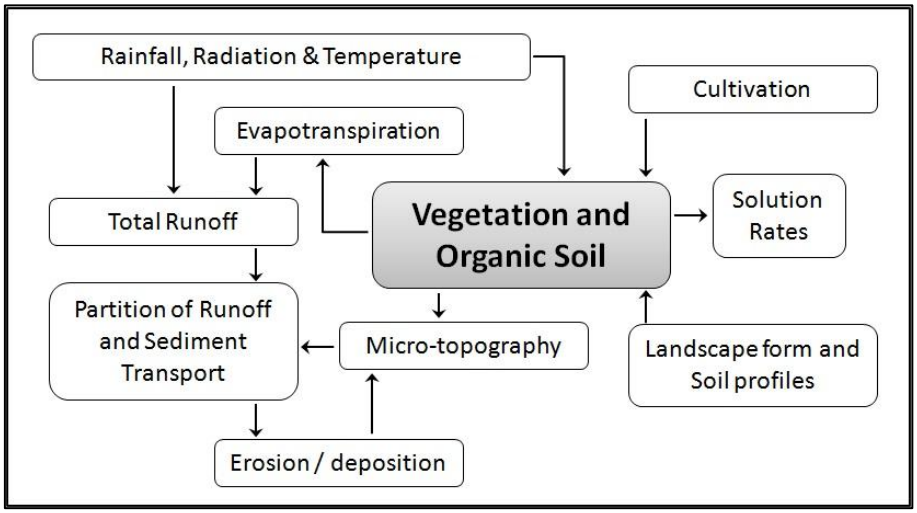

Figure 1.2 - Climate, hydrology, vegetation and lanform connections. (Kirkby, 1995)

In addition, at a larger scale, vegetation distribution also affects atmospheric and climatic conditions influencing heat transfer, evapotranspiration and water transport; this important relationship has been investigated through a simulated comparison between the two extreme situations of a "desert world" versus a "green planet" by Kleidon et al. (2000), which found out that the removal of vegetation leads to large changes in mean annual precipitations over extensive geographic regions. The same authors commented their study emphasizing the great value of their approach to land surface parameters which are not considered as independent of each other but mainly as quantities representing different aspects of vegetation, also including biosphere-atmosphere feedbacks. According to this, Dietrich and Perron (2006) added a further observation suggesting that, as erosion is positively correlated to precipitation, the biotic influence on precipitation patterns affects the height, width and symmetry of mountain ranges. To better comprehend this correlation, it is necessary to mention some recent studies which have suggested an existing relation between erosion, climate and the orogeny of mountain belts (Willet, 1999; Hilley and Strecker, 2004; Whipple and Meade, 2004, Dietrich and Perron, 2006). As already known, plate tectonic leads the continental crust to thicken at convergent plate boundaries, with a resulting uplift of the land surface and a steepening of the regional topographic gradient. This landform formation has been found to influence local climatic conditions in such way to determine an uneven distribution of precipitation and, as a consequence of the existing positive correlation between erosion and precipitation, the wetter sides of mountains will erode more rapidly, accelerating the uplift of the underlying bedrock, altering the force balance across the collisional zone (Dietrich and Perron, 2006). In this

perspective, vegetation is thought as indirectly affecting the shape of mountain ridges, by influencing the pattern of precipitation. Furthermore, relating this concept to the numerical simulation of vegetation-climate system by Kleidon et al. (2000), it can be assumed that the near-surface air temperature change experienced in the "green-planet" case (by setting the model on the extreme case of maximum vegetation), may increase erosion rates in high mountain areas, due to the freeze-thaw activity. This surely strengthens the hypothesis of an influence of biotic processes on long-term landscape evolution. Conclusions carried out by Dietrich and Perron (2006) suggest that even though it still can't be found a unique topographic signature of life on Earth, an analysis of frequency distributions on certain land properties has been found to show a significant difference between biotic and abiotic environments. Many studies on landscape evolution (Istanbulluoglu and Bras, 2005; Howard, 1994; Tucker and Bras, 1998; Dietrich et al., 2003; Willgoose, 1994; Dietrich and Perron, 2006) have focalized their attention on the analysis of the slope-area relationship (which will be better explained later in this work) and have shown that slopes generally steeps with increasing drainage area on hillslopes and become more gentle with increasing drainage areas in valleys, with higher slope values occurring at the hillslope-valley transition. In particular, Dietrich and Perron (2006) examined the slope-area curve of three landscapes (one with a significant biotic influence on erosion processes and two with a minimal biotic influence) and noted that "*the slope-area properties of the biotically-influenced landscape clearly differ from those of the landscape with minimal biotic influence*"(*Figure 1.3*).

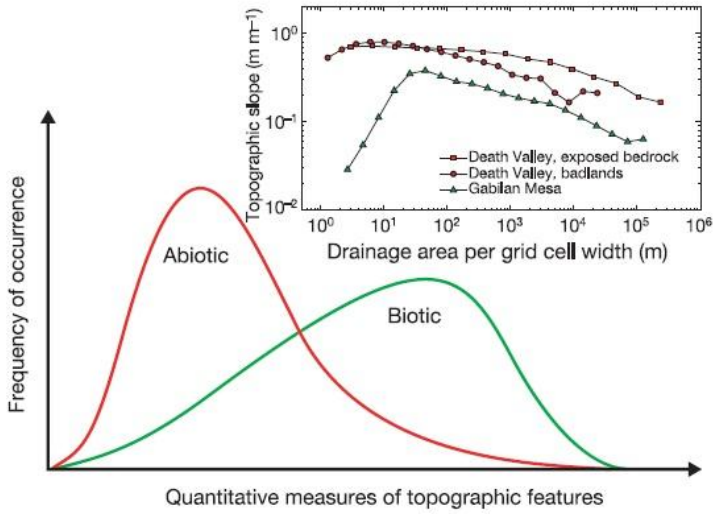

Figure 1.3- Hypothetical frequency distributions of landform properties for the present Earth and an abiotic Earth. Whereas the same range of landform types would probably be present in both, the frequency distributions of measurable landform properties (such as mountain height, steepness or curvature; the sinuosity of rivers; the extent

of the landscape with a soil mantle; slope–area characteristics) might differ. Inset, relationships between slope (the magnitude of the topographic gradient) and drainage area per grid cell width for three landscapes. Biotic processes are of minimal erosional importance in areas of badlands and exposed bedrock in Death Valley, California, but are significant in the Gabilan Mesa, California. Areas sampled are 2.7 km^2 for Death Valley bedrock, 0.24 km^2 for Death Valley badlands, and 5.8 km^2 for the Gabilan Mesa (Dietrich and Perron, 2006).

However, even acknowledging the profound influence of life on geomorphic features and landscape evolution, Dietrich and Perron's research of a unique topographic signature of life (i.e. a landform that could only exist in presence of life) leds to the conclusion that this sign cannot be represented by a diagnostic landform, whereas it may only be detectable in a more subtle exploration of landform properties that includes their frequency of occurrence and scale-dependence. This observation was successively reviewed by Corenblit et al. (2008) who pointed out that "*geomorphic signatures of life are complex and of multiple kinds on the Earth's surface and may encompass to a certain extend unique geomorphic patterns and dynamics at various scales*".

However, in their review Dietrich and Perron (2006) highly recommend the development of new geomorphic models that may explicitly include biotic processes, trying to go deeply through the initial experiments of this kind, such as researches from Howard (1999), Roering et al. (2004), Collins et al. (2004) and Istanbulluoglu and Bras (2005). Results from these researches suggest that vegetation can affect landscape form by changing the dominant erosion process from overland flow under abiotic conditions to landsliding in well-vegetated states. In order to better comprehend this concept, it is worth to briefly report the main issues of some of these studies.

Of particular interest is the investigation made by Collins and Bras (2004) over the effects of vegetation-erosion coupling. They approached the numerical simulation of vegetation-erosion dynamics through the use of the “Channel Hillslope Integrated Landscape Development" (CHILD) model (Lancaster, 1998; Tucker and Bras, 1999, 2000; Tucker et al., 2001a, 2001b). This model imitates landscape evolution by simulating discrete rainfalls events, routing the runoff through an elevation field, and deforming this field according to an interplay of various geomorphic processes (Collins and Bras, 2004). Their investigation found an evidence of vegetation-dominated erosion in the topographies of the *Bare* and *Basic* simulations. This study shows that "*vegetated landscape has greater relief and is dissected less than its barren counterpart*" (*Figure 1.4-A*). Furthermore, the slope-area plots relative to these simulations show a greater interception of the fluvial slope-area portion and a greater hillslope length for the vegetated simulation (*Figure 1.4-B*). The authors's analysis of the S-A relationships

indicate that higher and steeper slopes result from higher shear stress due to protective vegetation ($\tau_{c,v}$) and species-dependent vegetation erodibility parameter (K_v) respectively, and no discernible differences arise from variation of T_v (presented in the paper as the time taken for a plant to grow to a stage where it can noticeably limit erosion, which is distinct from the time until maturity or average height). In this analysis the parameter $\tau_{c,v}$ is considered as the species- or community- dependent variable to be multiplied by local vegetation density (V) in the following *Equation 1.1*, expressing the critical shear stress (τ_c), where the term $\tau_{c,s}$ is the shear stress due to the soil alone and it's assumed to be constant. The parameter V is the state variable used to describe vegetation and it ranges from 0 to 1, representing the proportional coverage at or near to ground level.

$$\tau_c = \tau_{c,s} + V\tau_{c,v} \quad 1.1$$

Within this analysis, vegetation growth is modeled with a logistic equation (*Equation 1.2*), in which growth rates are small both at low density (reproduction limited) and at high density (resources limited). For this reason, the equation only simulates the competition for space, through the use of the parameter T_v, to express the time needed to a vegetation community to grow till it can be able to avoid erosion. Since the plant type considered were grasses and small shrubs, T_v, varies over 1, 2, 3, 5, 10 (years). Vegetation growth is expressed by the following equation:

$$\frac{dV}{dt} = \frac{1}{T_v}(1 - V) \quad 1.2$$

For the sake of simplicity, vegetation loss was only related to fluvial erosion, so that a linear dependence on excess shear stress can be used to model it (*Equation 1.3*).

$$\frac{dV}{dt} = \begin{cases} -K_v \cdot V(\tau - \tau_c) : & \tau > \tau_c \\ 0 : & \tau \leq \tau_c \end{cases} \quad 1.3$$

K_v is a species-dependent erodibility parameter, whose experimental values are supposed to assume values equal to 0.1, 0.5, 1, 5, 10 (Pa^{-1} yr^{-1}).

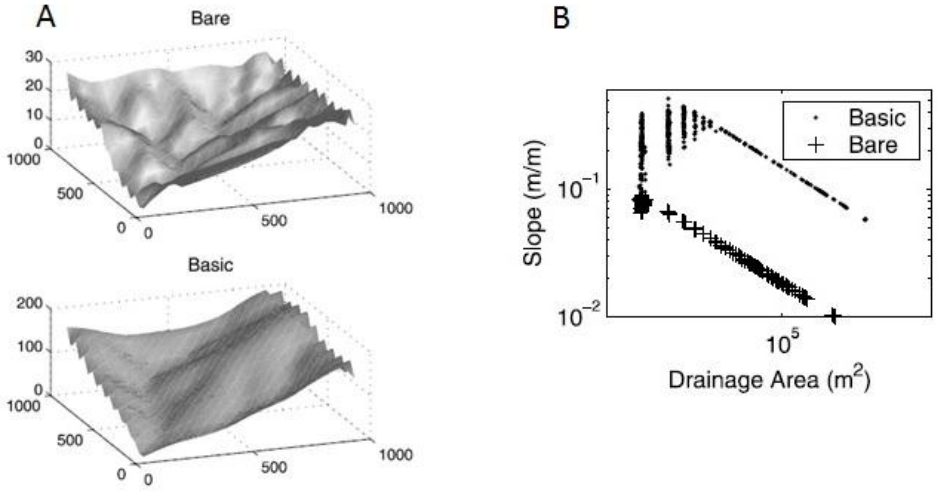

Figure 1.4 - A. Equilibrium basins of the unvegetated Bare and vegetated Basic simulations; B. slope-area (S-A) relationship for the equilibrium Bare and Basic landscapes (Collins and Bras, 2004).

Results from Collins and Bras (2004), coming through 14 simulations set on the three vegetation parameters analyzed ($\tau_{c,v}, T_v, K_v$), indicate that vegetation allows landscapes to become steeper but at the expense of an increase of erosion events variability; vegetation also reduces drainage density and highlights the transient and variable nature of erosionally active channel extent. Based on these findings from Collins and Bras (2004), Istanbulluoglu and Bras (2005) investigated the effects of vegetation on landscape development. They derived analytical expressions for channel initiation by overland flow and landsliding for hillslopes in equilibrium, then investigated the sensitivity of channel head source area and drainage density to steady state erosion, runoff rate and vegetation cover. Finally, they also performed some simulations using the CHILD model (Lancaster, 1998; Tucker and Bras, 1999, 2000; Tucker et al., 2001a, 2001b) to investigate the effect of vegetation cover on landscape evolution.

Istanbulluoglu and Bras (2005), firstly examined the theory that relates water erosion, sediment transport, hillslope diffusion and landsliding to vegetation cover. To evaluate the effects of vegetation on effective shear stress, they assumed F_τ as the shear stress partitioning ratio, written as a function of Manning's roughness coefficient for bare soil and vegetation (*Equation 1.4*). Roughness due to a particular vegetation (*Equation 1.5*) can be parameterized as a power function of its ground cover fraction relative to a reference vegetation, V_R, which has a known roughness coefficient n_{vR}, according to Istanbulluoglu et al. (2004).

$$F_\tau = \left(\frac{n_s}{n_s + n_V}\right)^{3/2} \qquad 1.4$$

$$n_V = n_{VR}\left(\frac{V}{V_R}\right)^{\omega} \quad 1.5$$

On the basis of this assumption, hydraulic radius, R_t, equivalent to flow depth for overland flow, and effective shear stress, τ_f, are written as functions of vegetation cover fraction respectively as in *Equation 1.6* and *Equation 1.7*:

$$R_t = \left(n_s + n_{VR}\left[\frac{V}{V_R}\right]^{\omega}\right)^{6/10} q^{6/10} S^{-3/10} \quad 1.6$$

$$\tau_f = \frac{\rho_w g n_s^{1.5}}{\left(n_s + n_{VR}\left[\frac{V}{V_R}\right]^{\omega}\right)^{9/10}} q^{6/10} S^{7/10} \quad 1.7$$

where q is unit discharge, S is slope, ρ_w is water density and the parameter ω quantifies the dependence of vegetation roughness to surface vegetation cover.

Furthermore, Istanbulluoglu and Bras considered the dependence of hillslope diffusion to slope gradient as represented in *Equation 1.8* by Howard (1994, 1997) and Roering et al. (1999, 2001).

$$q_{sd} = \frac{K_d S}{1-(S/S_c)^2} \quad 1.8$$

Equation 1.9 relates the diffusion constant, K_d, to surface vegetation cover according to an exponential function:

$$K_d = K_b[e^{-\alpha V}] \quad 1.9$$

where K_b is a baseline diffusion constant (L^2/T), α is an empirical parameter and the term in brackets is an adjustment factor that accounts for the influence of vegetation on soil creep processes.

About landsliding initiation, the authors reported the infinite slope stability equation in the form of a critical slope threshold that depends on drainage area, by equating *FS = 1*, and solving for slope:

$$S_c = \frac{C_r' V}{cos\theta} + tan\varphi\left[1 - \rho_w/\rho_s\, min\left(\Gamma\frac{A}{S}, 1\right)\right] \quad 1.10$$

where, C_r', is mature root cohesion for complete vegetation cover normalized to soil weight ($C_r' = C_r/h_s\rho_s g$), and Γ is a hydrology parameter that is the ratio of steady state precipitation rate to soil trasmissivity ($\Gamma = P/T$), or the inverse of saturated threshold. By multiplying C_r' for *V*, the authors assumed that total root cohesion in a hillslope parcel is linearly proportional to surface vegetation cover.

Finally, *Equation 1.5*, which relates vegetation roughness to vegetation cover, was tested on data already published by Prosser et al. (1995), showing that resistance due to vegetation can contribute in reducing flow velocity and that on vegetated surfaces a greater fraction of the shear stress is exerted on vegetation than on soils, reducing the detachment potential of water. This finding provided a way to relate erosion potential to vegetation cover.

Additionally, Istanbulluoglu and Bras (2005) also developed analytical expressions to quantify channel head source area size for runoff erosion and landsliding for hillslopes in equilibrium (i.e. when erosion is in balance with tectonic uplift), in order to evaluate its response to changes in vegetation cover. They assumed, for a steady-state basin, that the water discharge can be calculated as a function of unit contributing area, *A*, and effective runoff, P_e:

$$q = P_e A \tag{1.11}$$

and that the relationship between hillslope gradient and contributing area can be obtained by equating sediment production to hillsope sediment transport:

$$UA = K_d S \tag{1.12}$$

where *U* is the steady state erosion rate (equal to tectonic uplift), and *A* is unit contributing area. *Equation 1.13* gives the equilibrium hillslope gradient as:

$$S_{eq} = U_* e^{\alpha V} A \tag{1.13}$$

where U_* is the ratio of steady state erosion rate to bare soil diffusivity ($U_* = U/K_b$) referred to as hillslope steepness index, and the term $e^{\alpha V}$ is due to the substitution of *Equation 1.9* into *Equation 1.12* to represent the effects of vegetation on soil creep. According to these conditions, the source area for runoff erosion (A_R) can be thought to as the point at which the hillslope gradient becomes steep enough so that overland flow shear stress is greater than or

equal to the erosion threshold. This can be defined by substituting *Equation 1.11* and *Equation 1.12* into *Equation 1.7*, setting it equal to the erosion threshold (τ_c) and finally solving for *A* to obtain:

$$A_R = \left[\frac{\tau_c \left(n_s + n_{VR} \left(\frac{V}{V_R} \right)^{\omega} \right)^{9/10}}{\rho_w g n_s^{1.5} P_e^{6/10} (U_* e^{\alpha V})^{7/10}} \right]^{\frac{1}{0.6-0.7}} \qquad 1.14$$

Thus, setting some other conditions, Istanbulluoglu and Bras (2005) found out that valley formation by threshold landsliding begins in unsaturated portions of the landscape with a source area expressed by *Equation 1.15*.

$$A_L = U_*^{-1} \tan \phi \left[1 - \frac{\rho_w}{\rho_s} \Gamma U_*^{-1} \right] \qquad U_* > \Gamma \qquad 1.15$$

where A_L is the area at which equilibrium hillslope gradient becomes just steep enough for the initiation of pore pressure activated landsliding.

Results from this analysis suggested that when vegetation does not influence hillslope diffusion, source area is positively related to vegetation cover as a response to reduced efficiency of flow shear stress and increased slope-area threshold for landsliding; this implies a negative relationship between drainage density and vegetation cover. Whereas, when vegetation inhibits hillslopes diffusion, the model shows that source area may increase or decrease depending on the relative influence of vegetation in altering diffusion rates. A reduction in the source area (or increase in drainage density) with increasing vegetation cover occurs when hillslope gradients tend to steepen rapidly to cope with the constant rate of tectonic uplift under reduced hillslope diffusivity, caused by vegetation. Moreover, since source area was known to have an important implication on the structure of drainage basins (Moglen et al., 1998), the authors found useful to plot source area for runoff erosion and landsliding, both normalized to the mean of the latter, and also drainage density, normalized to its mean value, as functions of vegetation cover under high, moderate and low values of hillslope steepness index. Of particular interest resulted to be the intermediate case, in which the variation in the vegetation cover produces a shift in the dominant erosion process controlling the valley head position. This suggests that a runoff erosion-dominated landscape under poor vegetation cover may be landslide dominated under a denser cover. Finally, in

their numerical simulation, Istanbulluoglu and Bras (2005), investigate the long-term consequences of vegetation-erosion dynamics on landscape morphology, through the use of the CHILD model (Lancaster, 1998; Tucker and Bras, 1999, 2000; Tucker et al., 2001a, 2001b), using parameter values for tectonic forcing, vegetation and soils representative of the Oregon Coast Range. The first two simulations consider the end member case: bare soil (*Figure 1.5-A*), and full vegetation cover (*Figure 1.5-B*) on the landscape, with no vegetation disturbances driven by floods, erosion or fires; while the third simulation (*Figure 1.5-C*) analyzes dynamic vegetation disturbed by runoff erosion and landsliding. Consistent with the theory previously presented by the authors, all the numerical simulation were performed under conditions of constant uniform uplift.

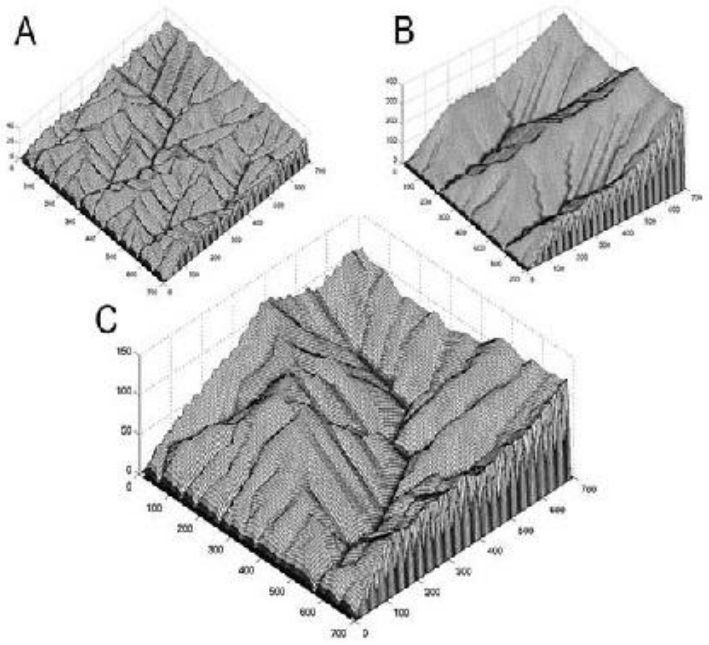

Figure 1.5 - Numerical simulations showing the contrasting differences in landscape morphology under conditions of constant uniform uplift and different vegetation cover (Istanbulluoglu and Bras, 2005).

In the first simulation (A), in absence of vegetation, rainstorms generate high erosion rates, forming a highly dissected, low-relief topography, while in the simulation which considers the opposite condition (B), static vegetation protects the soil surface from runoff erosion. In the third simulation with dynamic vegetation cover (C), the outcome of vegetation-erosion coupling is a more highly dissected topography, with smaller landslide-dominated hollows entering the channel network. The authors also noted that in the case of static vegetation cover, the landscape is landslides dominated, it consists of mostly planar hillslopes and has a higher relief and a significantly lower drainage density. This is due to the fact that, being

water erosion very rare under vegetation cover, continuing uplift and consequent slope steepening bring slopes to a point that they predominantly erode by landsliding (Istanbulluoglu and Bras, 2005). The difference in the dominant erosion process is reflected on the slope-area diagram, which is reported in *Figure 1.6*.

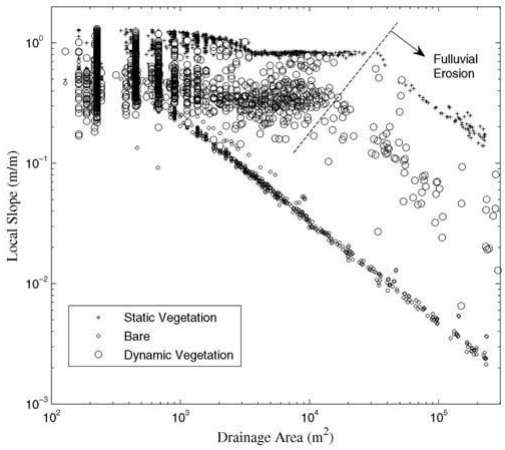

Figure 1.6 - Slope-area (S-A) relation for the simulated landscapes in *Figure 1.5* (Istanbulluoglu and Bras, 2005).

The three surface cover conditions were analyzed by the authors considering the hillslope to valley transition to occur where the rate of soil removal by runoff erosion is higher than infilling by hillslope diffusion. In the bare surface condition, runoff shear stress is completely exerted on the soil surface, generating frequent erosion, even in the upper portion of the simulated catchment. Whereas, in the case of static vegetation, this condition almost entirely avoids runoff erosion and continuing uplift allows the increase of elevation until slopes exceed the critical threshold for landsliding (according to *Equation 1.10*). The flat region on the slope-area diagram of the fully vegetated condition (*Figure 1.6*) extents to the point where the threshold gradient for landslides is equal to the equilibrium gradient for water erosion, below which concave channels begins. This process can be easily distinguished in *Figure 1.5-B*, where straight channels drain large hillslopes segments and flow into the main channels in the valley bottoms. The slope-area data outcoming from the dynamic vegetation cover show significant scatter and are bounded by the plots of bare and static vegetation. In this simulation, landslide-dominated hollows erode in a self-driven cycle of slope steepening and consequent landsliding (Dietrich et al., 1986; Istanbullluoglu and Bras, 2005). Moreover, comparing the fluvial sections of the bare and static vegetation cases, can be clearly seen that, for a given contributing area, equilibrium slopes are significantly larger in the latter case. While, for the dynamic vegetation cover plot, both in hillslopes and channel portions, slopes are lower than for the fully vegetated landscape. Thus, vegetation disturbances resulted to be

of fundamental importance on landscape morphology contributing to the formation of an highly dissected topography with less steep slopes. This also reduces the variability of erosion events which is directly related to greater hazard and management costs. Finally, a fourth simulation was performed by the authors submitting the dynamic vegetation condition to both geomorphic and wildfire disturbances. Results showed an increase of drainage density and a reduced basin relief.

Numerical modelling of the effects of coupled vegetation-erosion dynamics on long-term landscape evolution indicated that the presence of vegetation not only mitigates erosion and sedimentation, but also controls local topography. To this regard, topographic evolution of a landscape is strongly related to the geomorphic processes acting on it, which are in turns influenced by land surface properties that characterize such landscape. These are subject to a natural variation in space and time particularly linked to climate changes. To this regard, a noteworthy paper by Yetemen et al. (2010) examined the relationship between land surface properties such as soil, vegetation and lithology, and landscape morphology. Quantitative catchment descriptors as the slope-area relation, the curvature-area relation and the cumulative area distribution (CAD) were used to assess this relationship. This study was built on a previous research by Istanbulloglu et al. (2008) based on an aspect-controlled ecosystem in central New Mexico whose findings suggested that wetter north-facing slopes were steeper than dryer south-facing slopes. This was found to be attributable to the dense vegetation cover on north-facing slopes that restrain runoff erosion (Istanbulluoglu et al., 2008). To the purposes of these studies, vegetation was distinguished according to the mesic ecosystem typical of the wetter north-facing slopes, and the xeric ecosystem of dryer south-facing slopes (Gutiérrez-Jurado et al., 2007).

Landform analysis that involved surface properties were conducted on an elevation-controlled ecosystem which is the Upper Rio Salado basin, in central New Mexico. The authors provided an individual comparison of land surface properties that considers lithology, soil and vegetation cover respectively. Successively, they also presented an interactive comparisons of the same surface properties comparing the S-A plots of different types (e.g. forest, grass and shrub) of one of the surface properties (e.g. vegetation) within a domain where the other two types of land surface properties remain fixed (e.g., soil: loam; lithology: Crevasse Canyon Formation). They called this combination of land surface properties a "land surface group" (LSG).

Focalizing our attention on the analysis for types of vegetation, since it can be considered as a basis for comparison to this thesis work, it is necessary to report in *Figure 1.7* the abovementioned quantitative catchment descriptors analyzed by Yetemen et al. (2010). The figure (a) illustrates that the transitions between scaling regimes of the S-A relation (from I to II, and II to III), occur at the same drainage area values for each type of vegetation. It also appears that, for all the three ranges (I, II and III), from ridges to large valleys, forests show the steepest plot, followed by shrubs and grasses respectively. Observing the curvature-area diagram (b), forests show the highest ridge divergence and valley convergence, followed by shrubland; while grasslands have the least divergent ridges and least convergent valleys. This trend is consistent with the C-A trends of all the land surface properties, that found the higher degree of ridge divergence in region I and the higher degree of convergence in regions II and III to be observed for the properties of the selected land surface which plot steeper throughout all three regions of the S-A relation. This pattern for the vegetation cover is attributed by the authors to the variation in the steepness index, *k*. According to the authors, change in the steepness index, *k*, from grasslands to forests up to twofold in all regions, suggests that differences in the type of vegetation do not influence the nonlinear dependence of geomorphic processes to A and S within a given scaling region, but do influence the transport efficiency coefficient *K*. The steepness index, *k*, and also the concavity index (or degree of steepness), θ, are the parameters that relate the local slope of a given point on the landscape to its contributing area value, according to the power-law function in *Equation 1.16*.

$$S = kA^{\theta} \tag{1.16}$$

where are also true the following relations:

$$k = \left(\frac{D}{K}\right)^{\frac{1}{n}} \tag{1.17}$$

$$\theta = \frac{(1-m)}{n} \tag{1.18}$$

In *Equation 1.17* the parameter *D* is the long-term average denudation rate and *K* is the empirical transport efficiency coefficient. The parameters *m* and *n*, present in both *Equation 1.17* and *Equation 1.18*, are numerical parameters varying with different form of erosion (Kirkby, 1971; Montgomery, 2001 and Yetemen, 2010). To this regard, sediment transport in soil-mantled hillslopes where runoff is not erosive is characterized by a transport-limited

slope-dependent diffusive process with $m=0$. This suggests a convex hillslope morphology leading to a positive relation between S and A ($\theta > 0$). Conversely, fluvial sediment transport presents the parameters m and $n > 1$ ($\theta < 0$) leading to an inverse relationship for S with A and featuring a concave upward channel profile. It is also important to remember that change in the sign of θ from region I to II corresponds to the switch between convex diffusion-dominated ridges to concave valleys where episodic rill erosion takes place (Istanbulluoglu et al., 2008). Furthermore, Yetemen et al. (2010) found out that the cumulative area distribution (CAD) of a region with steeper slopes plots below the CAD of shallower slopes, meaning that the exceedance probability of a given area is higher for regions with lower slopes. This suggests that the land surface properties (also in the vegetation case) may influence the constant of the power-law distribution, while scaling exponent of the distribution remains close to 0.43.

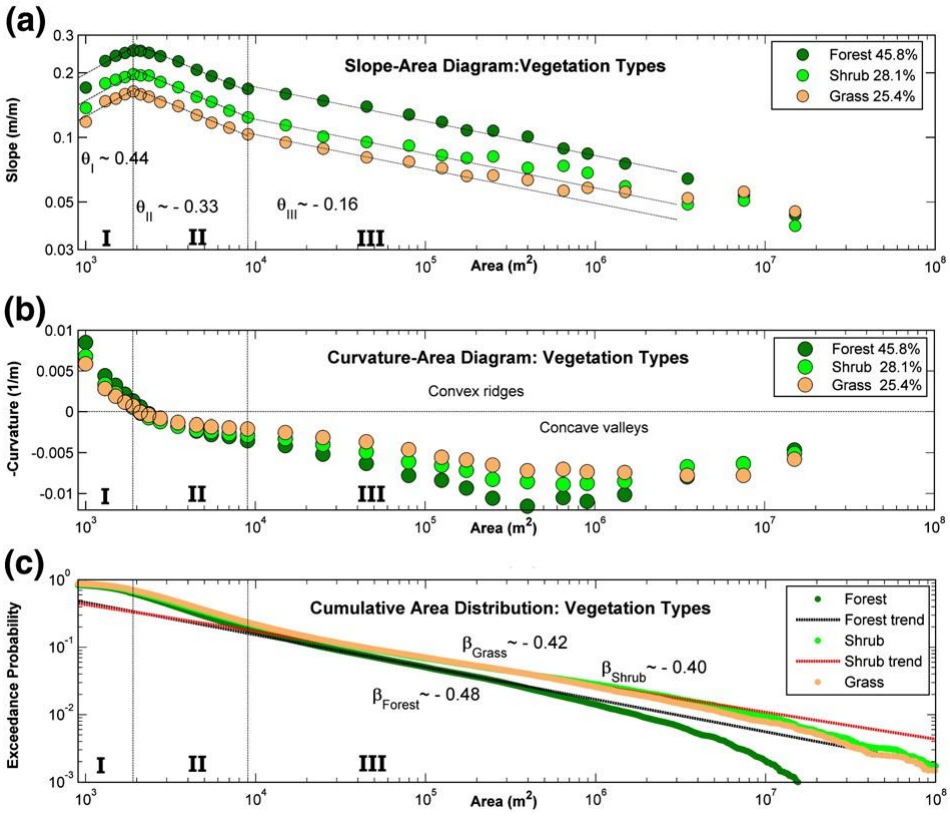

Figure 1.7 - a) slope-area (S-A) relation; b) curvature-area (C-A) relation; c) cumulative area distribuion (CAD) of the types of vegetation in the URS basin. Note: the trend line for grass is not given in (c) for clarity purpose. (Yetemen et al. 2010)

Results from Yetemen et al. (2010) exhibit a close association between catchment morphology and its underlying lithology, soil and vegetation cover. These land surface properties indeed, can influence slope steepness, the valley head position and the beginning of

perennial channels on the landscape. In addition, the mesic north-facing slopes were found to be typically steeper with planar morphology than the shallower and more dissected xeric south-facing slopes, thus implying a strong ecosystem control on landscape morphology. In particular, the authors found out that the south-facing slopes in the study sites, which were subject to more erosive runoff, could maintain long-term rates of erosion equal to base-level fall with shallower slopes, while more resistant north-facing slopes, with lower runoff potentials, require higher hillslope gradients to keep up with base-level fall, largely with soil creep transport (Istanbulluoglu et al., 2008; Yetemen et al., 2010). This view is consistent with the statement from Dietrich et al. (2003), who suppose the fluvial erodibility and hillslope diffusivity in soil-mantled landscapes to be determined by soil mechanical and hydrological properties as related to soil texture, functional type and dynamics of vegetation. Moreover, Gutierrez-Jurado et al. (2007) asserted that in arid and semi-arid regions, hydrology is strongly dictated by spatial patterns and connectivity of vegetation between the bare and vegetated patches of the landscape and also reported the differences in soil moisture between north- and south-facing slopes, illustrating the resource conserving and non-resource conserving roles, respectively.

Considering again the S-A relation in *Figure 1.7- 4a* , the steeper maximum slopes presented by the forests at the valley head position, followed by shrubs and grasslands can be explained by the more frequent soil slips occurrence under shallower hillslopes gradients on bare or sparsely vegetated surfaces with interconnected bare patches than forested areas. This is due to the forested hillslopes capability to bear greater critical hillslope gradients for threshold slopes than unvegetated slopes (Roering et al., 1999). Finally, results coming from the comparison among different land surface groups (LSGs) suggested that changes in soil texture (from loam to silt loam) and vegetation (from forest to grass) showed the greatest increase on slope steepness in the study area (Yetemen et al., 2010). Thus, evaluating the differences in the catchment geomorphic descriptors with respect to different land surface groups, revealed a significant dependency between LSGs and landscape morphology. A final consideration from the authors highlighted the responsibility of climatic fluctuations on replacing vegetation communities, leading to amplified hydrological and geomorphic responses.

1.2 Goals of the thesis

In accordance with such forward, this work of thesis is aimed to verify a possible correspondence existing between vegetation distribution patterns and the morphological characteristics of two different catchment areas, through the comparison of morphometric parameters such as aspect, local slope, mean landform curvature, upslope drainage area and the topographic wetness index. Particular attention has been addressed to the analysis of the vegetation classes' organization through subsequent scaling regimes of local slope versus drainage area. The analysis has been carried out over two distinct watersheds, the Miozza and Cetus basins. The former is an alpine catchment, located in the Carnia region of the North-Eastern Italian Alps, while the latter is a coastal basin on the Tyrrhenian sea, under the Salerno province. A preliminary research on the same topic was conducted by Tarolli et al. (2006) over two headwater catchments of the Miozza basin, which are the same study areas that have been examined in this work, besides the other study area of the Cetus basin.

The main purpose that supports this research is the understanding of the specific attitude showed by different vegetation types to occupy distinct hillslope morphologies, that is also the key concept investigated by Tarolli et al. (2006). Results from their study suggested that vegetation does play a fundamental role in slope stability, as it is directly related to erosion processes. This conclusion was supported by the evident dominance of different vegetation types over specific slope-area regimes. Diagrams of the relative frequency of vegetation classes and slope-area plots revealed an increasing shift toward woody vegetation with increasing slope steepness. Particularly, coniferous forest were found to be mainly located on drier and steeper hillslopes, consistently with their values of root cohesion; while shrub species, primarily represented by the Green Alder, specifically occupy landslides dominated areas, morphologically represented by high values of local slope and drainage area (Tarolli et al., 2006). The spatial distribution of Green Alder in relation to slope-area regimes is in accordance with the pioneering behavior of this species that typically invades open spaces, screes, abandoned pastures or debris flow paths. This characteristic was retained by the authors to be significant in recognizing dominant geomorphic processes in high altitude areas of Eastern Italian Alps (Tarolli et al., 2006; Tarolli, 2007).

The study areas of the Miozza and the Cetus basins are located in two distinct Italian regions with different geographic positions, lithologies, moisture regimes and climatic conditions.

They have been selected to better analyze vegetation dynamics with respect to contrasting situations: on the one hand there is the high elevation and humidity alpine environment of the two study areas within the Miozza catchment, characterized by glacial morphology and landslide signatures; while, on the other hand there is the low elevation, Mediterranean xeric environment of the coastal hillside, which defines the Cetus basin. Geomorphic and ecologic dissimilarities between the two basins are expected to highlight eventual correspondences linking vegetation patterns to the topographies of each basin. As it will be later discussed, vegetation species representative of each basin have been classified in various typologies that could be significantly related to the analyzed morphometric parameters. Those vegetation classes are the same for the two study areas of the Miozza basin, which are also equal to the classes defined by the researches cited above; whereas other types of vegetation cover, more specific to water stress tolerance, have been identified for the Mediterranean study area. Besides the differences between the two basins, the procedure that has been applied was almost the same. After having made comparable the initial surface representations of the two basins, so to have high resolution DTMs for each study areas, specific morphometric parameters have been calculated and successively related to each other through statistic computations. Remarkable attention has been paid to the slope-area and curvature-area relationships, since, as already explained, they could reveal significant evidences of linkages between geomorphic processes and vegetation dynamics.

In addition to the main goal of this thesis, the analyses have also been focused on the comparison among different DTMs resolutions. Moreover, the two basins had not the same surface representation, since digital elevation data relative to the Cetus basin were available as a TIN surface, whereas data available for the Miozza basin were already DTMs with different grid sizes. Therefore, two DTMs were created by the TIN surface at 5 m and 10 m resolutions for the Cetus basin and two DTMs at 1 m and 3 m resolution were selected for the Miozza basin.

The following chapters are structured to properly describe the morphometric parameters used in the data analysis process and the applied methodology (*Chapter 2*) and to furnish a specific description of the analyzed basin areas, both from a morphological point of view and from their vegetational composition (*Chapter 3*). Subsequently, results are reported and commented in detail (*Chapter 4*) to finally propose some remarks and considerations (*Chapter5*).

2 MATERIALS AND METHODS

2.1 LiDAR technology: overview and applications

In the last years a new technology has been developed to acquire high precision and georeferenced spatial information about the shape and the topography of a terrain. This is the LiDAR (Light Detection And Ranging) remote sensing system, which can be described as the implementation of a laser scanner on a platform, that can be ground-based stationary for small areas detection or deployed on an helicopter or aircraft for larger areas surveys. Airborne topographic LiDAR systems are the most common used for generating digital elevation models for large areas (Carter et al., 2012). The procedure for an Airborne LiDAR survey consists in flying along parallel paths over an area and operate pulsing laser scans from side to side while, performing as an optical remote sensing technology, the system measures properties of scattered light to find information about a distant target. Similar to radar (RAdio Detecting And Ranging) technology, which uses radio waves instead of light, the range to an object is determined by measuring the time delay between transmission of a pulse and detection of the reflected signal and multiplying it by the speed of light. The electric impulse, created by a generator, emits a beam of infrared light; the emitted signal is then backscattered and reflected by the objects, and the measurement mechanism is able to provide some of the properties (e.g. traveling time, signal intensity) of the reflected pulse (Wehr and Lohr, 1999). If the traveling time (Δt), spent by the laser pulse to reach the target and come back to the sensor, which is computed through a quartz clock, is divided by two and multiplied by the speed of light, the result corresponds to the distance (D) from the aircraft to the target, giving its elevation value:

$$D = \frac{\Delta t * c}{2} \qquad 2.1$$

where c ($3 \cdot 10^8$ m/s) is the speed of light (Watkins, 2005; Weitkamp, 2005). Moreover, the laser angle is recorded as well in such a way that from this information the location, in three dimensions, of the reflecting object can also be computed (Carter et al., 2012). The telemeter measures the travelling time in a discrete way, and this implies that also the distance is obtained as the sum of infinitesimal distances (Casella, 2003). The resolution in time δt, thus

the shortest measurable lapse time, is in inverse proportion to the frequency of the generator (*f*):

$$\delta t = \frac{1}{f} \qquad 2.2$$

while the resolution in distance δD is obtained by substituting the term δt in *Equation 2.1*.

The results consist in the restitution of three dimensional coordinates representing latitude, longitude and elevation of each measurement to the target object. However, in the actual data computation this process has also to take in account the exact position of the plane beside flight disturbances, while keeping track of hundreds of laser pulses per second. To accomplish this goal, a Global Positioning System (GPS) receiver and an Inertial Measurement Unit (IMU) are both installed on the LiDAR system (Habib et al., 2005; Reutebuch et al., 2005; Webster and Dias, 2006; Pfeifer and Briese, 2007). The GPS receiver is used to record the aircraft trajectory and position in absolute coordinates, while the IMU unit measures the altitude of the aircraft (roll, pitch and yaw or heading) (Webster and Dias, 2006). Therefore, by synchronizing the information derived by the scanner, the IMU and the GPS, it is possible to determine the target location with high accuracy in three dimensional spaces (Liu, X. et al., 2007), as showed *Figure 2.1*.

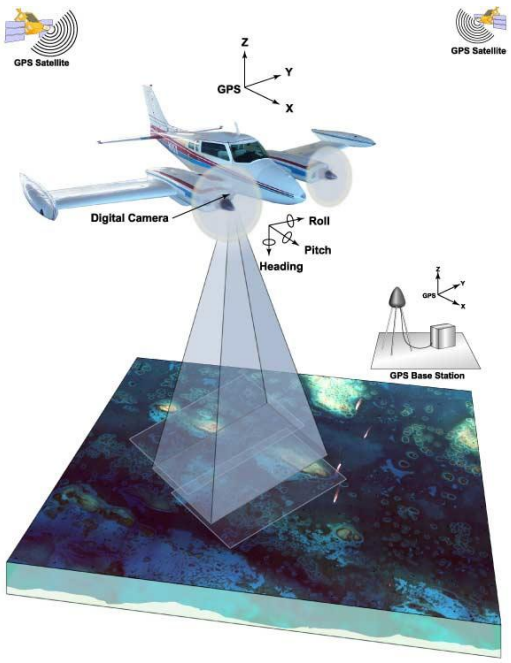

Figure 2.1- Basic airborne LiDAR data collection schematic explanation (Klipp and Nayegandhi, 2007).

The laser scanner unit consists of a pulse generator of laser with a wavelength in the range of 0.8 μm to 1.6 μm and a receiver to get the signal of scattered and reflected pulses from targets (Wehr and Lohr, 1999; Mukai et al., 2006; Pfeifer and Briese, 2007). Many LiDAR systems operate in the near-infrared region of the electromagnetic spectrum, although some sensors also operate in the green band to penetrate water and detect bottom features. These bathymetric LiDAR systems can be used in areas with relatively clear water to measure seafloor elevations (Carter et al., 2012). Airborne topographic mapping LiDARs generally work at 1064 nm frequency, while bathymetric systems generally use 532 nm frequency, because 532 nm penetrates water with much less attenuation than 1064 nm does (Cracknell A. P. and Ladson Hayes, 1991). One of the most concerning issues about airborne LiDAR technology is the laser footprint dimension. It has a variability range of about 10 cm to 2 m and it is directly related to the flight altitude and the opening angle of the scanner. It can be settled according to the needed point coverage density and it supports the "multiple returns system", which consists in a multiple record of the backscattered signal over subsequent times. In a multiple return system, where a single pulse meets an object (e.g. a tree crown), part of the signal is scattered, while the remaining part continues until it reaches the ground. The number of returns can be helpful to determine the shape of the hit surface. Multiple return systems, which are common, can capture up to five returns per pulse (*Figure 2.2*). This can increase the amount of data by 30% or more (100,000 pulses/second ≈ 130,000 returns/second) and increases the ability to look at the three-dimensional structure of the features above the ground surface, such as the forest canopy and understory (Carter et al., 2012).

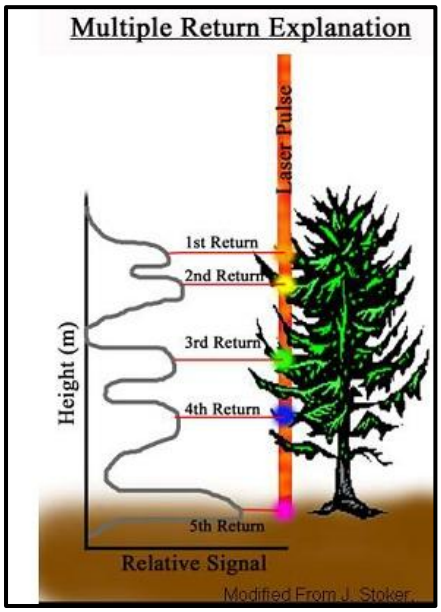

Figure 2.2 - Multiple returns from single pulse (Carter et al., 2012)

Recording multiple returns is quite useful for the topographic mapping in forested areas or for the description of forest stand and structure (Sheng et al., 2003), and it is of great advantage in mountainous environments.

LiDAR data derived from a scan are presented as *point clouds* that are a set of measured positions in three-dimensional space of point locations on a scanned surface (e.g., bare ground, trees, roads, buildings, etc.), which are typically attributed with return intensity, time and return number, in the case of multiple returns for a single shot. Point clouds must be properly processed through filtering techniques in order to create Digital Elevation Models (DEMs) as surface representation methods for scientific purposes. In addition, they can be classified as ground surface, artificial structures, or multi-storey vegetation canopies during post-processing. DEMs are created from the points classification and can represent bare ground or other surfaces such as the first surface or the last-return surface (Carter et al., 2012). In *Figure 2.3* is provided a simple example of point cloud filtering.

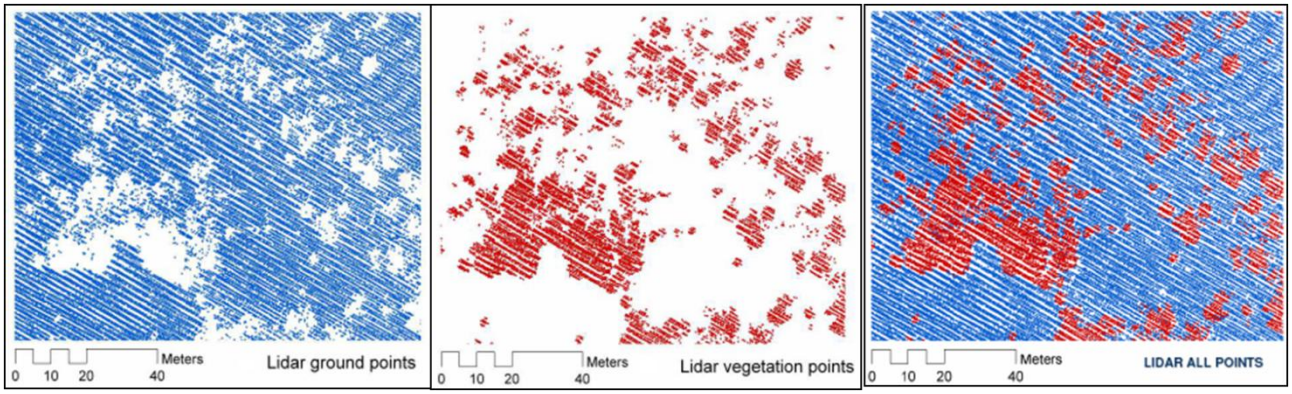

Figure 2.3 - LiDAR data points classification: blue-colored ground points at the left side, red-colored vegetation points at the center, all points representation at the right side. (Tarolli and Tarboton, 2006).

Since high resolution DEMs are generated from LiDAR data by gridding and interpolating the measured point cloud, DEMs quality comes from the highly sensitive analysis. Thus, in addition to the uncertainties in LiDAR point locations, that will be later described, an additional level of uncertainty is considered because points in the DEM do not necessarily lie on the true surface. Conversion of the point cloud to digital elevation model is a destructive step, in that the original cloud cannot be regenerated from the derived DEM (Arrowsmith et al., 2008). However, the most common point classification of elevation data is the one that distinguishes ground elevation points from points representing all the other features (e.g. vegetation and buildings). The representation model related to the former case is called a Digital Terrain Model (DTM), while the one associated to the latter case is known as Digital Surface Model (DSM) (*Figure 2.4*).

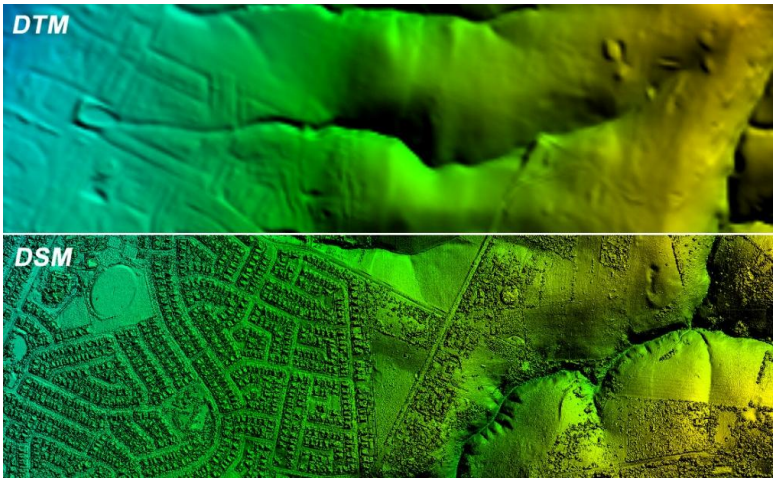

Figure 2.4 - Digital Terrain Model (DTM) and Digital Surface Model (DSM) representation (AEROmetrex digital mapping 2013).

It is also important to highlight that point cloud data are scattered, so that both point spacing and point density (number of points per m^2) vary within the scan. As a consequence, the high measuring rate of laser scanning is of particular importance. Present pulse rates lie between 2 kHz and 25 kHz. Accordingly, from 1000 m flying height, the sampling densities on the ground range from about 1 point per m^2 up to 20 points to m^2 (Ackermann, 1999).

Bearing in mind that accuracy is one of the primary reasons for the use of LiDAR data, since this technology represents a precise, cost-effective method for collecting topographic elevation data for large areas, it becomes particularly important to document the achieved level of data accuracy for the sake of usability. Typically, a data set is collected with a target accuracy value (Carter et al., 2012). Once data have been collected and processed, they must be tested to make sure that the collection and subsequent operations were successful in meeting the desired specifications; this is developed by measuring ground control points and comparing them with those generated from the LiDAR detection. It is also important to document data accuracy in order to ensure a proper use of the collected data and to maximize their utility. For this reason, information about accuracy is commonly provided in the metadata. The overall vertical system accuracy is usually in the dm order and is related to the accuracy of GPS and IMU. Airborne GPS is able to yield results in 5 cm horizontally and 10 cm vertically, while IMU can generate attitude with accuracy within a couple of centimeters (Liu, 2008).

The main sources of uncertainty in the point locations include accuracy of the laser scanner, Inertial Measurement Unit (IMU, in the airborne case) and GPS system, registration of individual scans, and georeferencing of the resulting point cloud (Arrowsmith et al., 2008). Concerning uncertainties, one of the most influencing feature of the LiDAR system is the laser ranging accuracy, which indeed deserves ground tests and calibrations to verify its sensitivity. In addition, there may be error in the laser range measured due to time measurement error, wrong atmospheric correction and ambiguities in target surface which results in range walk. Additional errors could be introduced in LiDAR data due to complexity in the object space, such as surface roughness, sharp steepening and also terrain covers. Error could range from a few cm in open canopies up to several meters in closed canopies and sloping terrains. Erroneous outlier points might also include reflections from objects such as birds, atmospheric effects (dust, moisture), multiple reflections and very bright points. Moreover, a further significant source of uncertainties comes from the points cloud filtering

and the coordinate conversion processes. Since the x, y, z coordinate values of the points are given by the GPS system, it is important to note that their positioning in space is referred to the WGS-84 datum. If on one hand the horizontal transition from the WGS-84 to the Rome 40 datum, which is the one of Italian cartography, is fairly standardized, on the other one the conversion from ellipsoidal to orthometric heights is subject to a substantial error (Cavalli et al., 2008).

However, in the last few years, LiDAR-DTMs have been used for detailed planning and environmental managing applications. In mountainous environments, they have been proved to be feasible in characterizing shallow landslides as a basis for numerical modeling, in recognizing alluvial fans deposition for the study of the longitudinal profile of rivers and,, in analyzing the characteristics and distribution of vegetation cover (Cavalli et al., 2008). Moreover, watershed delineation from surface morphology and the integration of hydrological models can be used to understand the hydraulic behavior of analyzed catchment in order to develop a powerful tool for extreme events prevention. The use of high resolution DTMs is also very common in the identification of fluvial and coastal erosion and, more in general, of all the areas in a landscape exposed to hazard conditions that could be potentially damaging for human activities.

The highly detailed topography description that can be reached through the use of this recently developed technique is not only applied to the Earth surface but also to examine its atmosphere chemical composition and climate changing (i.e. NASA's Langley Research Center - LiDAR Applications Group). Besides, LiDAR technology is getting involved in space observations as in the case of the NASA Phoenix Mars Mission aimed to study the polar atmosphere of the red planet.

Furthermore, among other fields, urban planning, forest managing and also archaeological surveys can benefit of LiDAR technology every time it is used to generate Digital Surface Models.

2.2 Surface representation

The final surface representation, which is the core object of topographic surveys, comes from the interpretation of elevation data. In the past, and still in some cases, these data were obtained in much economic but less accurate ways such as ground level surveys or even

before, digitalization of topographic maps. Nowadays, the increasing need for reliable data which may need to be collected with a high density of points, even over wide areas and in the shortest time possible, has been fulfilled with the development of remote sensing techniques. Among others, the LiDAR technology has been commonly preferred in mountainous environments for its feasibility.

Surface from LiDAR cloud points data can be represented as a) DEM raster grid, b) TIN surface or c) contour-based network as shown in *Figure 2.5*.

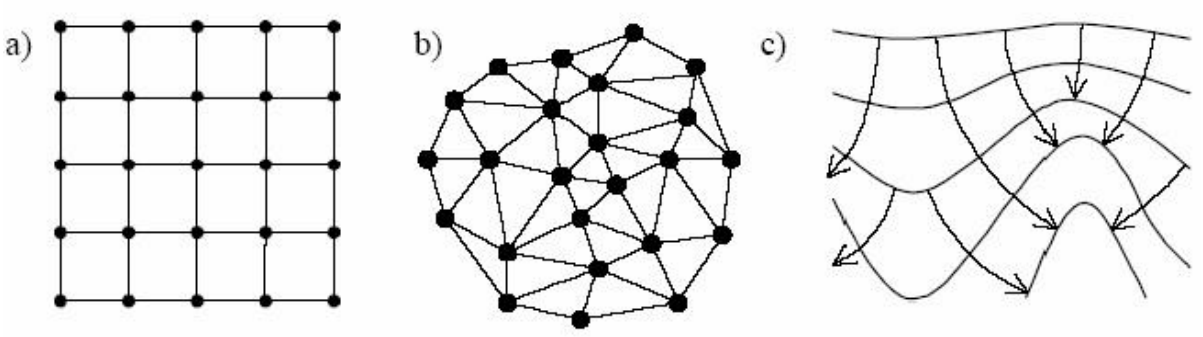

Figure 2.5 - Methods of structuring an elevation data network: a. DEM grid network; b. TIN (triangulated irregular network); c. contour-based network. (Moore et al. 1991).

While contour-based methods have computational advantages in hydrologic modeling, because the structure of their elemental areas is based on the way in which water flows on the land surface, topographic attributes can be more easily computed starting from a TIN surface or, even better, from a raster grid surface, that actually presents less irregularities.

Within this classification of surface representations, Moore et al. (1991) described the contour-based methods as a set of contour lines that are stored as Digital Line Graphs (DLGs) in the form of x, y coordinate pairs along each contour line of specified elevation. These can be used to subdivide an area into irregular polygons bounded by adjacent contour lines and adjacent streamlines.

Conversely, TIN surface representation can be described as a form of vector-based digital geographic data, which is constructed by triangulating a set of vertices (points of the collected point cloud). The vertices (nodes) are connected with a series of edges (breaklines) to form a network of triangles (facets). Each of these triangular facets describes the shape and position of a portion of the TIN surface, deriving this information from its vertices, stored as a set of x, y, z coordinates.

There are different methods of interpolation to form these triangles, such as Delaunay triangulation or distance ordering. The resulting triangulation that satisfies the Delaunay

triangle criterion ensures that no vertex lies within the interior of any of the circumcircles of the triangles in the network. If the Delaunay criterion is satisfied everywhere on the TIN, the minimum interior angle of all triangles is maximized. The result is that long, thin triangles are avoided as much as possible.

The edges of TINs form contiguous, non overlapping triangular facets and can be used to capture the position of linear features that play an important role in a surface, such as ridgelines or stream courses. Moreover, since nodes can be placed irregularly over a surface, TINs can have a higher resolution in areas where a surface is highly variable or where more detail is desired and a lower resolution in areas that are less variable. The input features used to create a TIN remain in the same position as the nodes or edges in the TIN. This allows a TIN to preserve all the precision of the input data while simultaneously modeling the values between known points.

However, TIN models are less widely available than raster surface models and tend to be more expensive to build and process. The cost of obtaining good source data can be high, and processing TINs tends to be less efficient than processing raster data because of the complex data structure. For this reason, TINs are typically used for high-precision modeling of smaller areas, such as in engineering applications, where they are useful because they allow calculations of planimetric area, surface area and volume. The maximum allowable size of a TIN varies relative to free, contiguous memory resources. Ten to 15 million nodes represent the largest size achievable under normal operating conditions with Win32. Regardless, it is strongly recommended to cap the size at a few million for the sake of usability and performance.

On the other hand, raster grid DTMs faced a widespread use for morphological quantification, mainly due to the fact that the matrix form is the simplest and the most efficient approach in terms of storage and manipulation (El-Sheimy et al., 2005; Ramirez, 2006; Ziadat, 2007). In its simplest form, the raster format consists of a geo-referenced matrix of cells (or pixels), which is organized into rows and columns where each cell contains a constant elevation value. The main advantages of storing data as a raster are the following:

- a simple data structure, which allows the use of simpler algorithms for data processing;
- a powerful format for advanced spatial and statistical analysis;
- the ability to represent continuous surfaces and perform surface analysis;
- the ability to perform fast overlays with complex datasets.

Nevertheless, the computations used to create DEMs range from simple to complex gridding techniques and can create slightly different surface types. These techniques are attributable to the interpolation process, which is made of a set of spatial analyst functions that predict values for a surface from a limited number of sample points, creating a continuous raster The appropriate interpolation method depends on the data and the desired use of the DEM (Carter et al., 2012). Concerning this, interpolation methods try to make the DTM accuracy as high as possible in relation also to the kind of surface in consideration, but this surely depends also on the quality of the source data. Thus, the features which have an impact on DTMs accuracy are the point density and terrain slope (Karel and Kraus, 2006), the ratio of point resolution to grid resolution and the distance between each point and its nearest neighbor (Briese, 2010).

To give an idea on how interpolation works, here are reported some of the more used interpolation methods which also are shown in *Figure 2.6* and *Figure 2.7*.

- **Natural neighbor interpolation** (Sibson, 1981), is an appropriate weighted-average interpolation method for calculating a grid of values from data which can be both regular, clustered or random combinations of distributions of points. The first step is a triangulation of the data by Delauney's method, in which the apices of the triangles are the sample points in adjacent Thiessen polygons. The triangulation is unique except where the data are on a regular rectangular grid. To estimate the value of a point, it is inserted into the tessellation and then, its value is determined by sample points within its bounding polygons. For each neighbor, the area of the portion of its original polygon that became incorporated in the tile of new point, is calculated. These areas are scaled to sum to 1 and are used as weights for the corresponding samples (Webster and Oliver, 2001). This technique is designed to favor local minimum and maximum values in the point file and can be set to limit overshoots of local high values and undershoots of local low values;

- **Inverse Distance Weighting (IDW)** (Shepard, 1968), like the previous one, is a weighted-average interpolation method that estimates the values of an attribute at unsampled points using a linear combination of values at sampled points, weighted by an inverse function of the distance from the point of interest to the sampled points. The assumption is that sampled points closer to the unsampled point, are more similar to it than those further away in their values (Li J. and Heap D.A., 2008). Weights diminish as the distance increases, so nearby samples have a heavier weight and have more influence on the estimation (Isaaks and Srivastava, 1989). The Inverse Distance Weighting interpolator indeed assumes that each input point has a local influence that

diminishes with distance. Therefore, it is not desirable to favor local high or low values but rather to look at a moving average of nearby data points and estimate the local trends;

- **Spline** (Ahlberg et al., 1967), is an interpolation technique that estimates values using a mathematical function that minimizes overall surface curvature, resulting in a smooth surface that passes exactly through the input points. It consist of polynomials that describe pieces of a line or surface and are fitted together so that they join smoothly (Burrough and McDonnell, 1998; Webster and Oliver, 2001). This method is best for gently varying surfaces, such as elevation, water table heights, or pollution concentrations;

- **Kriging** (Matheron, 1960), is a method of interpolation which predicts unkown values from data observed at known locations. It uses variograms to express the spatial variation and minimizes the error of predicted values which are estimated by spatial distribution of the predicted values. Kriging is an advanced geostatistical procedure that generates an estimated surface from a scattered set of points with z-values. Kriging is a weighted moving average technique, similar in some ways to Inverse Distance Weighting interpolation, even though, unlike IDW, Kriging can use different weighting functions depending on the distance and orientation of sample points with respect to the node, and the manner in which sample points are clustered.

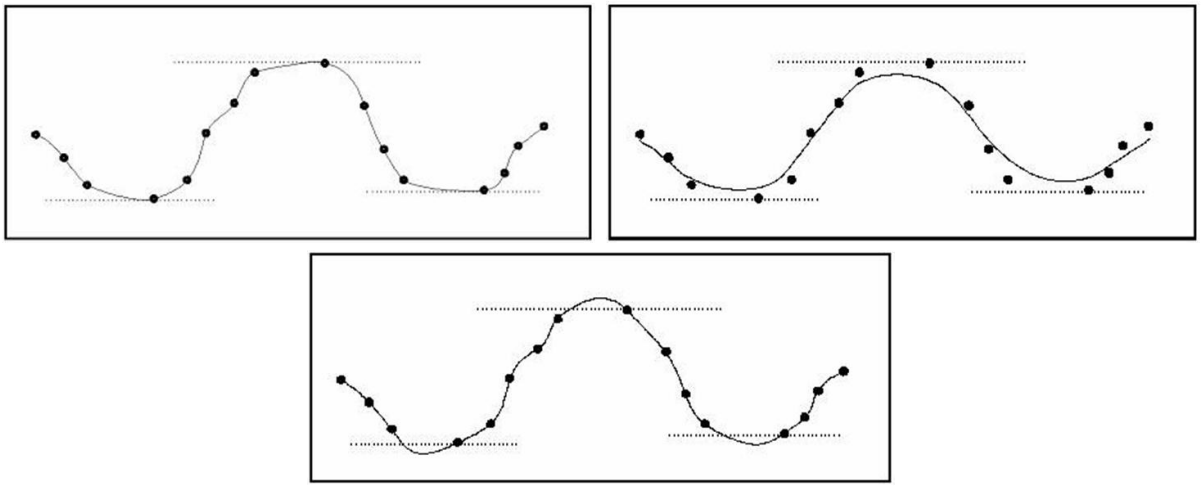

Figure 2.6 - Schematic representation of interpolation methods: Natural Neighbor at the top-left position, Inverse Distance Weighting (IDW) at the top-right and Spline interpolation at the bottom (Introduction to spatial analysis-planet.botany.uwc.ac.za - /nisl).

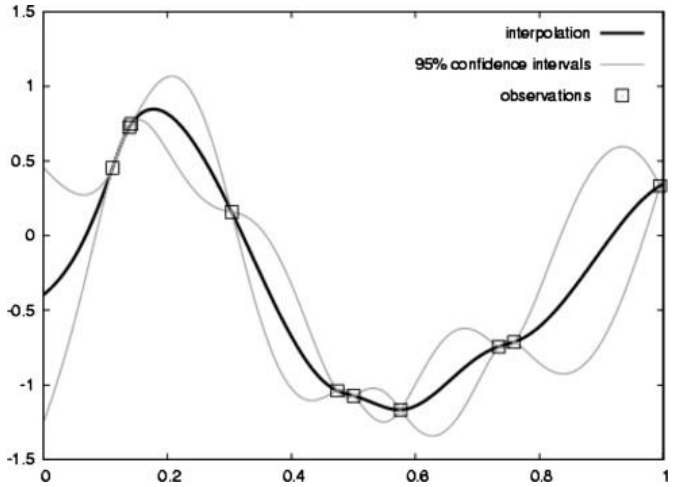

Figure 2.7 - Example of one-dimensional data interpolation by Kriging, with confidence intervals. Squares indicate the location of the data, the dark line is the Kriging interpolation and the confidence intervals are in light gray (Hu et al., 2008).

However, despite of the interpolation method used, the DTM raster grid surface representation always has a spatial uniform structure totally controlled by a single feature that is the cell size. The bigger is the cell size, the more general is the approximation of the terrain surface representation, and consequently, the lower is the resolution (Ramirez, 2006). The general idea is to select a resolution that produces best predictive properties without giving computational constraints. In general a grid DTM is commonly over-sampled in low relief areas and under-sampled in high relief areas (Hengl et al., 2003). In order to increase the details of the terrain representation, the sample point density must be raised while the cell size reduced.

Within the contest of this work, available topographic data presented the raster grid format for the Miozza basin and the TIN format in the case of the Cetus basin. However, for the sake of comparability, it was chosen to convert the TIN surface representation in a raster grid one. This because, even though triangulated irregular networks are more efficient and flexible in representing abrupt changes in elevation, specific catchment area and upslope flow paths calculation, the irregularity of the TIN surface makes the computation of attributes more difficult than for the grid-based methods (Moore et al., 1991).

2.3 Morphometric parameters

Morphometric parameters of a drainage basin are quantitative attributes derived from the terrain or elevation surface within a drainage basin, useful to characterize topographic features. To better describe them, Moore et al. (1991, 1993) divided terrain attributes in two categories: primary and secondary (or compound) attributes. The formers are computed directly

from the DTM through the use of a GIS software elaborating the specific elevation data associated to each cell of the raster grid; whereas the secondary attributes come from a further computation based on the primary attributes values Primary topographic attributes that have been directly calculated from DTMs in the contest of this work area: *Aspect, Slope, Flow Directions, Upslope drainage area*, *Specific Catchment Area* and *Landform curvature*; while as a secondary attribute the *Wetness Index* has been computed. Topographic indices can be embedded within the data analyzing system of a GIS, therefore, according to the aim of this paper, they have been calculated by using Spatial Analyst Tool of the ArcGIS software (version 10.1), TauDEM toolset (version 5.0, David G. Tarboton, 2005) and the LandSerf freely available software (version 2.3, Jo Wood, 2009).

2.3.1 Aspect

Hillslope aspect has important effects on both biotic and abiotic processes as it is directly involved in shadowing effects on the landscape and amount and timing of solar radiation. This may influence site-specific microclimatic conditions, such as temperature regimes, air humidity and evapotranspiration, besides impact soil properties, like moisture content and erosion; also affecting, in turns, vegetation species distribution and biodiversity (Vico and Porporato, 2009). Aspect defines the orientation of the analyzed surface. It identifies the downslope direction of the maximum rate of change in elevation from each cell to its neighbors, in fact the aspect for the processed cell is the direction of the plane fit by the slope function to the Z-values of a 3x3 cells neighborhood (see *Figure 2.8*). The value of each cell in an aspect dataset indicates the direction the cell's slope faces and the value of the output raster will be the compass direction of the aspect (N-S-E-W and their intermediate directions - *Figure 2.9*).

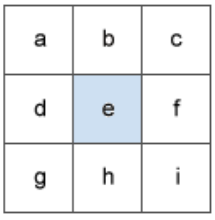

Figure 2.8 - Surface scanning window. The neighbors are identified as letters from a to i, with e representing the center cell (ArcGIS Help 10.1 - ESRI 2012).

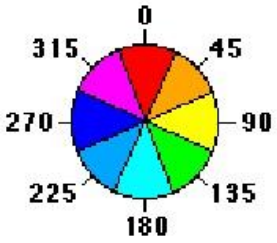

Figure 2.9 - Aspect is measured clockwise in degrees from 0 (due north) to 360 (again due north), coming full circle. Flat areas having no downslope direction are given a value of -1.((ArcGIS Help 10.1 - ESRI 2012)

To compute Aspect, the ArcGIS Spatial Analyst Tool uses, also in this case, the already shown 3x3 moving window (*Figure 2.8*) and for each cell in the center of the window, an aspect value is calculated using an algorithm that incorporates the values of the cell's eight neighbors, according to *Equation 2.3*. In such way, the value of the center cell *e*, related to the values of the neighbor cells, determines the changes in direction both on the x and y axes. From an analytical point of view, the rates of change in the x and y directions for the center cell are calculated with the following algorithms:

$$[dz/dx] = \big((c + 2f + i) - (a + 2d + g)/8\big) \qquad 2.3$$

$$[dz/dy] = \big((g + 2h + i) - (a + 2b + c)/8\big) \qquad 2.4$$

Given the rate of change in both the x and y direction for cell *e* (*Figure 2.8*), aspect is calculated using:

$$aspect = 57.29578 * atan2\,[(dz/dy), -(dz/dx)] \qquad 2.5$$

The aspect value is then converted to compass direction values (0-360 degrees), according to the following rule:

```
if aspect < 0
cell = 90.0 - aspect
       else
if aspect > 90.0
cell = 360.0 - aspect + 90.0
       else
cell = 90.0 - aspect
```

Like the Slope tool, also the Aspect one is mainly run on an elevation dataset, as shown in *Figure 2.10* .

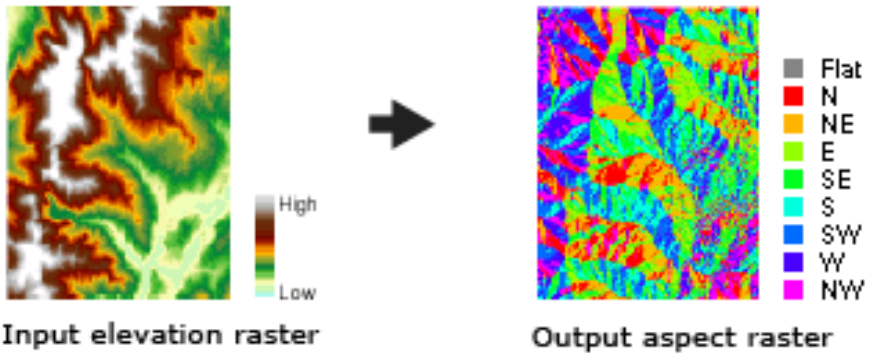

Figure 2.10 - Output aspect raster from an input DTM (ArcGIS Help 10.1 - ESRI 2012).

2.3.2 Slope

2.3.2.1 Topographic slope

Topographic slope identifies the first surface derivative of terrain elevation and can be described as the maximum change in elevation value from each cell of a raster grid. Topographic slope coincides with the Standard Slope Function which is also known as the "*Horn method*", due to the researcher's name who developed it (Horn, 1981). The function calculates, for each cell, the maximum rate of change in value from that cell to its neighbors. Basically, the maximum change in elevation over the distance between the cell and its eight neighbors, identifies the steepest downhill descent from the cell. Conceptually, the slope function fits a plane to the z-values of a 3 x 3 cell neighborhood around the processing or center cell. The direction the plane faces is the aspect for the processing cell. The lower is the slope value, the flatter is the terrain; the higher is the slope value, the steeper is the terrain. If there is a cell located in the neighborhood with a "no data" z-value, the z-value of the center cell will be assigned to the location. At the edge of the raster, at least three cells (outside the raster's extent) will contain "no data" as their z-values; to these cells will be assigned the center cell's z-value. The result is a flattening of the 3 x 3 plane fitted to these edge cells, which usually leads to a reduction in slope. The output slope raster can be calculated in two types of units, degrees or percent rise.

The topographic slope can be identified by *Equation 2.6*, which is commonly represented in units of degrees using the algorithm presented in *Equation 2.7* where the value *57.29578* is a truncated version of the result from 180/π.

$$slope = \sqrt{\left(\frac{\delta z}{\delta x}\right)^2 + \left(\frac{\delta z}{\delta y}\right)^2} \quad 2.6$$

$$slope\ (°) = \tan^{-1}\sqrt{\left(\frac{\delta z}{\delta x}\right)^2 + \left(\frac{\delta z}{\delta y}\right)^2} * 57.29578 \quad 2.7$$

These formulas assume that a plane surface can be placed at any point on the surface z (x,y) in such a way that it only just touches the surface: it is a tangential plane and relies on the notion of infinitesimally small distances. However, surfaces within GIS are typically modeled as grids, with a finite resolution. The values of the center cell *e* and its eight neighbors (identified as letters from *a* to *i*) determine the horizontal $\left(\frac{\delta z}{\delta x}\right)$ and vertical $\left(\frac{\delta z}{\delta y}\right)$ deltas as reported in *Equation 2.8* and *Equation 2.9* (*Figure 2.8*).

$$[dz/dx] = \big((c + 2f + i) - (a + 2d + g)/(8 * x\_cellsize)\big) \quad 2.8$$

$$[dz/dy] = \big((g + 2h + i) - (a + 2b + c)/(8 * y\_cellsize)\big) \quad 2.9$$

The Slope tool is most frequently run on an elevation dataset, as the following diagrams show. Steeper slopes are shaded red on the output slope raster (*Figure 2.11*).

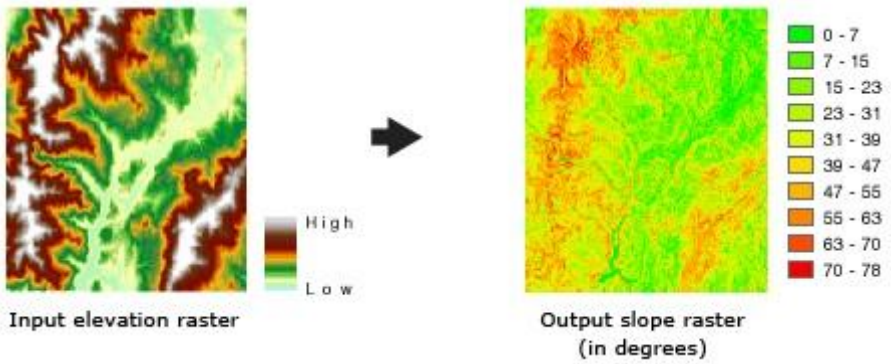

Figure 2.11 - Output slope raster from an input DTM (ArcGIS Help 10.1 - ESRI 2012).

2.3.2.2 Local slope

The *local* or *hydrologic* slope is a more hydrologically correct method to elaborate the slope parameter, based on the computation of the steepest outwards slope looking at one of the eight directions at which the neibouring grid cells are located, measured as drop/distance to the center cell of a three per three moving window (Eight Direction Pour Point Model - D8). *Figure 2.12* shows how the slope computation according to this method works. It is worth remembering that the derived local slope value is a dimensionless parameter.

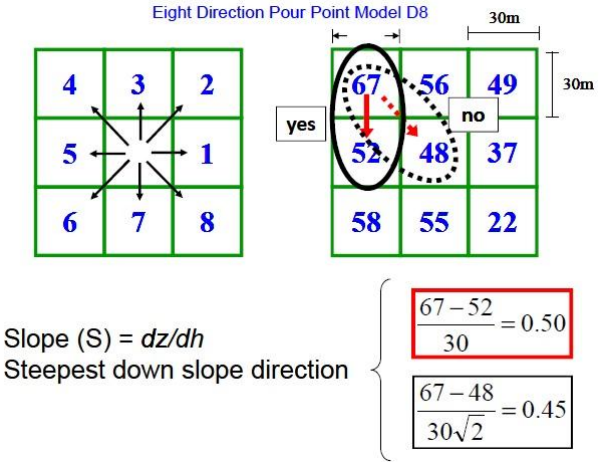

Figure 2.12 - Local slope computation according to the Eight Direction Pour Point Model (Fattorelli, Tarolli, Sofia, 2010).

2.3.3 Upslope drainage area

Another significant parameter to hydrologically characterize the analyzed surface is the upslope drainage area which is defined as a planimetric portion of area enclosed within a topographic divide, contributing to the runoff formation into the considered element. In the contest of raster grid files, the upslope area can be defined as the flow accumulation of each cell of the basin, estimated as the product of the number of pixels draining through each pixel and pixel area (Tarboton, 1997). The upslope area is strictly related to the flow direction algorithm (whose choice will be later dealt with), as the contributing area of each grid cell is taken as its own contribution plus the contribution from upslope neighbors that have some fraction draining to it, according to the chosen method to compute flow direction. The *D-Infinity* model from Tarboton (1997), adopted by the TauDEM Toolbox (version 5.0), was used to the purposes of this work. According to this algorithm, the flow from each cell either all drains to one neighbor (if the angle falls along a cardinal or diagonal direction) or is on an

angle falling between the direct angle to two adjacent neighbors. In the latter case the flow is proportioned between these two neighbor pixels according to how close the flow direction angle is to the direct angle to those pixels. The calculation is initiated by calling this function for the outlet pixel, then it recursively calls itself for all pixels that contribute to the upslope area at the outlet. The recursion stops when it reaches a pixel that has no pixels upslope (Tarboton, 1997). For this reason, cells on the ridge of the basin will have an upslope value equal to one, whereas the cell at the outlet of the basin will have the maximum upslope value because it comprehends all the drainage contributing cells, included itself.

2.3.3.1 DEM depitting

Dealing with morphological analysis, it is of maximal relevance to work with "hydrologically correct" DTMs, that means that they should not be affected by artifacts of the processing algorithms. During the DTM creation process indeed, some local punctual errors could be committed and due to this, some pits are produced. In digital terrain representations, pits comprised of grid cells surrounded by grid cells of higher elevation occur more commonly due to deficiencies in the digital elevation model production processes and generalization in the representation of terrain (Jenson and Domingue, 1988; Jenson, 1991). Raster grid DTMs presenting some pits in their structure must be corrected prior to come along the computation of morphometric parameters, in order to preserve them from inaccuracy. To more precisely describe them, pits are low elevation areas in digital elevation models that are completely surrounded by cells presenting higher elevation values, therefore it has no downstream cell to flow into, as a sink. Pits are generally removed by raising their elevation to the point where they drain off the edge of the domain. Pit filling was first implemented using methods that identify the region draining to each pit and the lowest point on the boundary, the so called pour point, then raising the elevation of all points within the region to at least the pour point elevation (Jenson and Domingue, 1988). TauDEM presently uses an implementation of this approach that first identifies pits then recursively scans upslope to find the pour point so as to be able to raise the elevation within the pit to that level (Wallis et al., 2009).

However, it is possible that few pits actually exist on the terrain surface, while others are artifacts that need to be removed. For this reason, care needs to be exercised not to correct existing terrain pits. To do so, the actual pits should have "no data" elevation values inserted at their lowest point. "No data" values serve to define edges in the domain, and elevations are

only raised to where flow is off an edge, so an internal "no data" value will stop a pit from being removed, if necessary.

2.3.3.2 Flow directions calculation algorithms

For the sake of comprehension regarding the computation of the flow direction in a DTM analysis, it is needed to specify why the *D-Infinity* algorithm (Tarboton, 1997) was preferred and which the main differences are with some other similar algorithms. At this regard, here is reported a brief recap of the comparison made by Tarboton (1997) among its method and four others, which are:

1. the *D8* algorithm by O'Callaghan and Mark (1984)
2. the *Multiple flow* direction method MS (Multiple directions based on Slope) by Quinn et al.(1991) and Freeman (1991)
3. the *Lea's* algorithm (Lea, 1992)
4. the *DEMON* method by Costa-Cabral Burges (1994) based on the Lea's algorithm.

The Tarboton's algorithm is named as *D-Infinity* because it admits an infinite number of possible single directions and this is also the reason why it does not introduce grid bias or substantial dispersion. The former of these issues indeed, is typically derived by the D8 method, which is so called because it computes only eight possible flow directions, assigning flow from each pixel to one of its eight neighbors, either adjacent or diagonal, in the direction with steepest downward slope. In the case of the D8 algorithm, the direction of flow is determined by the direction of steepest descent, or maximum drop, from each cell. When a direction of steepest descent is found, the output cell is coded with the value representing that direction. Although this simple method avoids dispersion and represents a simple and efficient grid based matrix storage structure, it resolves flow direction too coarsely, resulting in streaks aligned with the grid due to the forcing of the flow biased by the grid alignment (Tarboton, 1997).

On the other hand, the substantial dispersion issue is typical of the *MultiFlow* (Multiple direction) methods. They generally introduce a substantial dispersion, as flow from a pixel is dispersed to all neighboring pixels with lower elevation, in proportion to their slope value, resulting in flow to be split in up to eight possible directions for each cell. Moreover, this also represents a complication in data storage. Dispersion, however, is presented by any method

that assigns flow from one pixel to more than one downslope neighbor and is evident in the terms of spreading flow from a single pixel (Tarboton, 1997).

Moreover, the plane flow methods (Lea, 1992; Costa-Cabral and Burges, 1994) are both involved in the approximation arising in fitting a plain through the elevation of the four pixel corners, these corner elevations being estimated by averaging the elevations of adjoining pixel center elevations (according to Lea's algorithm), or using grid elevation values as pixel corners fitting a plane surface for each pixel (according to the DEMON method). In these cases flow direction is continuously specified, minimizing dispersion, as an angle between 0 and 2π, but the threat of inconsistent or counter intuitive flow direction computation is led by a discontinuous representation of the surface at pixel edges (Tarboton, 1997).

The $D\infty$ algorithm determines a single flow direction (represented also in this case as a continuous quantity between 0 and 2π) in the direction of the steepest downward slope on the eight triangularfacets formed in a 3x3 window centered on the pixel of interest (*Figure 2.13*). The use of triangular facets avoids the approximation involved in fitting a plane and the influence of higher neighbors on downslope flow. Where the direction does not follow one of the cardinal (0, $\pi/2$, π, $3\pi/2$) or diagonal ($\pi/4$, $3\pi/4$, $5\pi/4$, $7\pi/4$) directions, upslope area is calculated by apportioning the flow from a pixel between the two downslope pixels according to how close the flow angle is to the direct angle to that pixel center. These eight planar triangular facets are formed between the pixel and its eight neighbors. Each having a downslope vector which when drawn outwards from the center may be at an angle that lies within or outside the 45° ($\pi/4$ radians) angle range of the facet at the center point. If the slope vector angle is within the facet angle it represents the steepest flow direction on that facet. If the slope vector angle is outside a facet the steepest flow direction associated with that facet is taken along the steepest edge.

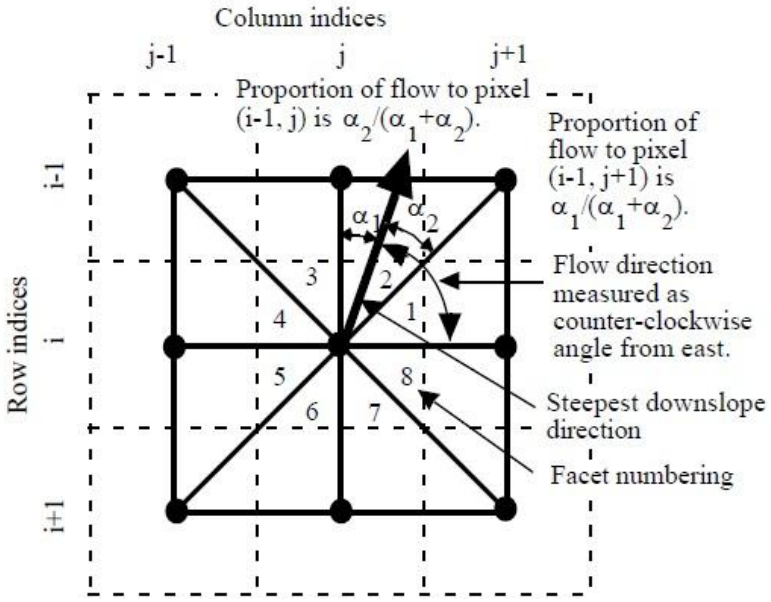

Figure 2.13 - Flow direction defined as steepest downward slope on planar triangular facets on a 3x3 cells grid. (Tarboton, 1997).

Since only a single number need to be saved for each pixel to represent the flow field, computer storage is simple and efficient. Some dispersion is introduced by the proportioning of flow between downslope pixels, but this is minimized since flow is never proportioned between more than two downslope pixels (Tarboton, 1997).

In the case where no slope vectors are positive (downslope) a flow direction angle of -1 is used to flag the pixel as "unresolved", i.e. a flat area or pit. Unresolved flow directions are resolved iteratively by making them flow towards a neighbor of equal elevation that has a flow direction resolved. This ensures that flat pixels drain to a neighbor that ultimately drains to a lower elevation, eliminating the possibility of inconsistencies such as loops in the flow direction angles (Tarboton, 1997). Some comparisons between the different algorithms can be evaluated looking at *Figure 2.14* which shows the influence maps for each of the five algorithms applied to the inward circular cone. The D8 method produces no dispersion, but flow paths result constrained to grid directions, while the MultiFlow follows the topographic slope but introduces substantial dispersion. Lea's method results in a stair step path roughly perpendicular to the contours, whereas DEMON and D∞ create a compromise with spreading slightly wider than divergence perpendicular to the contours. It could happen that for some pixels D∞ results in no spreading. In general when the topographic slope is aligned with the grid axes, cardinal or diagonal, the D∞ procedure gives the same results as D8, and both are correct. However when the topographic slope is not aligned with one of the grid directions,

the procedures differ. D8 introduces no dispersion, but at the expense of grid bias. D∞ follows the topographic slope at the cost of introducing some dispersion, which is in any case minimal because the algorithm allows the flow to be partitioned in no more of two downslope cells.

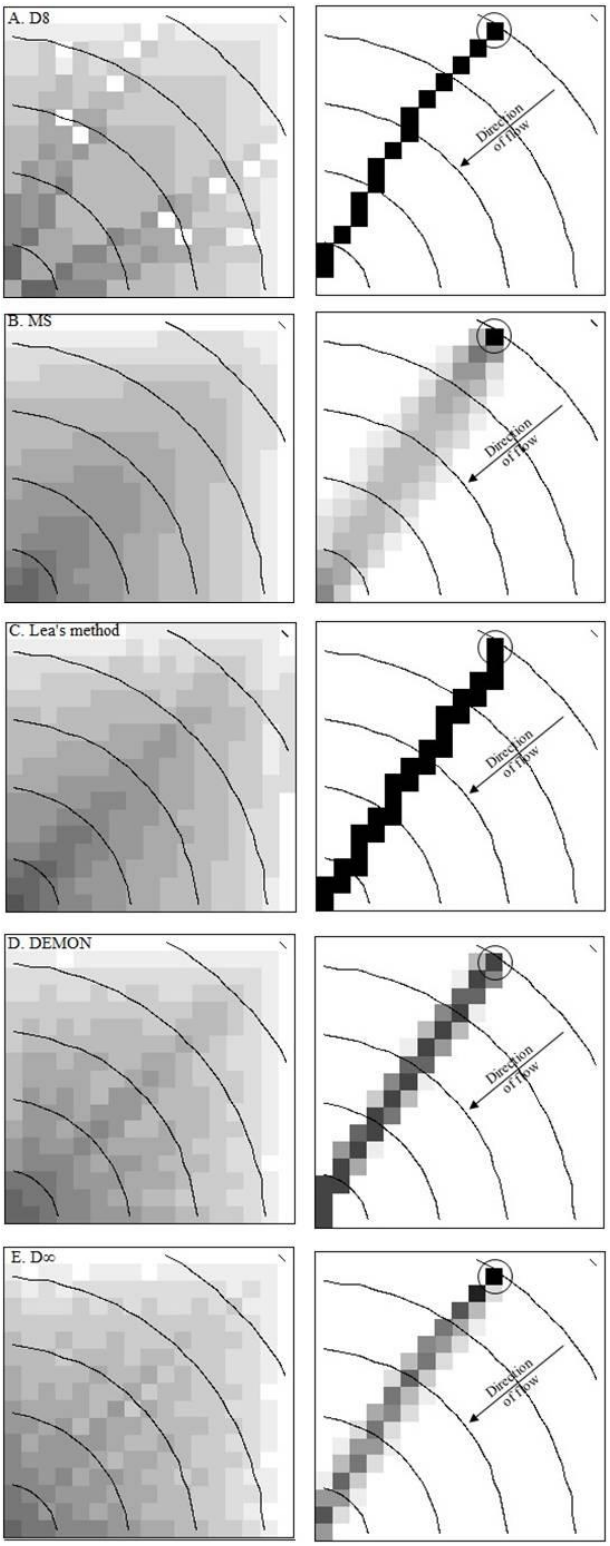

Figure 2.14 - The left panel shows upslope area in grayscale. The right panel shows the influence function from the circled pixel. A. D8 method, B. MS method, C. Lea's method, D. DEMON method, E. D∞ method. (Tarboton, 1997).

For this reasons the D∞ method represented a good compromise to compute flow directions, local slope and upslope drainage area, by using the TauDEM 5.0 Toolbox applied to the ArcGIS 10.1 software.

2.3.4 Specific Catchment Area

The specific catchment area (SCA) is defined by Moore et al. (1991) as the total upslope catchment plan area draining across a unit length of contour. This useful morphometric parameter is estimated as follows:

$$SCA = \frac{A}{L} \tag{2.10}$$

where L is the cell size. Specific catchment area can also be interpreted as a characteristic length or extent of the upslope catchment area for the processes controlling the lateral response of the catchment (Chirico et al., 2005). Upslope area and specific catchment area have both a key role in hydrologic and geomorphologic studies. Upslope drainage area is commonly used for the automatic demarcation of channels relying on the notion of a critical support area (O'Callaghan and Mark, 1984; Jenson and Domingue, 1988; Morris and Heerdegen, 1988; Tarboton, 1989; Lammers and Band, 1990; Tarboton et al., 1991; Tarboton et al., 1992; Martz and Garbrecht, 1992). While specific catchment area patterns, combined with other variables, such as other terrain attributes or soil–vegetation properties, are commonly used in hydrological and geomorphological applications (Chirico et al., 2005). Having said that, it is evident the relevance of an accurate computation of deterministic quantities such as upslope and specific catchment areas. The above-mentioned computation should be pursued in a repeatable way.

2.3.5 Landform curvature

Landform curvature is another morphometric parameter extremely useful for the interpretation of dominant sediment transport process on the landscape (Bogaart and Troch, 2006, Lashermes et al., 2007; Istanbulluoglu et al.,2008; Tarolli and Dalla Fontana, 2009; Yetemen et al., 2010). Considering the DTM surface to be approximated through a bivariate quadratic function (Evans, 1979), where x, y, and z are local coordinates, and a to f are quadratic coefficients as expressed by *Equation 2.11*,

$$z = ax^2 + by^2 + cxy + dx + ey + f \quad 2.11$$

landform curvature (*C*) can be recognized as the second derivative of the terrain elevation (*z*) or its Laplacian (*Equation 2.12*).

$$C = \nabla^2 z \quad 2.12$$

According to Wood (1996), "*if we wish to create a single measure of the second order derivatives we must derive that measure for an intersecting plane so as to reduce the expression to an ordinary differential one. Thus we have several choices depending on the orientation of this intersecting plane*". Nevertheless, the two most frequently calculated forms are profile and plan curvature (Gallant and Wilson, 2000; Pirotti and Tarolli, 2010). From a morphological point of view, plan curvature $\left(\frac{\partial^2 z}{\partial x^2}\right)$ represents the degree of terrain divergence or convergence perpendicular to the flow direction, while profile curvature $\left(\frac{\partial^2 z}{\partial y^2}\right)$ represents the terrain convexity or concavity along the flow direction. If considered as a whole, these two quantitative parameters describe what is known as total curvature ($\nabla^2 z$), which can be expressed by *Equation 2.13*.

$$\nabla^2 z = \left(\frac{\partial^2 z}{\partial x^2} + \frac{\partial^2 z}{\partial y^2}\right) \quad 2.13$$

In general terms, divergent-convex landforms ($\nabla^2 z < 0$) are associated with the dominance of hillslope/diffusion processes, while concave-convergent ($\nabla^2 z > 0$) landforms are associated with fluvial-dominated erosion (Yetemen et al., 2010). The profile curvature is the curvature of the surface in the steepest downslope direction. It describes the rate of change of slope along a profile in the surface and may be useful in highlighting convex and concave slopes across the DTM. The plan curvature is the curvature of a contour drawn through the central pixel. It describes the rate of change of aspect in plan across the surface and may be useful in defining ridges, valleys and slopes along the side of these features (Pirotti and Tarolli, 2010). Moreover, based on Evan's bivariate quadratic function (*Equation 2.11*), Wood (1996) proposed a multiple-scale parameterization and implemented it in the LandSerf software. He generalized the calculation of minimum and maximum profile convexity for different window sizes, by adopting two factors *g* and *n* corresponding respectively to the grid resolution of the

DEM and to the size of the moving window (kernel), which resulted in *Equations 2.14* and *2.15*.

$$profc_{MAX} = n * g\left(-a - b + \sqrt{(a-b)^2 + c^2}\right) \quad 2.14$$

$$profc_{MIN} = n * g\left(-a - b - \sqrt{(a-b)^2 + c^2}\right) \quad 2.15$$

To the purpose of this work, a generic parameter considering both planar and profile curvatures has been chosen to analyze the landform surface (*Equation 2.16*). This parameter has been referred to as "mean curvature" and it has been computed using the LandSerf 2.3 software. Mean curvature is described by Wood (1996) as a measure of the average curvature for specific cells (the average of the maximum and minimum curvature for that cell) or even the mean value over all cells in a grid. This is expressed by the following formula:

$$C_{MEAN} = \frac{C_{MAX} + C_{MIN}}{2} \quad 2.16$$

Mean curvature provides for a general curvature in any plane considering both the profile and plan components; in particular, positive values of C_{MEAN} correspond to convex morphologies, while negative values are associated to concave surfaces.

Morover, the calculation of mean curvature has to be performed through the use of a moving window (kernel) whose size has to be defined prior to proceed with terrain analysis according to the scale of the elements that are going to be investigated. To this regard, Pirotti and Tarolli (2010) stated that more detail do not imply a better accuracy because methods are not necessarely sensitive to a greater level of details. Their results showed how important is to best select the window size for curvature computation in the recognition of morphological features and channel networks in mountain basins. Accordingly, they identified for alpine basins where channels present a bankfull width ranging from 1 to 5-6 m, an optimal kernel scale of at least three times the features width. That consisted in a window size of 15x15 pixels, which corresponded to a 15 m curvature scale. Therefore within this study, the choice of the moving window relative to the mean curvature analyzed for different DTMs' resolutions of each study area, has been based on the Pirotti and Tarolli (2010) findings.

2.3.6 Topographic Wetness Index

Among the secondary topographic attributes one of the most commonly used is the topographic wetness index (TWI), first developed by Beven and Kirkby (1979). It can quantify the effect of topography on runoff generation and serves as a physically-based index in approximating the location of zones of surface saturation and the spatial distribution of soil water (Beven and Kirkby 1979; O'Loughlin 1986; Barling et al. 1994). This topographic index has been implemented in various hydrologic models such as TOPMODEL (Beven and Kirkby, 1979). In this rainfall-runoff model the topographic index represents the extension of saturated areas and the spatial variation of soil moisture and groundwater levels. TOPMODEL in turn, has been used for studying several hydrologic processes such as flood frequency (Beven 1987), flow paths (Beven and Wood 1983, Quinn et al. 1991) and water quality (Wolock et al. 1989, 1990) but also to represent the hydrologic variable in models to study photosynthesis and annual net primary production (White and Running, 1994), carbon budgets (Band 1993) and vegetation patterns (Moore et al. 1993; Zinko et al. 2005).

Topographic Wetness Index (TWI), as presented by Beven and Kirkby (1979) is derived by a combination of the primary attributes specific catchment area (SCA) and local slope gradient, as specified in *Equation 2.17.*

$$TWI = ln\left(\frac{a}{tan\beta}\right) \qquad 2.17$$

Where a is the upslope drainage area per unit contour length (or specific catchment area, as previously described) and $tan\beta$ is the local slope gradient for estimating a hydraulic gradient. This formula assumes steady-state conditions and uniform soil properties, in particular transmissivity (the vertical integral of hydraulic soil conductivity along depth) is considered as constant throughout the catchment and equal to one.

To the purpose of this thesis, the TWI has been analyzed together with aspect, slope gradient, profile curvature and specific catchment area calculated from the DTMs of the two study areas to analyze the spatial variability of vegetation distribution.

2.4 S-A and C-A relationships

Some of the parameters introduced before have been related to each other in past studies in order to examine landscape morphology and its mutual ecological and geomorphologic implications. In particular, since the increasing availability of high resolution topographic data, two suggestive relations (slope-area and curvature-area relations) have been several times reckoned with to investigate many different, though interconnected, themes.

Among others, Tarolli, Istanbulluoglu and Dalla Fontana (2006) investigated the spatial distribution of different vegetation types in relation to the landscape morphology by giving an interpretation of the slope-area and curvature-area relations. Besides, Yetemen, Istanbulluoglu and Vivoni (2010) examined the relationship between land surface properties, in particular soil, vegetation and lithology, and landscape morphology, quantifying it by catchment descriptors such as slope-area relation, curvature-area relations and the cumulative area distribution.

2.4.1 Slope-Area relation

Slope-area relationship methodology is based on a power-law relation between the local slope of a given point on the landscape (S) and its contributing area (A), expressed as in *Equation 2.18*:

$$S = kA^{\theta} \tag{2.18}$$

where k is the steepness index and θ is the concavity index, which could also be referred to as the gradient (degree of steepness) of the slope-area relation in a log-log plot (Yetemen et al., 2010).

In an idealized soil-mantled (transport-limited) equilibrium landscape, the slope-area relation can be described by the following generic Geomorphic Transport Law that specifies sediment transport capacity (Q_s) as:

$$Q_s = KA^m S^n \tag{2.19}$$

where K is an empirical transport efficiency coefficient that considers climatic factors and erodibility, while m and n are parameters varying with different erosion processes (Kirkby,

1971). Moreover, assuming that rock uplift and erosion rates are in balance, which is also the most general criterion for steady-state topography, then the local sediment transport rate must equal the product of the rock uplift (U) and the contributing drainage area (A), accordingly to *Equation 2.20* (Howard, 1994; Montgomery, 2001).

$$Q_s = UA \tag{2.20}$$

To what concerns transport-limited erosion, it is possible to combine *Equations 2.18* and *2.20* so that local slope can be expressed as a power function of drainage area, as in *Equation 2.21* (Montgomery, 2001).

$$S = \left(\frac{U}{K}\right)^{\frac{1}{n}} * A^{\left(\frac{1-m}{n}\right)} \tag{2.21}$$

Comparing *Equation 2.21* with *Equation 2.18* it appears that k and θ parameters can be written respectively as in *Equations 2.22* and *2.23*.

$$k = \left(\frac{U}{K}\right)^{\frac{1}{n}} \tag{2.22}$$

$$\theta = \frac{(1-m)}{n} \tag{2.23}$$

In this way, it is easier to notice how a variation in parameters could affect erosion processes. To this regard, Yetemen et al. (2010) observed sediment transport in soil-mantled hillslopes, where runoff is not erosive, to be characterized by a transport-limited slope-dependent diffusive process, with $m = 0$. This leads to a positive relationship between local slope and drainage area ($\theta > 0$) in *Equation 2.21*, suggesting a convex hillslope morphology. Conversely, for fluvial sediment transport, results to be m and $n > 1$, so that *Equation 2.21* predicts an inverse relationship for S and A ($\theta < 0$), representing a concave upward channel profile. To this regard, Smith and Bretherton (1972) suggested an explanation for the origins of ridges and valleys to be produced by the competition among the aforementioned opposite erosion processes. According to their opinion, Dietrich and Perron (2006) proposed in their review a graphical interpretation of the transport laws role in shaping the landscape. This is reported in *Figure 2.15*.

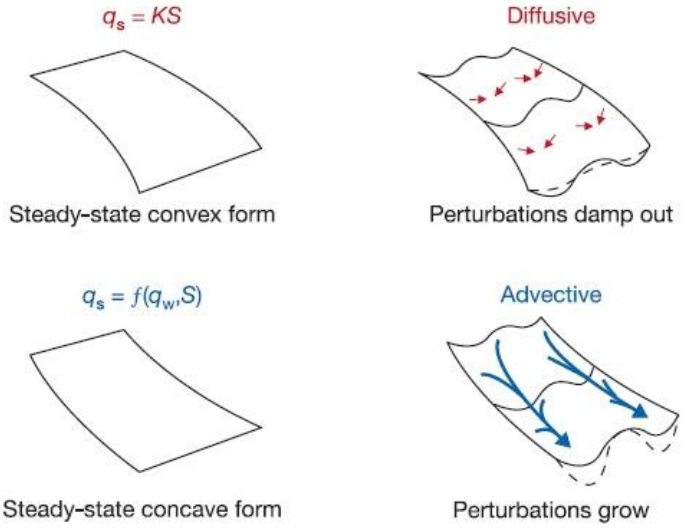

Figure 2.15 - Slope-dependent (diffusive) transport leads to convex hillslopes, and when the topography is laterally perturbed, the transport direction (red arrows) causes the high points to lower and low points to fill in. This results in smooth topography, as suggested by the dashed line. In contrast, transport that depends on water flow and slope advects sediment, and produces concave-up hillslopes. Flow concentrations (blue flow paths) resulting from lateral topographic perturbation lead to incision, as suggested by the dashed lines. The competition of these two processes leads to diffusion-dominated ridges and advection-dominated valleys (Dietrich and Perron, 2006).

Since, for soil-mantled landscapes, a slope-dependent critical support area has been both theoretically and empirically proven to be a more appropriate approach to channel network extraction from DTMs, which is consistent with the assumption that channel head represents an erosional threshold and hence a change in sediment transport processes, Montgomery and Foufoula-Georgiou (1993) proposed a landscape partitioning into drainage area and slopes regimes. The four different landscape regions are shown in *Figure 2.16*: hillslopes, unchanneled valleys, debris-flow dominated channels and alluvial channels.

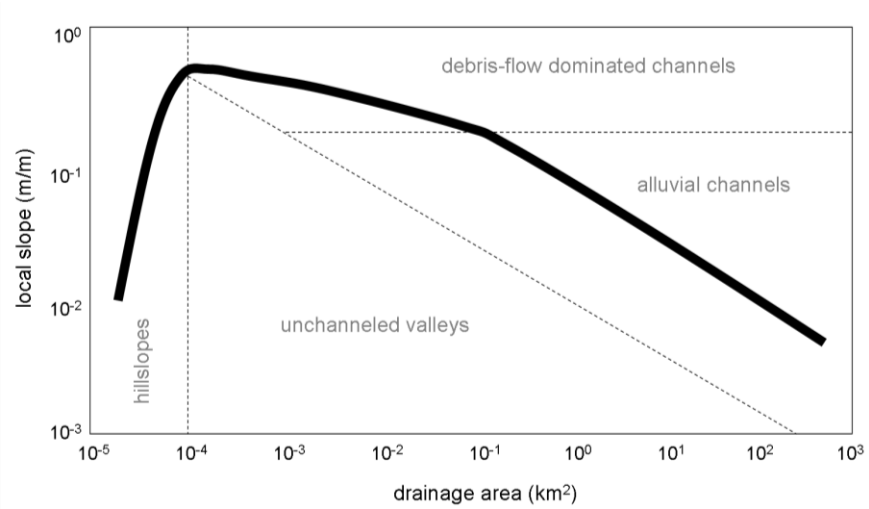

Figure 2.16 - Schematic illustration of relations between drainage area and local slope depicting hillslope to valley transition and the channel initiation criteria (Montgomery and Foufoula-Georgiou, 1993).

Looking at figure 15, two inflections of the curve are evident: the first one (occurring in this case at about 10^{-4} km^2) corresponds to the hillslope to valley transition, while the second one (presented at about 10^{-1} km^2) is related to the transition from a debris-flow dominated morphology to a channelized one. In conformity to this interpretation, many researchers focalized their attention on the slope-area relation. According to some of whom, results consisted in the identification of four distinct scaling regimes in the slope-area diagram that depict the change from diffusive to fluvial sediment transport processes (Ijjaz-Vasquez and Bras, 1995), or in the determination of topographic thresholds to define erosion-landsliding processes (Tucker and Bras, 1998), as well as in the acknowledge of topographic signature of valley incision by debris-flows (Stock and Dietrich, 2003).

Scaling regimes proposed by Ijjaz-Vasquez and Bras (1995) consisted in the individuation in the S-A plot of four distinct regions according to the increasing order of contributing area: a small Region I exists at low value of upslope area presenting a positive gradient; in Region II the gradient turns negative; in Region III the gradient, although still having a negative value, is much smaller; and in Region IV the gradient goes back to a larger negative value. Tarolli and Dalla Fontana (2009) underlined that the transition between regions I and II is related to the change of dominance from hillslope/diffusive sediment transport to unchanneled valleys; while Region III is related to the dominance of debris flows and landslides and Region IV to the dominance of alluvial channels.

It is also important to bear in mind that the slope-area relationship, as well as other topography-based analysis, is strongly influenced by DTMs resolution, since this involves issues of both high resolution data availability and accuracy of feasible results. Outcomes from Tarolli and Dalla Fontana (2009) attested the necessity of high resolution DTMs (1-5 m cell size) for a better interpretation of the hillslope to valley transition based on the slope-area relationship; moreover, raster resolutions finer than 10m allowed the identification of topographic signature of valley incision by debris flows and landslides from the S-A plot, which otherwise would disappear with higher resolution DTMs. This is consistent with findings by previous researches on the effects of DTM resolutions on geomorphology. Indeed, Montgomery and Foufoula-Georgiou (1993) remarked in their conclusions that a higher-resolution grid size (< 30 m) data available may be required to derive the hillslope to valley transition from the S-A plot; also Zang and Montgomery (1994) observed that grid size

influenced physically-based models of runoff generation and surface processes and proposed a 10m cell size as a rational compromise.

The slope-area relationship methodology has been also used in more recent studies for landscape evolution modeling. To this regard, it is remarkable the investigation by Istanbulluoglu and Bras (2005) about the effects of vegetation on thresholds for channel initiation, which suggests that, under steady uplift, vegetation may change dominant erosion process from wash to landsliding due to stampeding of vegetated slopes (Tarolli et al., 2006).

2.4.2 Curvature-Area relation

The aforementioned landscape curvature is well known in the literature for its role in the curvature-area relation that is often associated to the slope-area relation for the analysis of landscape morphology; the C-A relation indeed, can contribute to an useful interpretation of dominant landform processes (Lashermes et al., 2007; Istanbulluoglu et al., 2008).

As already stated, Yetemen et al. (2010) used this C-A relation in their work and found out a correlation between the change in the sign of curvature plotted in relation to drainage area that approximately corresponds to the S-A turnover point from hillslope to valley morphology. This is also consistent with what is affirmed by Montgomery and Foufoula-Georgiou (1993) about the corresponding location of the valley head to a transition from divergent to convergent morphology.

From an analytical point of view, this concept can be expressed in general terms as in Tarolli and Dalla Fontana (2009), where divergent-convex landforms are associated with dominance of hillslope/diffusion processes, while convergent-concave landforms are associated with fluvial-dominated erosion. Moreover, Yetemen et al. (2010) also observed a global maximum in the C-A relationship within the concave portion of the landscape, but this did not find a repercussion on the related slope-area plot, suggesting for this maximum point to be the result of an initial increasing and a subsequent decrease in landform curvature with drainage area.

In their analysis over different DTMs resolutions, Tarolli and Dalla Fontana (2009) also underlined the relevance of the availability of high resolution DTMs to obtain correct curvature values. Their results showed a progressive decrease of curvature values and a progressive shift towards divergent/hillslope topography as grid resolution decrease; as well as an increasing number of channel heads located in divergent/hillslopes zones, that is inconsistent with data from higher resolution DTMs, which locates almost all channel heads

in convergent/channeled zones. This interpretation is in agreement with the assumption from Montgomery and Foufoula-Georgiou (1993) that considers channel head representing of a change in sediment transport processes, other than an erosional threshold.

The transition from convex to concave slope profiles commonly coincides with the transition from divergent to convergent topography, suggesting that constant-threshold models are more appropriate for representing controls on valley development than for channel initiation (Dietrich and Dunne, 1993; Montgomery and Dietrich, 1994; Montgomery and Foufoula-Georgiou, 1993).

3 STUDY AREAS DESCRIPTION: THE MIOZZA AND CETUS CASE STUDIES

The study areas of the Miozza and the Cetus basins have been chosen for specific reasons. To the purposes of this thesis work, that investigates the relations between vegetation distribution patterns and the morphology of the study areas, it has been supposed to be interesting to compare the analytic results of two distinct locations within the Italian territory. Different geographic positions, lithologies, moisture regimes and climatic conditions characterize the studied basins, so that the analysis of their vegetation dynamics could highlight or exclude eventual correspondences that could link vegetation patterns to the topographies of each basin. To this extent it is important to note that the two catchments present contrasting ecological features, ranging from the high elevation and humidity alpine environment of the two study areas within the Miozza catchment, to the Mediterranean xeric environment of the coastal hillside, which defines the Cetus basin. To the aim of this analysis, a classification of vegetation typologies has been carried out specifically to each basin.

3.1 Miozza basin: general characteristics

The Miozza catchment is located in North-eastern Italian Alps, within the Carnia region, more precisely it falls within the Ovaro and Raveo municipalities (Udine province) in the Friuli Venezia Giulia Italian region. Within this basin two study areas have been identified: the headwater catchments "A" and "B" (*Figure 3.1*), which will be separately described in *Paragraphs 3.2* and *3.3*.

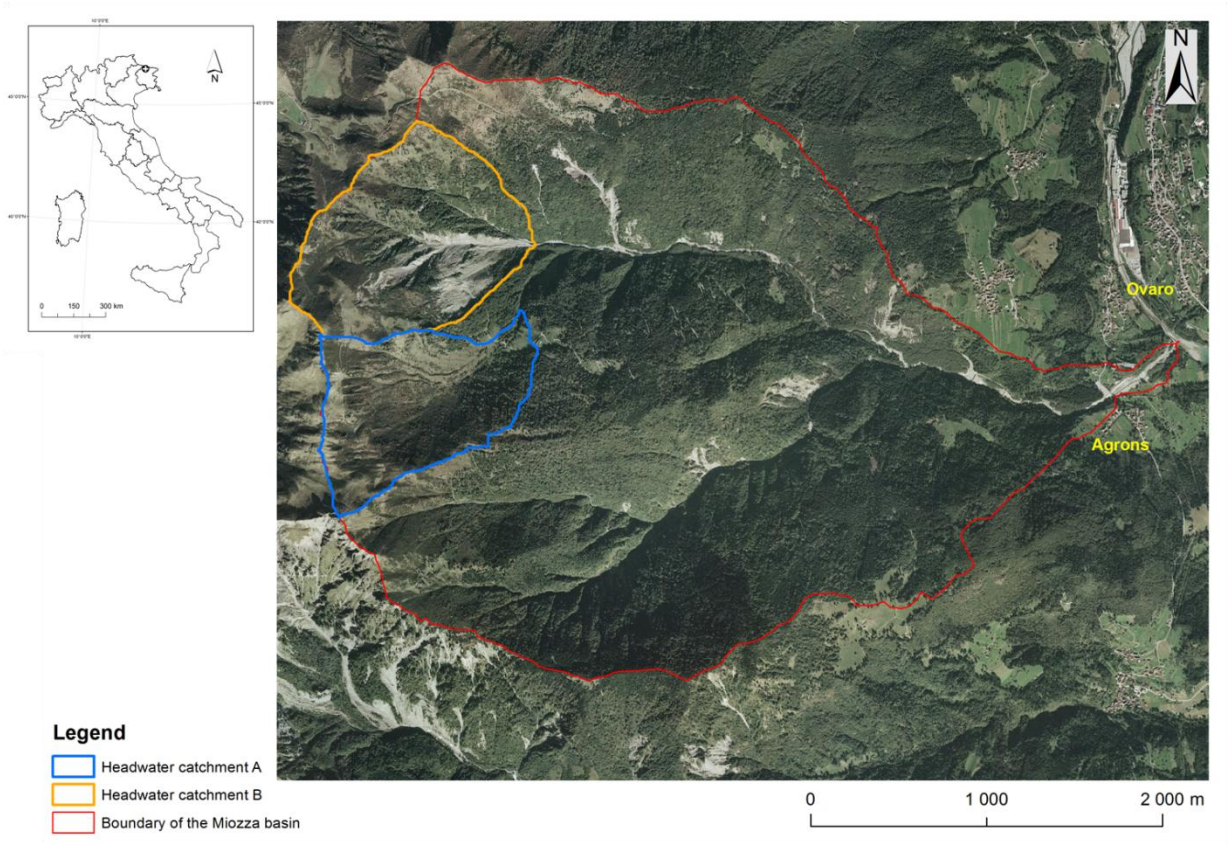

Figure 3.1 - Overview of the Miozza catchment and its sub-basins A and B.

The Miozza stream is a feeder of the Degano stream, which in turn is an affluent of the Tagliamento river, so that they are included in the Tagliamento mountain basin.

The catchment is delimited from the M. Forchia ridge on the South-Western side and from the Col Gentile ridge on the North-Eastern side. The overall surface of the basin is about 10.69 Km^2, while its perimeter is around 14780 m. The main stream branch is 5200 m long and its most consistent affluent is the Rio d'Archia, which presents a sub-basin area of 3.99 Km^2 and joins the main stream on the orographic right side at an elevation of 640 m a.s.l.. Other less consistent feeders are the Rio Giaf, the Rio Pertia and the Rio Valinia on the orographic right side of the main stream, as well as the Rio Venchiaruz on the orographic left side. *Table 3.1* summarizes the main morphometric characteristics of the basin.

Table 3.1 - General morphometric characteristics of the Miozza basin

Area	13.693 km^2
Minimum elevation	516.03 m a.s.l.
Average elevation	1268.33 m a.s.l.
Maximum elevation	2124.24 m a.s.l.
Minimum slope	0.014 °
Average slope	33.05 °
Maximum slope	75.15 °

The landscape presents different kinds of features: from steep ridges of the Col Gentile mountain to smooth valleys and grasslands, going through steep slopes and gully landforms often signed by debris flows scars and ephemeral streams. In addition, the effects of human presence due to the traditional rural activity and seasonally used housing settlements are both well visible on the landscape. Furthermore, the presence of environmental engineering structures such as dams and embankments are as well an hint to understand how this area had been managed in the past decades. It is conceivable that the agricultural and farming use of the basin area had been kept alive till the second half of the last century, but, nowadays, a low intensity wood harvesting practice and a seasonal grazing are still operating only for the most accessible areas. Nevertheless, some areas of the basin are also in range of tourism and recreational activities, thanks to the presence of hiking trails, grazing paths and many forest roads and secondary municipal roads.

3.1.1 Geological characteristics

The geologic map of the basin has been extracted from the paper "Carta geologica delle Alpi Carniche" (Venturini, 2001). The main sediment type consists in terrigenous rocks, which can be related to the subsequent formations, also represented in *Figure 3.2*:

- Bellerophon formation (Upper Permian): it is only present the Bellerophon component made of Dolomites and Black Limestone, which is located both along the left side of the Miozza stream and on the medium-lower section of its main affluent Rio d'Archia;
- Werfen formation (Scythic - Lower Triassic): it is an heterogeneous formation consistent in limestones, marly limestones, sandstones and red mudstones, it is mainly present on the upper-medium section of the basin;

- Sciliar's Dolomite (Anisiac - lower stage of the Middle Triassic): it is composed by dolomites and limestones and it is only present along the right side of the Rio d'Archia, where it joins the Miozza;
- Val Degano formation (Carnian - lower stage of the Upper Triassic): calcareous marlstones and black limestones components characterize the basin's outlet area;
- Durrestein formation (Carnian - lower stage of the Upper Triassic): it is composed by limestones, dolomites and purple sandstones and it constitutes the rocky buttress to the northern side of the basin's outlet;
- Raibl formation (Carnian - lower stage of the Upper Triassic): it is only represented by rare outcrops of the red mudstones component;
- Alluvial covering layer: it characterizes the remaining area of the basin (about 40%) and consists of ground moraine deposits and screes.

Moreover, the upper-medium section of the Miozza's riverbed is located along one of the fault plans of the Sauris' line. This southward tectonic line which mainly goes along the East-West direction causes the thrust faulting of the Permian-Scythian rocks over the Carnian rocks.

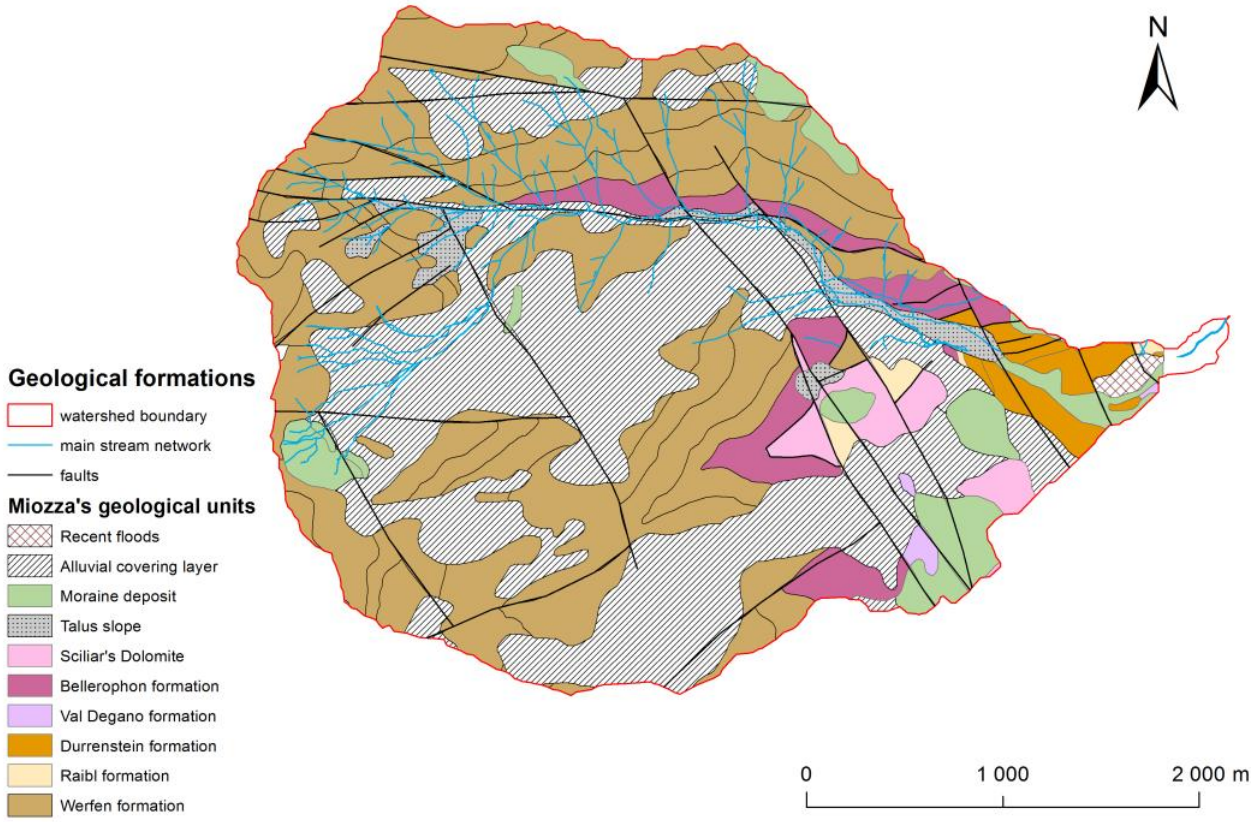

Figure 3.2 - Geologic map of the Miozza basin (modified from the *"Carta geologica delle Alpi Carniche"* -scale 1:25000- Venturini, 2001).

3.1.2 Geomorphology of the basin

The geomorphologic setting of the basin is typical of the Eastern Alpine region, with deeply incised valleys. Soil thickness varies between 0.2 m and 0.5 m on topographic spurs to depths of up 1.5 m in topographic hollows. Part of the soil of Miozza basin is characterized by morain formations with vegetated talus deposits. To this regard, looking at the upper part of the basin, three glacial cirques with their ground moraine and terminal moraine deposits can be recognized.

Werfen formation's rocks, which characterize the head of the basin, are very disjoined, highly erodible rocks; this is also due to the presence of numerous faults. In the specific case, the Miozza stream originates from a wide dissected area (0.22 km^2) with an average slope of 39° which can still be visible in *Figure 3.3*.

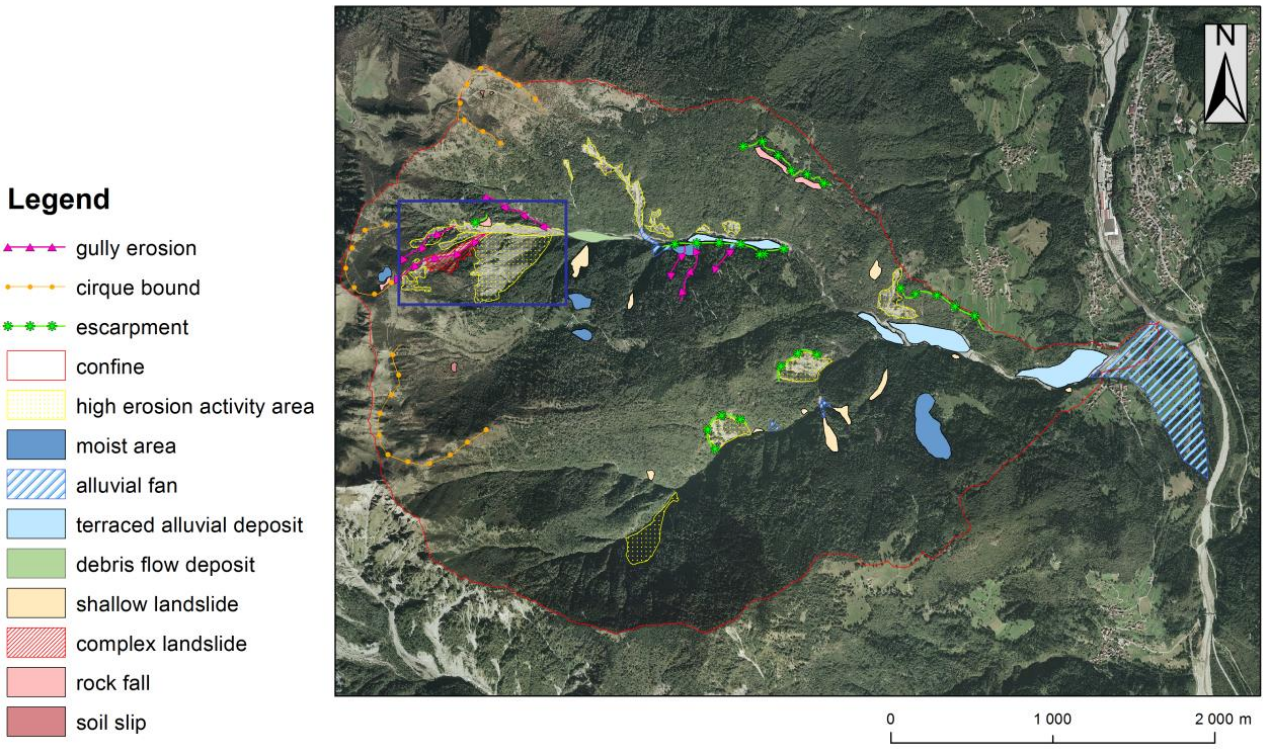

Figure 3.3 - Geomorphologic map of the Miozza basin with a detail (blue squared area) of the spring of the Miozza stream.

This area supplies material for sediment transport processes that involve debris flow mechanisms, as can be detected by the presence of rambling rounded deposits on the medium-low elevation storage areas.

High erosion processes are mainly caused by the very steep slopes, the brittle behavior of rocks due to their geology and tectonic, and also by the high level of annual precipitation. All these factors lead to the production of available material for sediment transport. As a consequence, many debris flow events occurred during the last century, also causing damages to the restoration works previously arranged. Currently, debris flows are arrested by a series of retention check dams located along the main stream plus one at the head of the alluvial fan, which hold most of the sediment transported through the valley, also protecting the Agrons village placed within the alluvial fan area.

Many small channels rise at the head of the basin, contributing to the main stream which is characterized by an upper section with steep slope and a positive proportion between erosion and depositional processes, and a lower section with smoother slope and larger riverbed width. This section is arranged with restoration works constructed at different times and with various constructional characteristics. The first works were built during the '30s, made by stone masonry, but they were partially injured by the 1966 flood event. The same works were

repaired or substituted with concrete during the '70s. A wide depositional area has been located before a huge check dam, built after the 1983 flood event, to protect the alluvial fan that characterizes the last section of the Miozza stream.

The major debris flow events occurred between October 31st and November 1st in 2003 and on March 25th-26th in 2005, causing the detachment of a huge amount of material from the valley head which settled at an elevation of about 600 to 900 m. Concerning this, it is also important to remember, as Tarolli and Tarboton (2006) stated, that the occurrence of landslides in complexes is not the result of a specific rainstorm event, but a combined effect of different events including both extreme short rainfalls, low intensity long duration rainfalls, and snow melt.

3.1.3 Climatic conditions

To better understand the climatic condition of the study area it is important to partially introduce the geography and orography of the Friuli Venezia Giulia region.

The region is geographically located between the Adriatic sea and the Alps in the South-North direction, while in the West direction is opened toward the Po valley, while other Alpine ridges and the early Balkan ridges can be found on the East side. The Alpine System protects it from the direct impact of the rigid northerly winds, but the region, opening toward the Po Valley, is influenced by the general circulation of air masses from the west to the east. Along this direction, the low pressure centers develop and move, bringing with them thunderstorms and hailstorms, especially in the summer. Being open to the Adriatic Sea, the territory also receives Sirocco winds, that bring with them heavy rainfall.

The orography of the region, characterized by the presence of Pre-Alps and Alps (Carnic and Julian Alpine regions), also amplifies the effects of the Mediterranean moist air fluxes by rising up them with the help of quite intense southern wind blow. Especially in the summer season, warm and moist air masses move from the Adriatic sea and the Po Valley and meet the much cooler air coming from northern regions, causing thunderstorms.

According to this overview on the climate of the Friuli Venezia Giulia region, the area of interest of the Miozza basin, can be described as having a typical North-Eastern Alpine climate with short dry periods and high intensity rainfall events, with extreme temperature range. Mean annual precipitation is about 2200 mm, since recorded annual precipitation ranges from 1300 to 2500 mm. Precipitation mainly occurs as rainfall from October to

November and from April to May, while it becomes mainly snowfall from November to April; consequently, runoff is usually dominated by snowmelt in May and June. During summer, flash floods with heavy solid transport frequently occur, while in autumn high discharges associated to long low intensity rainfall periods characterize the flow regime.

3.1.4 Vegetation and soil use description

The vegetation cover map for the Miozza basin was already been created as the basis for previous studies on the same study area (Tarolli et al., 2006; Tarolli, 2007). It was been realized through the LiDAR-derived DSM at 3 m resolution, on the base of a double check comparison between the soil use map of the Miozza basin (Regione Autonoma Friuli Venezia Giulia - Direzione Centrale Risorse agricole, naturali, forestali e montagna, 2000) (*Figure 3.4*) and the orthophoto IT2000, whit the help of some field observations.

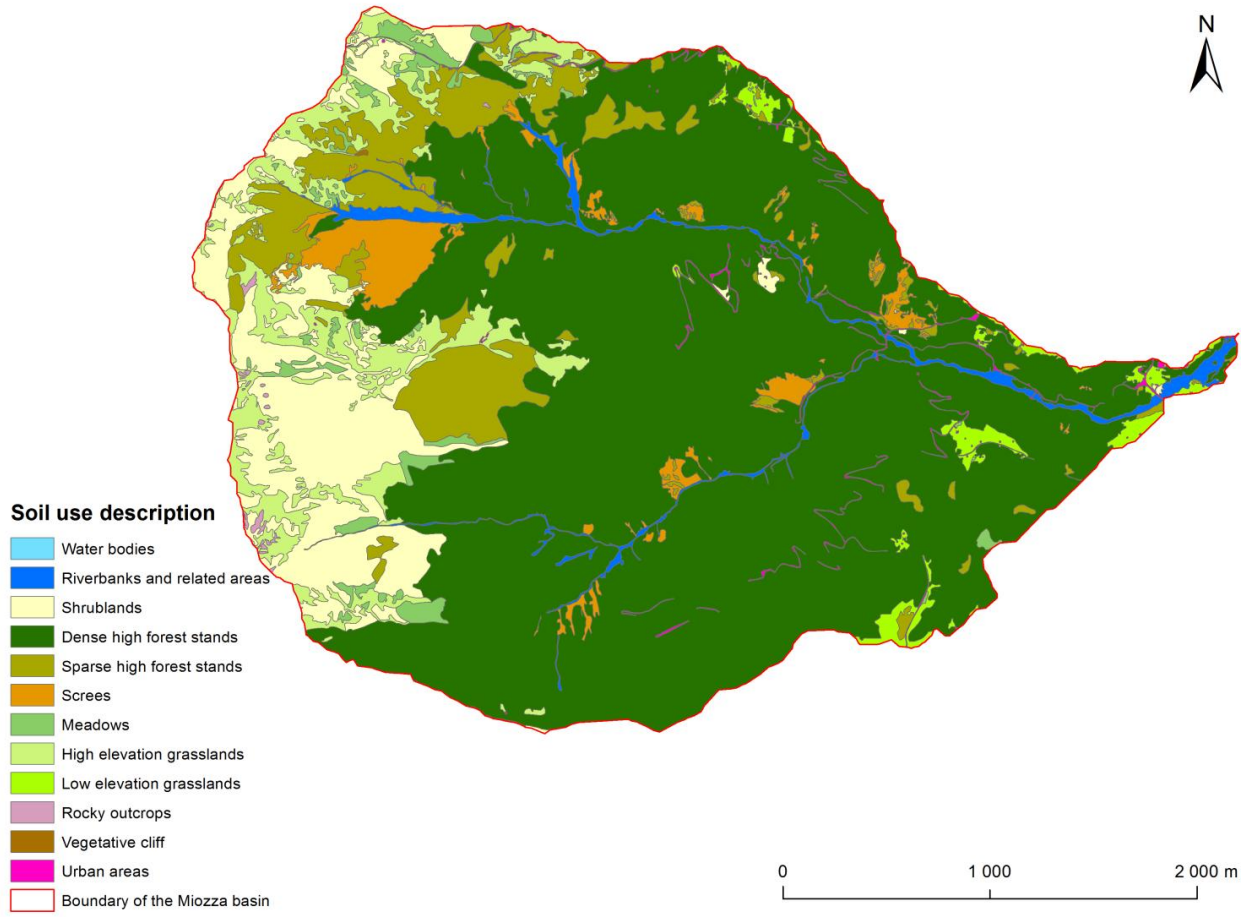

Figure 3.4 - Soil use description for the Miozza basin. Regione Autonoma Friuli Venezia Giulia - Direzione Centrale Risorse agricole, naturali, forestali e montagna.

The soil coverage results to be characterized by three vegetated classes:

- woodland (73 % of the basin area), composed by dense and sparse high forests;
- shrubland (18.5 % of the surface), composed by shrubs, meadows planted with trees and high elevation grasslands;
- grasslands (2,5 %), mainly located in the lower part of the basin.

Other less represented coverage areas are screes (3 %), urban areas (1 %) and water bodies (2 %). This soil use classification supports the vegetation classification that will be later reported.

Vegetation species most present in the wooded areas are the Norway Spruce (*Picea abies* (L.) H.Karst.) and the European Beech (*Fagus sylvatica* (L.)), which characterize the "Piceo-Faggeto of mesic soils and of the mountainous altitudinal range" according to the forest type map of the Miozza basin (Carta dei tipi forestali del bacino del torrente Miozza. Regione Autonoma Friuli Venezia Giulia - Direzione Centrale Risorse agricole, naturali, forestali e montagna, 1998). Many typical species of this forest type can be found moving upward along the main stream branch. In fact, in the lowest section of the basin are located the mixed mesotermophilous deciduous woods, composed by species such as *Ostrya carpinifolia* (Scop.), *Fraxinus ornus* (L.), *Quercus robur* (L.), *Fagus sylvatica* (L.), *Fraxinus excelsior* (L.), *Acer pseudoplatanus* (L.), *Cornus mas* (L.), *Ligustrum vulgare* (L.), *Corylus avellana* (L.) and *Lonicera* (L.) *spp.* At the intermediate elevations can be found pure Beech forests or Spruce-Beech mixed forests, which are combined with European Mountain-ash (*Sorbus aucuparia* (L.)) and Sycamore Maple (*Acer pseudoplatanus* (L.)). Moreover, the Green Alder (*Alnus viridis* (Chaix. DC)) shrubsland succeeds to the upper limit of the sub-Alpine Spruce forest and still at higher elevations can be found some colonization units of European Larch (*Larix decidua* (Mill.)). In particular, the Green Alder shrubsland generally originates, thanks to the pioneering behavior of this species, over earth movements and dissected areas, which are previously colonized by pioneering herbaceous species, such as *Tussilago farfara* (L.) and *Calamagrostis villosa* (Adans.), and also by some Willow species (*Salix* (L) *spp*.). On the North-facing slopes, the Green Alder tends to colonize mounds where the snowmelt begins before other areas; whereas on South-facing slopes, it better penetrates along hollows and small valleys, where water is more available (*Figure 3.5*).

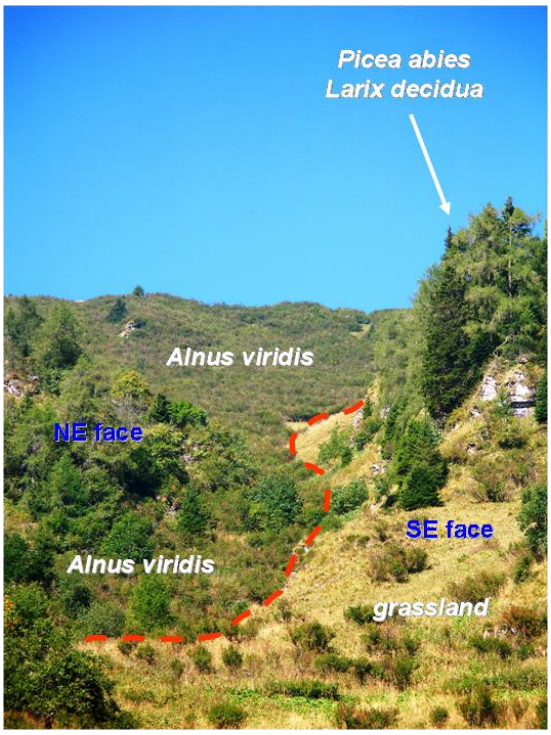

Figure 3.5 - Vegetation patterns overview in relation to different aspects in the Miozza basin (Tarolli, 2007).

3.2 Headwater catchment A

Figure 3.6 - Upward view of the headwater catchment A of the Miozza basin (Tarolli, 2007).

The study area A (*Figure 3.6*) presents a surface of about 0.87 km^2 and is located at an elevation ranging from 1368 m a.s.l. to 2123 m a.s.l., with a mean elevation value of about 1754m a.s.l.. Its mean slope value is about 31.58°, while the maximum slope value is 70.15°. The hillshade representation of the basin is exhibited in *Figure 3.7*.

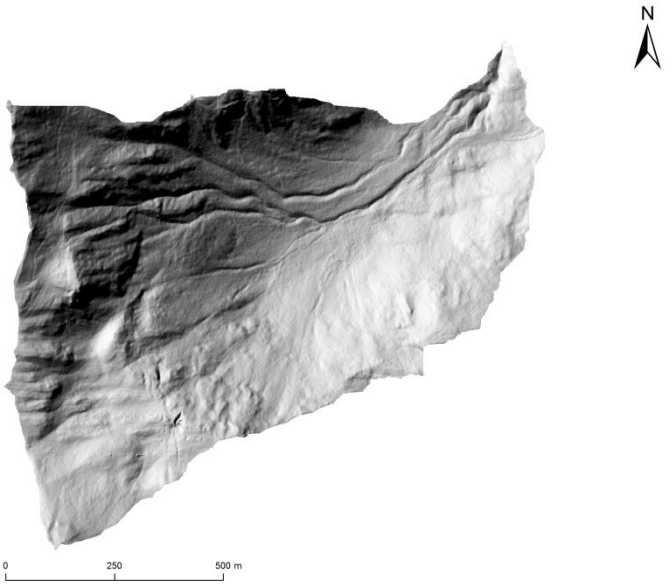

Figure 3.7 - Shaded relief map obtained from DTM at 1 m resolution of the sub-basin A of the Miozza chatchment.

The basin was glaciated during the last ice age (Würm ice age) until glaciers started to retreat during the Pleistocene-Holocene transition (12,000 to 11,500 years ago). The upper part of the basin consists of a low-slope belt, separated from the middle-lower part by a morphological threshold, which characterizes the typical hanging valley of a glacial cirque. The middle-lower part of the basin is characterized by cobles and gravels merged with a silty matrix, consisting in the 63 % of the basin area. These can be recognized as colluvial deposits related to the paleo-landsliding phenomena occurred during the Lower Holocene. Additionally, 10 % of the basin surface is characterized by a silt matrix with cobles of the Upper Pleistocene, while the remaining area consists of sandstones, shales, calcarenites and marly limestones belonging to the Werfen formation (Scythian). The soil is relatively shallow (~ 0.2 m) on steeper slopes and deeper (up to 1 m) in other places. The 98 % of the basin area is covered by vegetation, of which the 25 % are grasslands of high altitude pastures, the 55 % consists of shrubland mainly characterized by Green Alder (*Alnus viridis* (Chaix) DC.), the 14 % are medium height forest stands characterized by European Mountain-Ash (*Sorbus aucuparia* L.). Finally, the 5 % are made of the coniferous high forest stands, where mainly vegetate Norway Spruce (*Picea abies* (L.) Karst.) and European Larch (*Larix decidua* Mill.). The remaining

2 % of the basin area consists in unvegetated rocky outcrops. It is worth saying that the vegetation classification used to analyze these study areas precisely reflects the species characterization of the two basins, as it is shown by *Figure 3.8*.

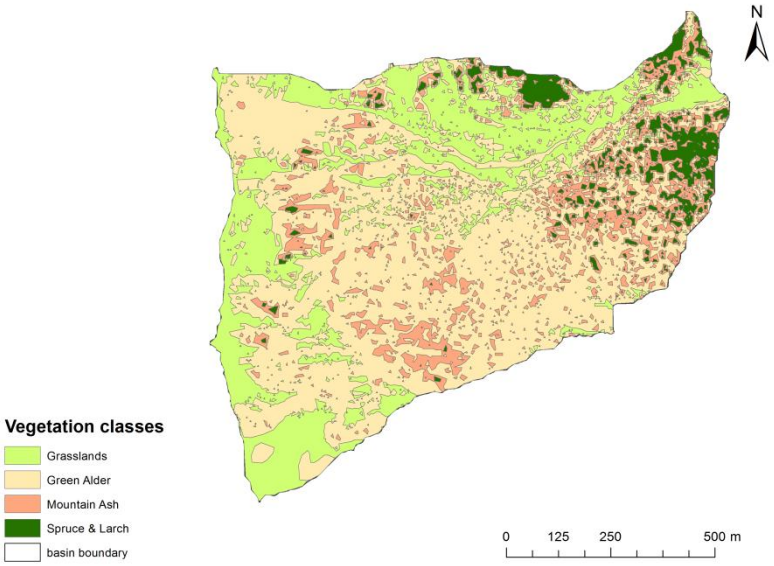

Figure 3.8 - Vegetation classes for the sub-basin A of the Miozza chatchment.

3.3 Headwater catchment B

Figure 3.9 - Upward view of the headwater catchment B of the Miozza badin (Tarolli, 2007).

The study area B (*Figure 3.9*) is characterized by a surface of about 1.13 km^2 and presents an elevation ranging from a minimum value of 1185m a.s.l. to a maximum one of 2056 m a.s.l.,

with a mean elevation of about 1673 m a.s.l.. The mean slope value is 39.04° and the maximum slope value is 74.09°. The hillshade representation of this headwater catchment is presented in *Figure 3.10*.

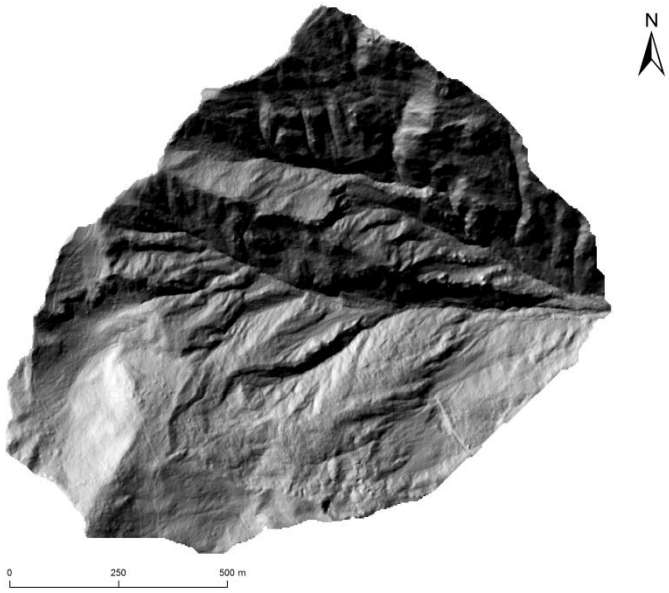

Figure 3.10 - Shaded relief map obtained from DTM at 1 m resolution of the sub-basin B of the Miozza chatchment.

The lithology of the basin consists for a 70 % of sandstones, shales, calcarenites and marly limestones which belong to the Werfen formation (Scythian); while the remaining 30 % is made of cobles and gravels merged with silt matrix, this consists in colluvial deposits of the Holocene limited to some areas at the outlet of the basin. As in the case of basin A, the soil thickness is about 0.2 m on steeper areas and it rises up to 1.5 m in topographic hollows. The vegetation cover interests the 75 % of the area. According to this percentage, the 23 % corresponds to the grassland areas and the 32 % are Green Alder (*Alnus viridis* (Chaix) DC.) shrublands. The medium height forest covers the 10 % of the forested area and mainly consists of European Mountain-ash (*Sorbus aucuparia* L.). Finally, the high forest stands interest another 10 % of the surface and are composed by a prevalence of coniferous species such Norway Spruce (*Picea abies* (L.) Karst.*)* and European Larch (*Larix decidua* Mill.), but also the European Beech (*Fagus sylvatica* L.) is present in some areas. The vegetation classification of the study area is presented in *Figure 3.11*.

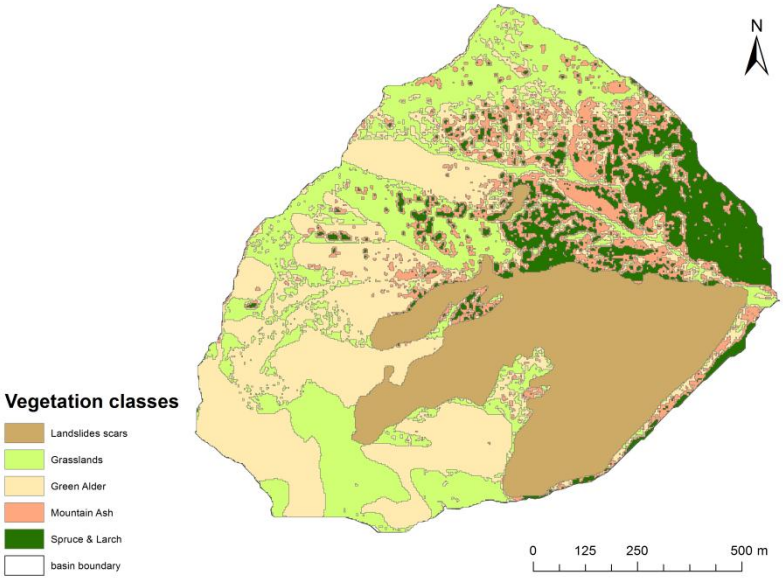

Figure 3.11 - Vegetation classes for the sub-basin B of the Miozza chatchment.

The 25 % of the basin area consists of unvegetated landslide scars, presenting an average slope of 39°. Such landslides occur in complexes that result from the aggregation of many shallow landslides.

3.4 Cetus basin: general characteristics

Figure 3.12 - Downward view of the Cetus basin also showing the Cetara village at the valley bottom (www.summitpost.org - 2010).

Another analyzed study site is the catchment area of the Cetus stream (*Figure 3.12*), which is located along the Tyrrhenian coast, under the municipality of Cetara that is included in the Salerno province (Campania region) (*Figure 3.13*).

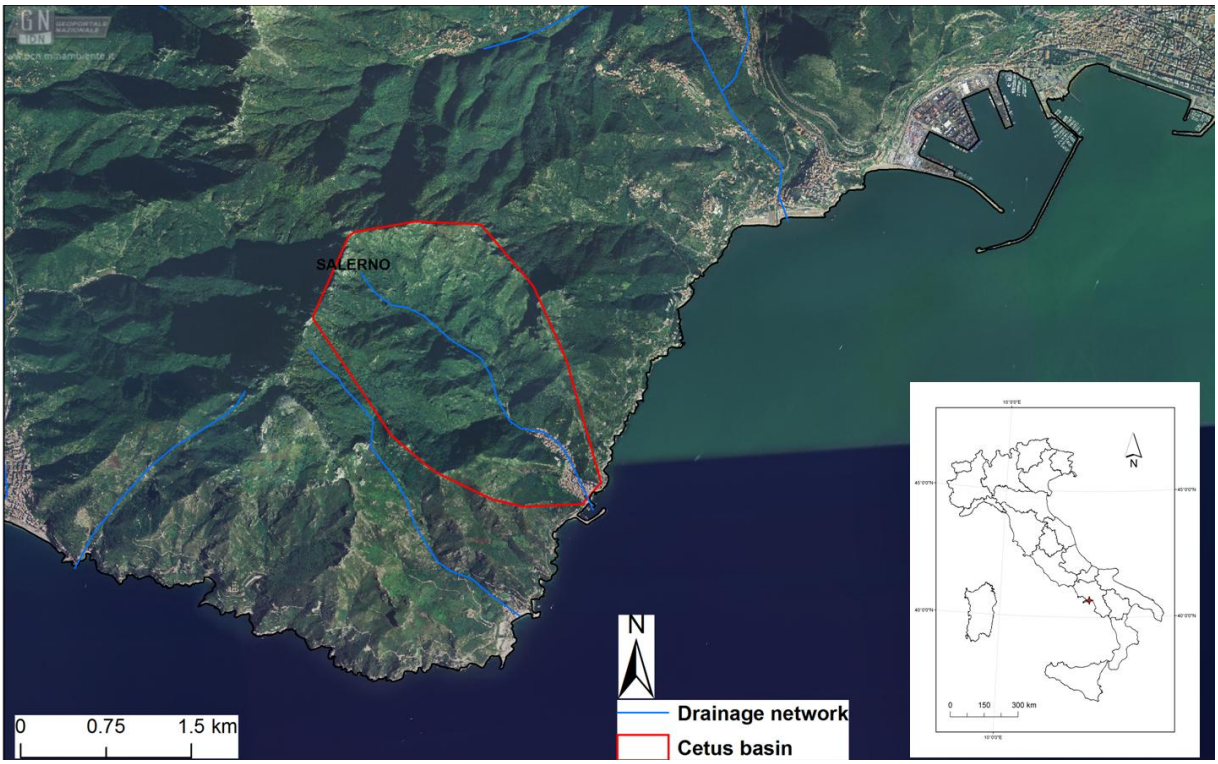

Figure 3.13 - Overview of the Cetus catchment.

The municipality of Cetara falls under the regional basin authority "in Destra Sele". It comprehends the whole catchment area of the "Vallone Grande" that is delimited to the North from the ridges of "Monti del Demanio" (932 m a.s.l.), "Monte della Rena" (551 m a.s.l.), "Monte del Lavoratore" (618 m a.s.l.) and "Monte Falerio" (684 m a.s.l.) which gently slopes toward the South-West direction until the basin joins the Tyrrhenian sea. Right in the narrow gorge of the coastal alluvial fan of the "Vallone Grande" the Cetara village is located, which is distributed along the Cetus stream line for about 1 km inward. *Table 3.2* summarizes the main morphometric characteristics of the basin.

Table 3.2 - General morphometric characteristics of the Cetus basin

Area	3.59 km^2
Minimum elevation	25.00 m a.s.l.
Average elevation	425.74 m a.s.l.
Maximum elevaiton	934 a.s.l.
Minimum slope	0.00 °
Average slope	37.54 °
Maximum slope	80.59 °

The study area is placed within the Monti Lattari regional Park and it is involved in two Sites of Community Importance (SIC IT8030008 Dorsale dei Monti Lattari; SIC IT8050054 Costiera Amalfitana tra Maiori e il torrente Bonea), as well as in the Special Protection Area (ZPS IT8050009 Costiera Amalfitana tra Maiori e il torrente Bonea). In *Figure 3.14* the distribution of SIC and ZPS protected areas and Unesco sites over the Campania region is shown.

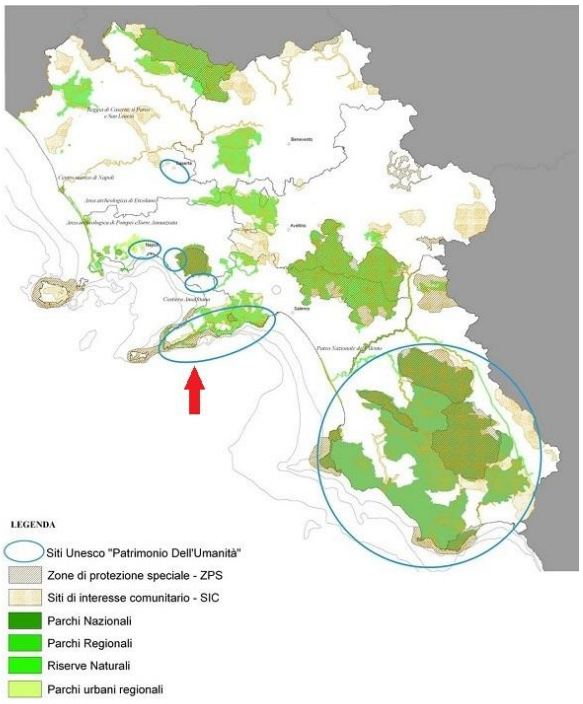

Figure 3.14 - Protected areas and "Unesco" sites of the Campania region. The red arrow points to the study area. (modified from "Piano Territoriale Regionale 2006 - Bollettino ufficiale della regione Campania, Gennaio 2007").

According to the soil use description reported in the PSAI (Piano Stralcio d'Assetto Idrogeologico - 2009) the main part of the basin area (73 %) is covered by shrubs and grassland vegetation; a wide portion is also occupied by heterogeneous agricultural areas (20 %), while only the 2 % is classified as urban areas and the remaining 5 % is covered by bare or sparsely vegetated areas (*Figure 3.15*).

Besides the low amount of wood harvesting recorded (about 5% of the national timber production - ISTAT 2007), the human pressure is highly exerted on the Campania region because of the high urbanization of the coastal areas and the intensive agricultural activity. Moreover, an increasing trend has been recorded for the touristic sector, which is probably linked to the establishment of the protected areas and the development of recreational activities.

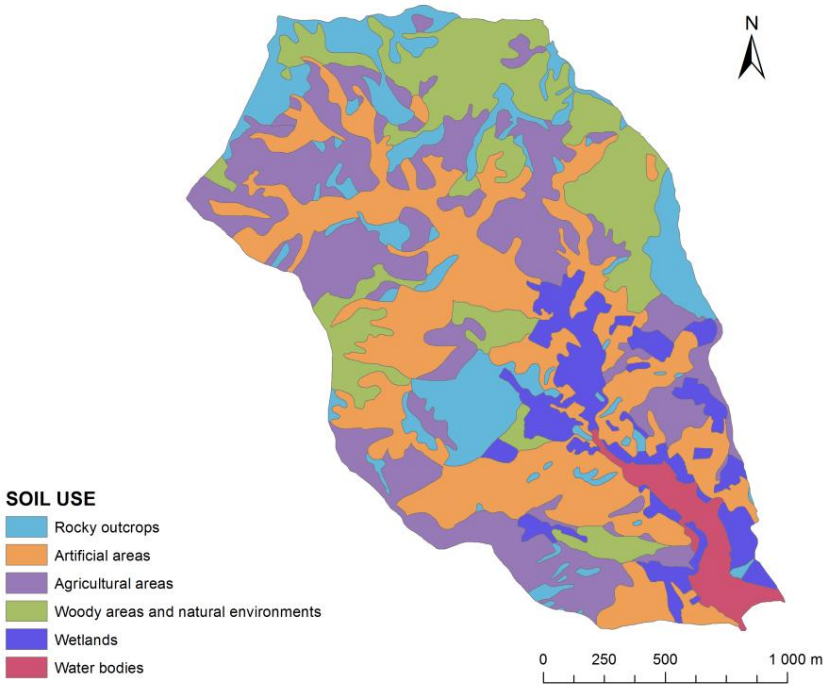

Figure 3.15 - Soil use description for the Cetus basin (Agenzia Nazionale per la Protezione dell'Ambiente e per i Servizi Tecnici - APAT, 2001).

3.4.1 Geological characteristics

The emerging surfaces belong to the dolomitic limestone Mesozoic series of the Carbonate Platform/Basin System (CPBS sensu D'Argenio et al., 1993).

In particular, in the area are present the medium-high section of this series (Jurassic), which basically presents calcareous origins, and the low section (Triassic), which has a dolomitic nature.

Most recent surfaces are made by alluvial and detrital continental deposits from the Pleistocene and Holocene series, besides loose deposits of the detrital-pyroclastic coverage. The subsequent formations are present in the municipal area:

- Dolomitic formation (Upper Triassic - Lower Jurassic): laminated bioclastic dolomites Member;
- Palaeodasycladus limestomes (Lower Jurassic): stratified micritic limestones with bioclasts;
- "Supersintema" of Conca (Upper Pleistocene): sandy-limestone conglomerates and phytoclastic travertines mainly located in the alluvial fan area;
- "Sintema" of Masseria Acqua Santa (Upper Pleistocene - Holocene): fluvial gravels and sands interbedded with limno-marsh, fluvial and volcaniclastic pelites;

- recent fluvial sediments (Upper Holocene): gravel or silty sands, from loose to dense, localized to the valley bottom;
- seaside sediments (Upper Holocene): loose sands with intermediate to coarse texture, locally gravelly, characterize the coastal area;
- artificial deposits (current): debris material and landfills due to reclamation activities.

3.4.2 Geomorphology of the basin

The geomorphology of the municipal area is composed by two main units: the Vallone Grande catchment area and the South-Eastern hillslope of the Monte Falerio. The study area is localized in the first unit, which is positioned on a fault line in the North-West/South-East direction and is characterized by a rugged surface morphology with many hollows and steep slopes. Moreover, the coast line consists in a cliff of the Upper Pleistocene.
The drainage network is deeply influenced by the underlying morphology which follows the tectonic fault lines, where the dolomitic limestones result to be more erodible. Secondary basins join the main stream branch, especially on its orographic right side. The Cetus stream presents a torrential flow regime which in occurrence of extreme rainfall events could become a serious threat to the highly exposed village present at the outlet of the drainage basin, as already happened in 1910 and 1954 when catastrophic flood events took place in this area. The main causes of such calamities were linked to the high steepness of the slopes and to the widespread presence of pyroclastic-detritic coverage. In addition, the frequency and typology of the landslides detected by the municipal landslides inventory (IFFI project, "Rapporto sulle frane in Italia", APAT 78/2007), reveal that these erosion phenomena are strongly influenced by the structural arrangement of the outcropping surfaces. Indeed, rocky outcrops are typically subject to rock falls, while debris and mud flows mainly characterize morphologic hollows with significant pyroclastic-detritic coverage.

3.4.3 Climatic conditions

The Campania region is characterized by a high variability of climatic conditions, due to its complex morphology. Indeed, the inner areas of the region present high elevation ridges with very cold and humid winters, whereas the coastal areas are subject to the mitigation effect of the sea and to the protection offered by the Apennine mountain chain. Although this, such

closeness of the mountain region to the Tyrrhenian see promotes the abundance of precipitations. In particular, for the coastal plains and valleys, mean annual rainfall values increase in the southward direction within the range of 900-1200 mm, while in the inner mountainous part of the region the annual rainfall amount increases up to 1500-2000 mm. Precipitation distributes irregularly over the year, showing a maximum in the fall-winter season and a minimum in summer, which is less evident in the inner part of the region due to higher elevations. Snowfall precipitations are abundant on the Apennine but very rare on the coast. Temperatures are mild on the coastal areas for the whole year. Mean annual temperature in this areas is about 16°-17°C, with minimum values lightly below 0°C and maximum values of about 38°C. A strong temperature range characterizes the inner part of the region with extreme values between 2°C and 40°C; mean annual values are in the range of 8°-15°C.

3.4.4 Vegetation characterization of the study area

To better understand the vegetation characterization of the Cetus basin, it has been worth consulting the Piano Forestale Generale 2009-2013 for the Campania region, which refers to the "Inventario Nazionale delle Foreste e dei Serbatoi Forestali" (2005). According to this document, the forest surface of the region is divided in two major categories: woods and wooded lands; each one of this is subdivided in other inventorial categories. The former, which comprehends high forests, timber arboriculture lands and temporary non-forested areas, occupies the 28% of the regional area of which the 69% is located at elevations lower than 1000 m a.s.l. (that corresponds to the elevation range of the Cetus study area). The latter major category, which comprehends low forests, spars cover forests, bushes, shrubland and other wooded unclassified areas, occupies the 4.5% of the regional surface, of which about the 8% is located below the 1000 m a.s.l.. It is also interesting to note that main aspect directions which characterize the wood category are the North/North-East aspects, while for the wooded lands category the main aspect directions are South-East/South-West. This is consistent with the results obtained for the aspect parameter characterization of the Cetus study area.

According to the paper of the monitoring of the biodiversity heritage of the Monti Lattari Regional park (Monitoraggio del patrimonio di biodiversità - Analisi per la gestione delle risorse ambientali per la conservazione della biodiversità, 2008), the Cetara municipality falls

under the extreme conservation area of the Capo d'Orso sector. The plant communities of interest present in the area are:

- arborescens garrigue with *Juniperus* spp.;
- Quercus ilex woods related to the "*Foreste di Quercus ilex* e *Quercus rotundifolia*" habitat;
- shrubland with a dominance of *Euphorbia dendroides* (L.) and *Chamaerops humilis* (L.) related to the "Arbusteti termo-mediterranei e pre-steppici" habitat;
- nucleus of steppe grasslands with *Ampelodesmus mauritanicus* (Th. Dur. & Schinz.) and *Hyparrhenia hirta* (L.) related to the "Percorsi substeppici di graminacee e piante annue dei *Thero-Brachypodietea*" habitat;
- cliff with Mediterranean vegetation with local *Limonium* (Mill.) spp.

Other floristic species of interest are:

- *Chamaerops humilis* (L.)
- *Seseli polyphyllum* (Ten.)
- *Centaurea tenorei* (Guss.)
- *Limonium remotispiculum* (Mill.)

To go deeply in detail on the study area vegetation characterization, the phisiognomic map of vegetation (Copertura forestale e stabilità dei versanti nel bacino di Cetara (SA), in previsione e prevenzione del rischio idrogeologico. Bacino Campione di Cetara (SA), Agenzia Nazionale per la Protezione dell'Ambiente - APAT 2001) has been analyzed. This map presented 60 vegetation classes (*Figure 3.16*).

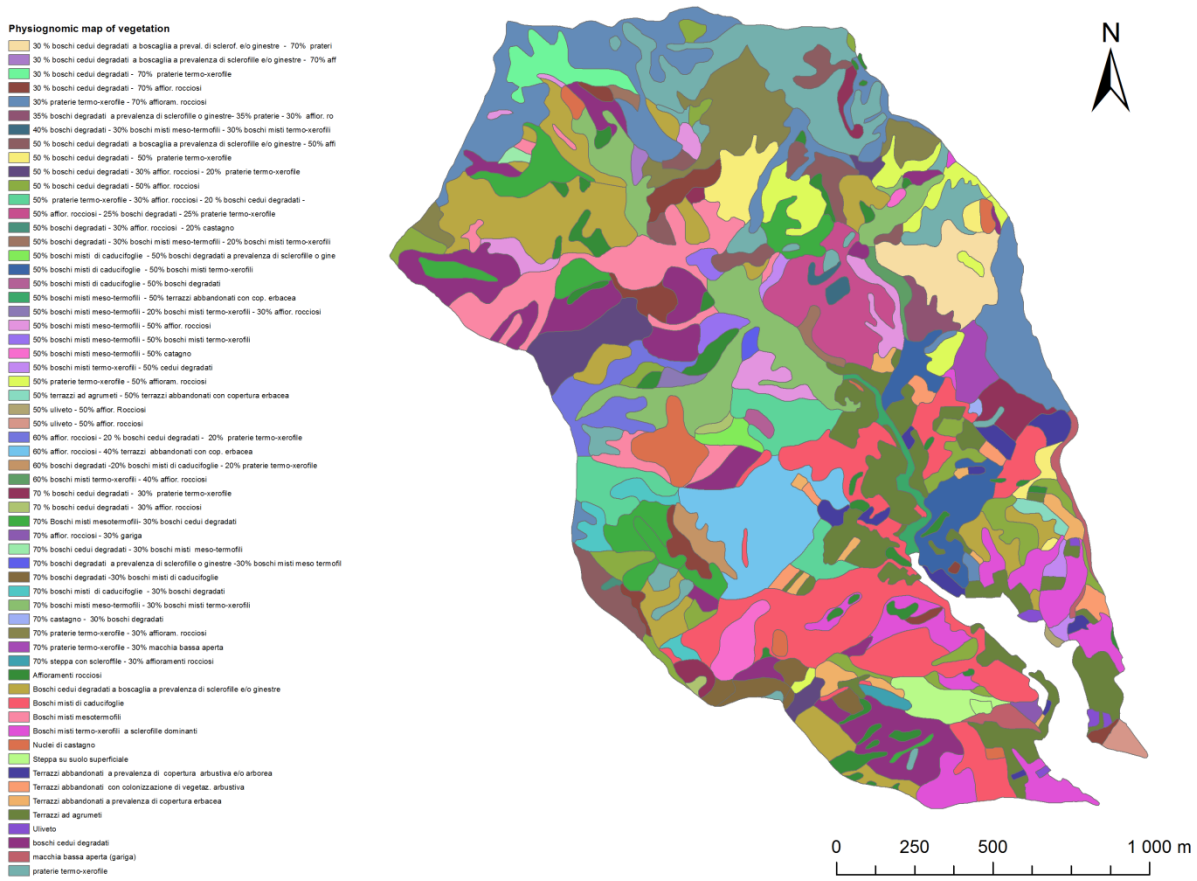

Figure 3.16 - Representation of the 60 original vegetation classes from the physiognomic map of vegetation (Agenzia Nazionale per la Protezione dell'Ambiente e per i Servizi Tecnici - APAT, 2001).

With the aim to overcome the inconvenient issue of operating with such a high number of classes, they were merged together on the base of their common features, mainly promoting the differentiation derived by the vegetation habit (e.g. woody vegetation, shrubs, grasses) and the thermophile preferences of each vegetation community. In this way it became possible to relate the morphological analysis carried out to each typology of vegetation in order to highlight the differences in their distribution over the landscape. From this aggregation six different vegetation classes emerged (*Figure 3.17*):

- Rocky outcrops with woody vegetation
- Rocky outcrops with grassland vegetation
- Mesothermophilous woods
- Thermoxerophilous woods
- Thermoxerophilous grasslands
- Garrigue.

Each vegetation category reported in *Figure 3.16* was assigned to one of the six classes also considering its position in the basin area through the visualization of the aerial image (Web Map Service "Ortofoto colore 2006" from the Geoportale Nazionale website) and its closeness to other categories belonging to a specific class. Furthermore, it has been also verified the correspondence of the vegetation classes to the soil use map of the area according to the map represented in *Figure 3.15*. Proceeding with such methodology, some of the 60 categories had to be excluded because of their incompatibility with any of the classes, in order to avoid the production of non-comparable heterogeneous results. The resulting map of vegetation classes is shown in *Figure 3.17*.

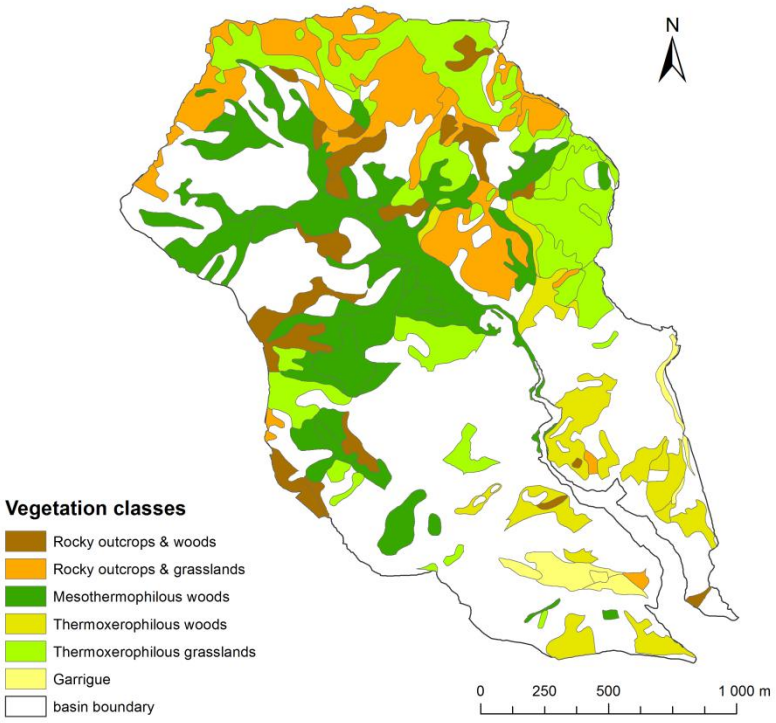

Figure 3.17 - Physionomic map of vegetation for the Cetus basin reduced to six classes, as a result of the aggregation of the original classes from the physiognomic map of vegetation (Agenzia Nazionale per la Protezione dell'Ambiente e per i Servizi Tecnici - APAT, 2001).

According to the criteria used to define forest typologies based on several stands located in the Southern Apennines by Pignatti et al. (2004), the forest types that have been supposed to better describe the above presented classes are here reported with their species description. In addition, some groups of species from the same criteria definition are reported to describe the shrubby and grasslands classes.

Holm Oak mesoxerophilous forest type

Quercus ilex, Quercus pubescens, Fraxinus ornus, Ostrya carpinifolia, Carpinus orientalis, Cercis siliquastrum, Acer monspessulanum, Phillyrea latifolia, Smilax aspera, Crataegus monogyna, Pistacia lentiscus, Clematis vitalba, Pistacia terebinthus, Arbutus unedo, Clematis flammula, Coronilla emerus, Myrtus communis, Lonicera implexa, Styrax officinalis, Viburnum tinus, Rubia peregrina, Asplenium onopteris, Arisarum vulgare, Brachypodium sylvaticum, Daucus carota, Cymbopogon hirtus, Lagurus ovatus, Agrostis stolonifera, Geranium purpureum, Geranium robertianum, Oryzopsis miliacea, Prasium majus, Urginea maritima, Viola suavis.

Downy Oak mesoxerophilous forest type

Quercus pubescens, Fraxinus ornus, Ostrya carpinifolia, Quercus ilex, Quercus cerris, Acer campestre, Acer obtusatum, Cytisus sessilifolius, Crataegus monogyna, Rosa canina, Juniperus oxycedrus, Coronilla emerus, Lonicera caprifolium, Rubus ulmifolius, Cornus sanguinea, Cornus mas, Juniperus communis, Smilax aspera, Brachypodium rupestre, Teucrium chamaedrys, Asplenium onopteris, Lotus corniculatus, Cruciata glabra, Luzula forsteri, Brachypodium sylvaticum, Rubia peregrina, Sanguisorba minor, Briza maxima, Cerastium arvense, Clinopodium vulgare.

Hop Hornbeam mesoxerophilous forest type

Ostrya carpinifolia, Fraxinus ornus, Carpinus orientalis, Quercus pubescens, Acer obtusatum, Quercus ilex, Acer monspessulanum, Quercus cerris, Acer campestre, Fagus sylvatica, Sorbus domestica, Castanea sativa, Cornus mas, Cytisus sessilifolius, Coronilla emerus, Laburnum anagyroides, Crataegus monogyna, Daphne laureola, Cornus sanguinea, Corylus avellana, Rosa canina, Rubus ulmifolius, Clematis vitalba, Euphorbia amygdaloides, Euonymus europaeus, Juniperus communis, Smilax aspera, Phillyrea latifolia, Melica uniflora, Melittis melissophyllum, Brachypodium rupestre, Viola reichenbachiana, Lathyrus venetus, Rubia peregrina, Anemone apennina, Helleborus foetidus, Brachypodium sylvaticum, Campanula trachelium, Cruciata glabra, Festuca heterophylla, Fragaria vesca, Clinopodium vulgare, Scutellaria columnae, Aremonia agrimonoides, Hepatica nobilis.

Holm Oak mesophilous forest type

Quercus ilex, Fraxinus ornus, Ostrya carpinifolia, Acer obtusatum, Carpinus orientalis, Acer monspessulanum, Quercus pubescens, Acer campestre, Smilax aspera, Crataegus monogyna, Phillyrea latifolia, Coronilla emerus, Cornus mas, Viburnum tinus, Ligustrum vulgare, Rubus ulmifolius, Laburnum anagyroides, Arbutus unedo, Clematis vitalba, Euphorbia amygdaloides, Juniperus communis, Pistacia terebinthus, Styrax officinalis, Rubia peregrina, Melica uniflora, Asplenium onopteris, Melittis melissophyllum, Anemone apennina, Brachypodium sylvaticum, Lathyrus venetus, Lathyrus vernus, Aremonia agrimonoides, Arisarum vulgare, Brachypodium rupestre, Fragaria vesca, Helleborus foetidus, Teucrium chamaedrys.

Downy Oak mesophilous forest type

Quercus pubescens, Quercus cerris, Fraxinus ornus, Acer obtusatum, Ostrya carpinifolia, Acer campestre, Quercus frainetto, Crataegus monogyna, Cytisus sessilifolius, Cornus mas, Clematis vitalba, Corylus avellana, Coronilla emerus, Laburnum anagyroides, Euonymus europaeus, Lonicera caprifolium, Rosa arvensis, Rubus ulmifolius, Cornus sanguinea, Ligustrum vulgare, Viola reichenbachiana, Brachypodium rupestre, Brachypodium sylvaticum, Melittis melissophyllum, Clinopodium vulgare, Hepatica nobilis, Anemone apennina, Campanula trachelium, Cruciata glabra, Fragaria vesca, Lathyrus venetus, Festuca heterophylla, Helleborus foetidus, Scutellaria columnae, Teucrium chamaedrys.

European Hornbeam mesophilous forest type

Ostrya carpinifolia, Fraxinus ornus, Carpinus betulus, Acer obtusatum, Quercus cerris, Acer campestre, Quercus pubescens, Fagus sylvatica, Sorbus domestica, Castanea sativa, Cytisus sessilifolius, Crataegus monogyna, Laburnum anagyroides, Corylus avellana, Cornus mas, Clematis vitalba, Rosa arvensis, Daphne laureola, Euonymus europaeus, Euphorbia amygdaloides, Coronilla emerus, Rosa canina, Lonicera caprifolium, Cornus sanguinea, Lathyrus venetus, Melittis melissophyllum, Campanula trachelium, Anemone apennina, Helleborus foetidus, Fragaria vesca, Viola reichenbachiana, Melica uniflora, Festuca heterophylla, Brachypodium sylvaticum, Hepatica nobilis, Cruciata glabra, Luzula forsteri, Primula vulgaris, Aremonia agrimonoides, Potentilla micrantha, Luzula sylvatica, Brachypodium rupestre.

Grassland species

Agrostis stolonifera, Asphodelus albus, Brachypodium ramosum, Brachypodium rupestre, Briza maxima, Cerastium arvense, Cymbopogon hirtus, Daucus carota, Galium album, Galium lucidum, Geranium lucidum, Geranium purpureum, Helianthemum apenninum, Lagurus ovatus, Lotus corniculatus, Micromeria graeca, Oryzopsis miliacea, Sanguisorba minor, Satureja montana, Sesleria nitida, Silene vulgaris, Tordylium apulum, Urginea maritima, Viola suavis.

Shrubs and shrubby edges species

Anthriscus nemorosa, Bryonia dioica, Campanula persicifolia, Chaerophyllum temulum, Chamaecytisus hirsutus, Coronilla varia, Digitalis lutea, Fragaria vesca, Galium aparine, Genista tinctoria, Juniperus communis, Origanum vulgare, Peucedanum oreoselinum, Rubus hirtus, Rubus idaeus, Rubus ulmifolius, Symphytum officinale, Trifolium medium.

Thermophilous evergreen woods, brush and garrigue species

Anagyris foetida, Arbutus unedo, Arisarum vulgare, Asplenium onopteris, Calicotome spinosa, Cistus incanus, Cistus monspeliensis, Clematis flammula, Clinopodium vulgare, Daphne gnidium, Juniperus oxycedrus, Lonicera implexa, Luzula forsteri, Myrtus communis, Osyris alba, Phillyrea angustifolia, Phillyrea latifolia, Pistacia lentiscus, Pistacia terebinthus, Prasium majus, Quercus ilex, Rhamnus alaternus, Rubia peregrina, Smilax aspera, Spartium junceum, Teucrium flavum, Teucrium polium, Viburnum tinus.

Deciduous termophilous woods whit a mesoxerophic characterization

Acer monspessulanum, Acer obtusatum, Alnus cordata, Anemone apennina, Arum italicum, Cardamine graeca, Centaurea centaurium, Cercis siliquastrum, Cornus mas, Coronilla emerus, Crepis leontodontoides, Cruciata glabra, Cytisus sessilifolius, Dorycnium pentaphyllum, Euonymus latifolius, Fraxinus ornus, Helleborus foetidus, Huetia cynapioides, Hypericum perfoliatum, Inula conyza, Knautia purpurea, Laburnum anagyroides, Lathyrus venetus, Melica uniflora, Melittis melissophyllum, Oenanthe pimpinelloides, Ostrya carpinifolia, Potentilla micrantha, Prunus mahaleb, Quercus cerris, Quercus frainetto, Quercus pubescens, Scutellaria columnae, Silene sicula, Sorbus aria, Sorbus domestica, Styrax officinalis, Tanacetum corymbosum, Teucrium chamaedrys, Vinca major.

3.5 Analysis of surface morphology

This study has been developed in two different study areas: the Cetus basin, located along the Italian southern West coast, and the Miozza basin, in the Carnia north-eastern Alpine region. They have been specifically chosen in order to show how morphometric analysis are affected by consistent different climatic conditions, geology, soil and vegetation compositions.
Bearing in mind the aim of this work, that is to investigate the vegetation distribution attitudes in relation to the analyzed morphometric parameters over different environments, it is quite relevant to note that for both the study areas high resolution topographic data were available. This allows to proceed with specific analysis in order to achieve the prefixed goal in a way that, otherwise concerning with a lower level of resolution, could certainly not be developed.
The general procedure here proposed for both the study areas consists in generating morphometric data, relative to the parameters previously described, in the form of raster grid files and successively sort them accordingly to each one of the vegetation classes determined beforehand, on the basis of environmental peculiarities that define each of the basins.
The obtained data were finally examined through statistical analysis, such as distribution indexes, box plots and log-log plots of the S-A and C-A relations, implemented by the MATLAB numerical computing environment.
By way of introduction, it can be said that the final purpose and the analysis comparison to test the hypothesis of an existing relation between vegetation distribution and morphometric properties of the basins were the same for both the study areas. Therefore, it has been considered appropriate to modify the initial methodology accordingly to the different topographic data available for each basin. For this reason, here are reported two distinct paragraphs to describe the procedures carried out for the Cetus and the Miozza catchments.

3.5.1 Cetus basin

The analyses have been carried out starting from a TIN (Triangular Irregular Network) representation of the catchment surface (*Figure 3.18*) derived by conventional cartography, whose principal parameters are reported below:

- **Triangulation Method:** *delaunay conforming*
- **Number of Data Nodes:** *184873*
- **Number of Data Triangles:** *369710*
- **Z Range:** *(25.000000; 935.000000)*

The TIN digital surface model comes from the Agenzia Nazionale per la Protezione dell'Ambiente (APAT, 2001) which has now become the Istituto Superiore per la Protezione e la Ricerca Ambientale, Roma, (ISPRA, 2006). Besides that, the contour lines at 5 m and 25 m associated to the elevation range of the basin have been also provided.

In order to identify different vegetation classes, a physiognomic map of vegetation (*Figure 3.17*) of the study area has been used. The numerous kinds of environmental, moisture and soil use conditions that can be found in the basin resulted in sixty different vegetation descriptions provided by the map, each one of these showing the prevalence (in term of percentages) of one up to three co-existing environments. It follows that, to proceed with the analysis over each one of the sixty vegetation types and compare them to one another would have led to inconsistent results and conclusions devoid of any meaning. To overcome this problem, vegetation types were merged together toward obtaining only six new classes; this step was carried out, on the basis of the available descriptions, following some selection criteria here described. The most determinant element considered was the main percentage of vegetation type presented by each description, but also the more or less pronounced adaptability to xeric environments. Also, the soil use map (*Figure 3.15*) was looked at as an indicator for human influence over the basin. To this regard, it is important to note that most of the soils classified as "*agricultural managed lands*" presented rather a vegetation description that deals with land abandonment: e.g. degraded woodland, degraded copse, some of the termo-xerophic grassland and shrubs. For this reason these lands have been analyzed unlike the terraced areas that are instead presently cultivated, which were excluded because of their inconsistence with natural environments. Moreover, in order to have a visual comparison over the described area, an aerial photograph was consulted, in order to directly look at surface analogies or heterogeneities.

3.5.1.1 Procedure of data analysis

Based on the end points of each 5m contour line, a mask has been built in order to remove from the TIN surface portions where data were unavailable. The so-obtained TIN is represented in *Figure 3.18*.

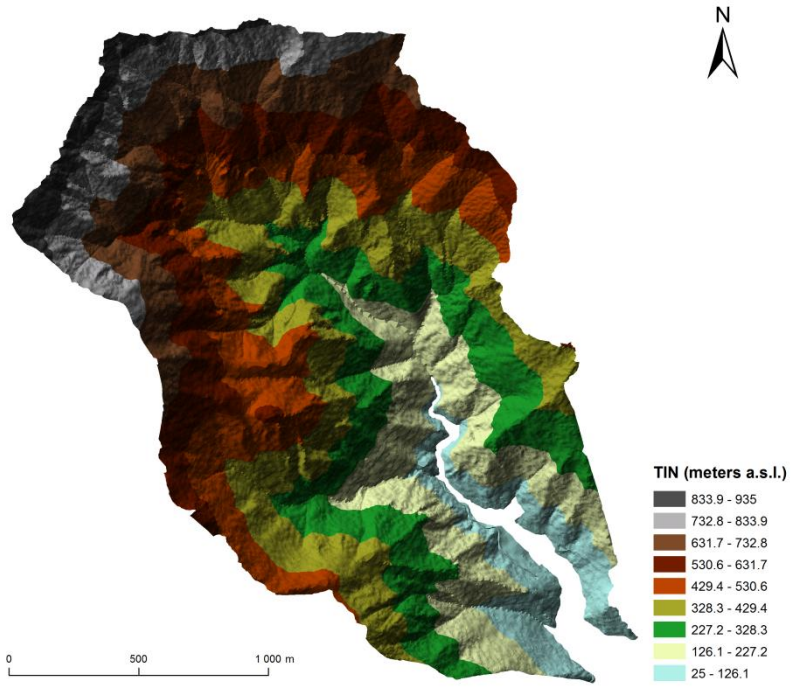

Figure 3.18 - TIN surface representation of the Cetus basin.

With the aim of dealing with as much homogenous as possible data, it was needed to convert the TIN to a raster grid file in order to make comparisons with the other basin examined. This was accomplished by applying the natural neighbor interpolation method with cell sizes either of 5 m and 10 m (*Figure 3.19*). Such grid sizes were selected to reach the highest resolution possible, consistent with the original data.

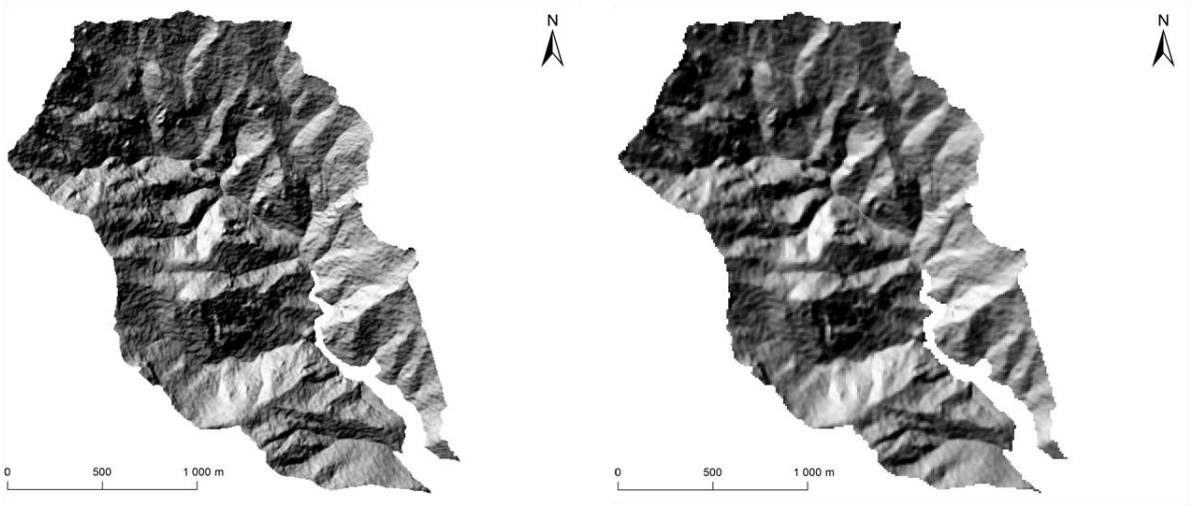

Figure 3.19 – Shaded relief maps of the Cetus basin (5m DTM on the left and 10m DTM on the right).

Then, DTMs needed to be depicted in order to ensure further hydrological analysis. This was achieved with the TauDEM 5.0 software ArcGIS Toolbox (by G. Tarboton, 2005) as already explained in *Paragraph 2.3.3.1.*

The depicted DTMs were successively used to compute the local slope (*Paragraph 2.3.2.2, Figure 3.20*) and the specific catchment area (SCA-*Paragraph 2.3.4*,) for the whole Cetus basin, still using the TauDEM 5.0 Toolbox. Flow directions have been computed according to the D-infinite method which considers the steepest slope among eight triangular facets (Tarboton, 1997); this implies the simultaneous computation of the local slope as the steepest outwards slope on one of the eight triangular facets centered at each grid cell, measured as drop/distance (see *Paragraph 2.3.2.2*)

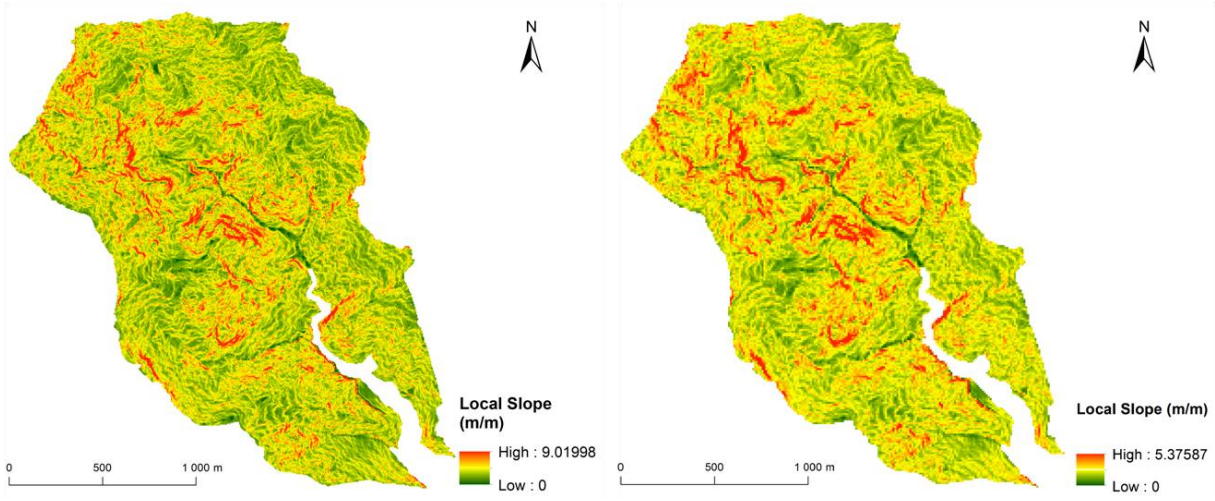

Figure 3.20 - Local Slope maps of the Cetus basin (5m DTM on the left and 10m DTM on the right). The steepest values are shown in red, the lowest values are shown in green. Computations were developed using the TauDEM 5.0 software.

The so-obtained *flow direction* grid files were then used in order to produce the *SCA* grid files. Since the specific catchment area can be described as the upslope drainage area per unit contour length, as confirmed by *Equation 3.10*, the same *SCA* grid files were recalculated simply multiplying their values by the raster cell size (5m or 10m according to the analyzed raster file). The obtained *Upslope Drainage Area* grid files, displayed in *Figure 3.21*, are required to develop the slope-area and curvature-area plots during the stage of statistic computations.

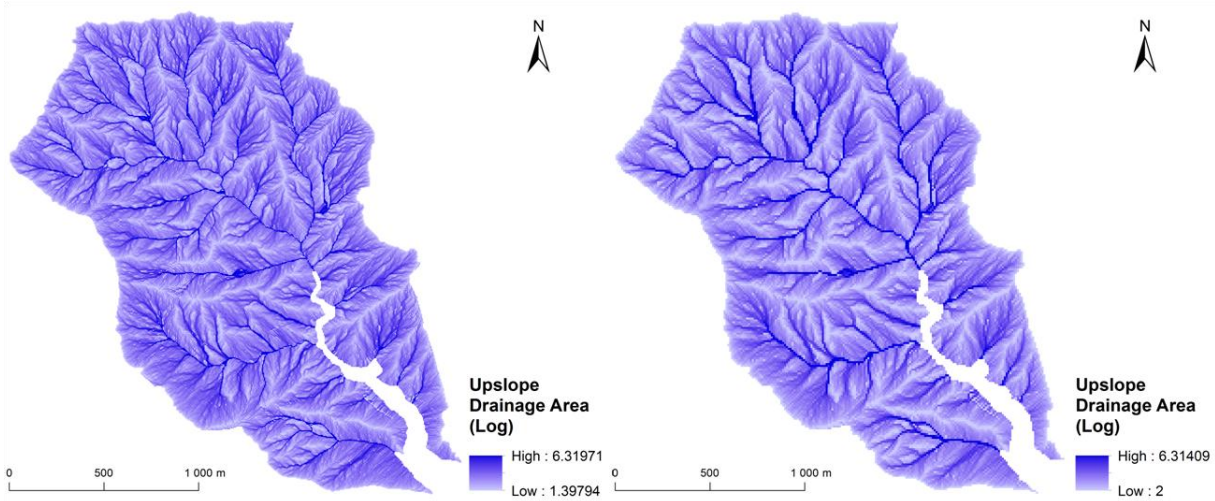

Figure 3.21 - Upslope Drainage Area maps computed with D-infinite algorithm (5m DTM on the left, 10m DTM on the right). Computations were developed using the TauDEM 5.0 software.

Moreover, the *SCA* raster files were processed again as described by *Equation 3.17*, in order to obtain the topographic wetness index (TWI- *Paragraph 2.3.6*) as shown in *Figure 3.22*.

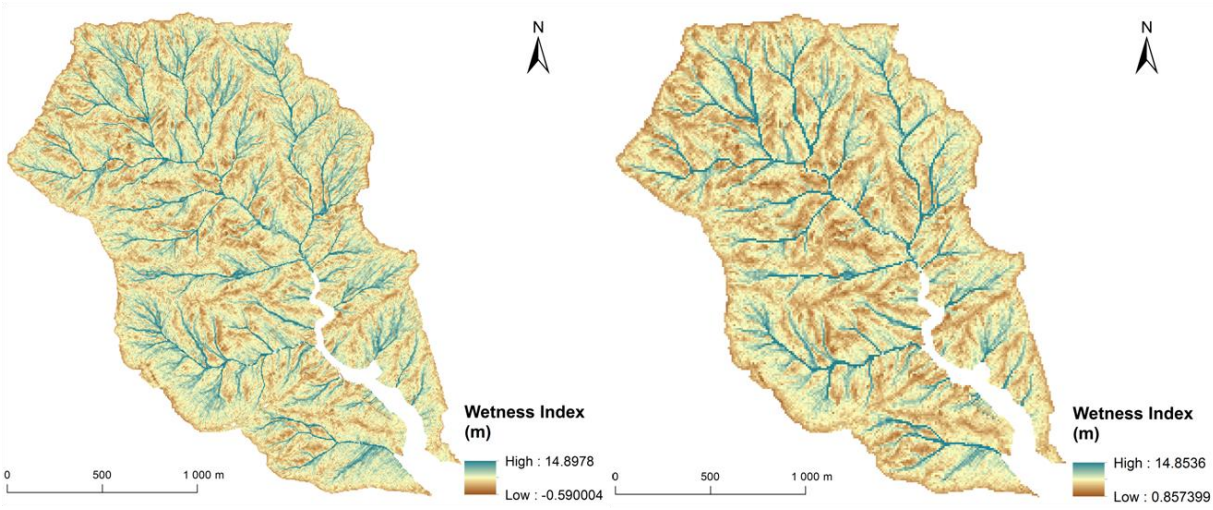

Figure 3.22 - Topographic Wetness Index maps of the Cetus basin (5m DTM on the left and 10m DTM on the right). Higher values of WI correspond to areas saturated more from below.

Successively, the original DTMs were newly adopted to compute the aspect (*Paragraph 2.3.1*) for the basin. The resulting *Aspect* raster files are supposed to give an interpretation of the orientation, along the cardinal directions expressed in degrees of the analyzed surfaces, as laid out in *Figure 3.23*.

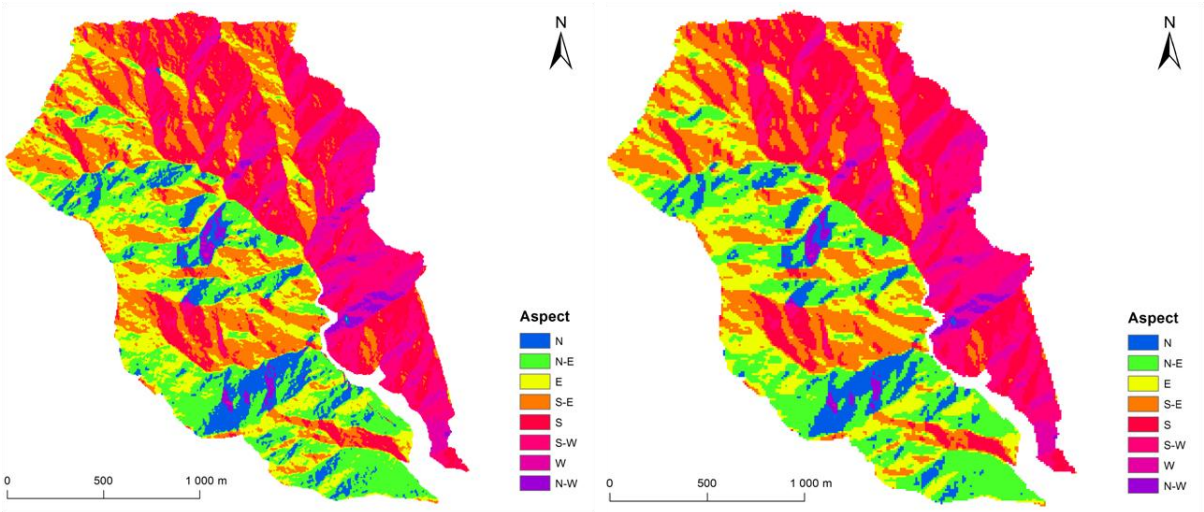

Figure 3.23 - Aspect maps of the Cetus basin (5m DTM on the left and 10m DTM on the right).

Finally, starting from the original DTMs, the *Mean Landform Curvature* (*Paragraph 2.3.5*) has been computed by using the freely available software LandSerf 2.3 (by J. Wood, 2009). It is noteworthy that for curvature analysis were used not depicted DTMs in order to not influence the results with artificial adjustments, as suggested by Tarolli and Dalla Fontana (2009). The basis for most of the analytical functions in LandSerf is the process of quadratic approximation; this involves taking a local moving window of DEM cells (*kernel*) and fitting

the most appropriate continuous quadratic function through them. Then, LandSerf uses this quadratic function to calculate parameters such as curvature. The size of the local window that LandSerf uses has to be set before any calculation. This allows one to perform analysis at broader scales than that implied by the DEM resolution.

Therefore, it has been chosen to be consistent with the results by Pirotti and Tarolli (2010), which have already been explained in *Paragraph 2.3.5*, regarding the selection of a suitable window scale for the curvature analysis. According to this, for the Cetus basin (besides it is not an alpine catchment), a moving window of 3x3 cells has been adopted. This resulted in a 15 m scale for curvature related to the 5 m DTM, which conforms with the optimum scale suggested by the authors. Unfortunately, in the case of the 10 m DTM, the selection of a 3x3 cells window (that also is the finest available in the software) leads to a 30 m scale due to the pixel width; *Figure 3.24* exhibits the differences between the two scales.

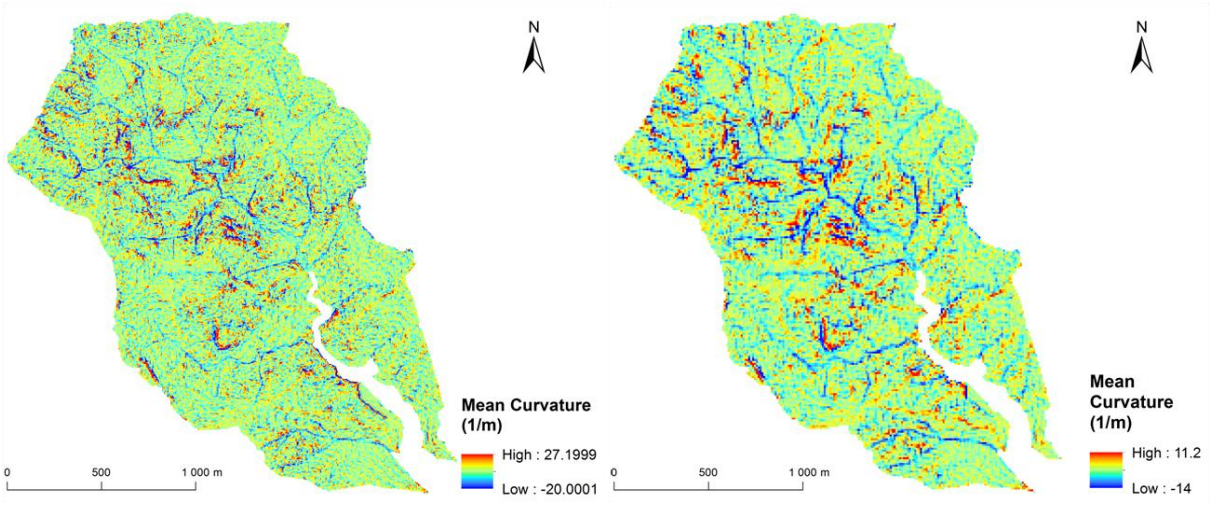

Figure 3.24 - Mean Curvature maps of the Cetus basin obtained from the 5m DTM (on the left) and the 10m DTM (on the right). Raster files of both resolutions were processed with a 3x3 moving window, using the LandSerf 2.3 software.

All the raster files created have been successively extracted on the base of each vegetation class described above. This step allowed the extraction of such morphometric parameters for each vegetation type considered for the Cetus basin, both at 5 m and 10 m resolutions.

3.5.2 Miozza basin

Available topographic data for the Miozza basin were two DTMs respectively of 1m and 3m resolution, which derived by a LiDAR survey in snow-free conditions carried out during November 2003. LiDAR and aerial images were acquired from a helicopter flying at an

average altitude of 1000 m above ground level, using an ALTM 3033 OPTECH and a Rollei H20 Digital camera. The flying speed was 80 kn h^{-1}, the scan angle was 20°, and the scan rate was 33 KHz. The average density of the survey points was greater than 2 points/m^2. The first and last returns corresponding respectively to vegetation and ground, were then filtered, resulting in an irregular density of ground returns with an average of 0.26 points/m^2 (4 m^2/point). The ground point density for areas without continuous vegetation canopy, such as grassland, landslides, and bedrock outcrops, was in average 0.9 points/m^2 (~1 m^2/point). The ground elevation points were already been interpolated using a spline function (see *Paragraph 2.2* dedicated to surface representations). The accuracy of LiDAR dataset used for this study were already been verified in the field by Barilotti et al. (2006), showing an average vertical error of 0.324 m, a mean relative error of 0.02 m and a RMSE of 0.434 m; with the largest error found in areas under dense forest canopies, while the smallest error (<0.1 m) was found in open areas (Tarolli and Dalla Fontana, 2009).

Vegetation distribution over the two analyzed headwater catchments of the Miozza basin was evaluated using the LiDAR-derived DSM at 3 m resolution. In particular, the vertical elevation of different vegetation canopies was analyzed and subsequently, was derived the spatial variation of vegetation species following their heights as surveyed in the field. A double check was also applied through the comparison of the DSM to the available orthophotograph (IT2000) of the area. Based on this procedure four main vegetation classes were individuated on the differences among vegetation heights and also compared with serial photographs and field surveys. These classes and their relative heights ranges are listed below:

- Grassland 0-0.5 m
- Green Alder shrubs land 0.5-4 m
- Mountain Ash medium height forest 4-12 m
- Coniferous tall forest (Spruce & Larch) > 12 m

The same classes are proposed for both the sub basins, since their vegetation composition is quite similar, although the only difference comes from the necessity of considering an additional class to represent the landslides scars located in one of the sub basins. These classes were already showed for each analyzed sub-basin in *Paragraph 3.1.4* by *Figure 3.8* and *Figure 3.11* . It is considerably important to maintain this separate class in order to

analyze the role of early successional vegetation species in re-colonization of disturbed terrain surfaces and their distribution patterns.

3.5.2.1 Procedure of data analysis

Regarding the two analyzed headwater catchments of the Miozza basin, DTMs at 1m and 3m cell sizes were already available; therefore, it has been possible to do the analysis for each sub basin at two different levels of resolution. The procedure was implemented in the same order as for the Cetus basin, although in the case of the Miozza basin the initial DTMs were already given (*Figure 3.25*).

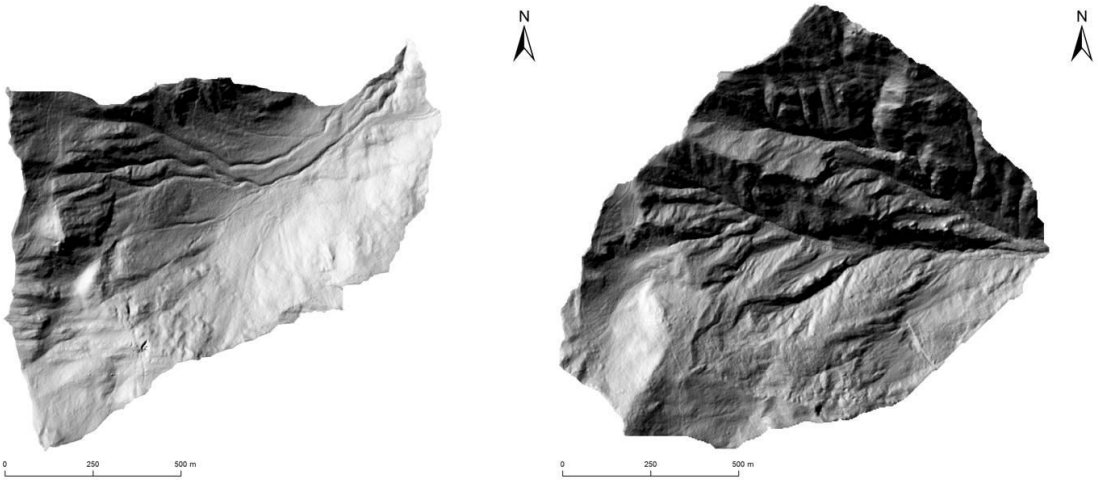

Figure 3.25 – 1m DTMs of the study areas A (left) and B (right) of the Miozza basin displayed in shaded relief maps.

DTMs at both resolutions were firstly depicted and successively processed in order to create the *Flow Directions*, *Local Slope* (*Figure 3.26*) and *Specific Catchment Area* raster grid files; once again these procedure were implemented by the D-Infinity method (Tarboton, 1997) proposed by the TauDEM 5.0 Toolbox.

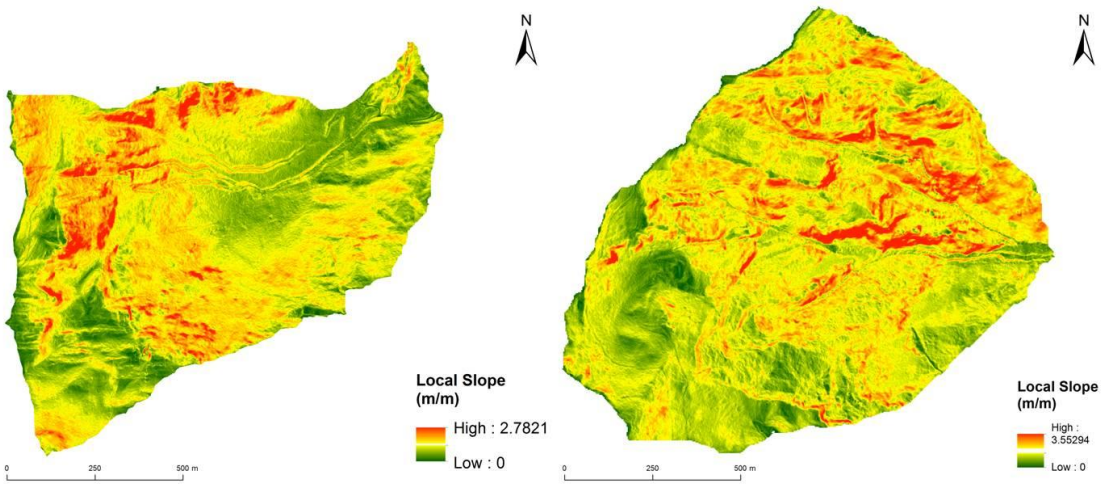

Figure 3.26 - Local Slope maps of the study areas A (left) and B (right) of the Miozza basin as derived from the 1m DTMs. The steepest values are represented in red color, the lowest values are green colored. Computations were developed using the TauDEM 5.0 software.

The *Upslope Drainage Area* was then elaborated by multiplying the SCA values by the cell size specific to each raster (1m or 3m according to the analyzed raster file), as displayed in *Figure 3.27*.

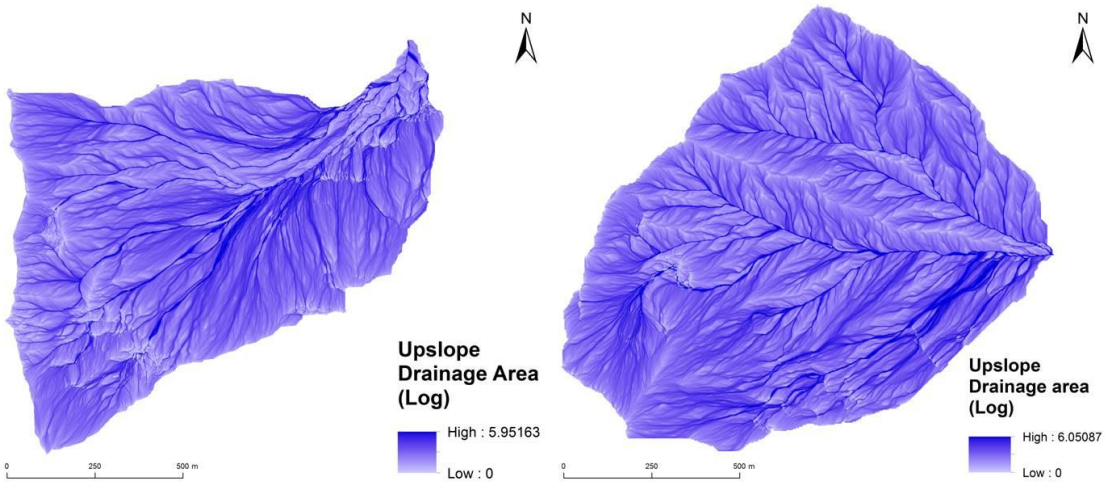

Figure 3.27 - Upslope Drainage Area maps of the study areas A (left) and B (right) of the Miozza basin as derived from the 1m DTMs. Computations were developed using the TauDEM 5.0 software.

In addition, the same SCA raster files were still used to compute the *Topographic Wetness Index* as in *Equation 3.19* and the resulted raster grid files are shown in *Figure 3.28*.

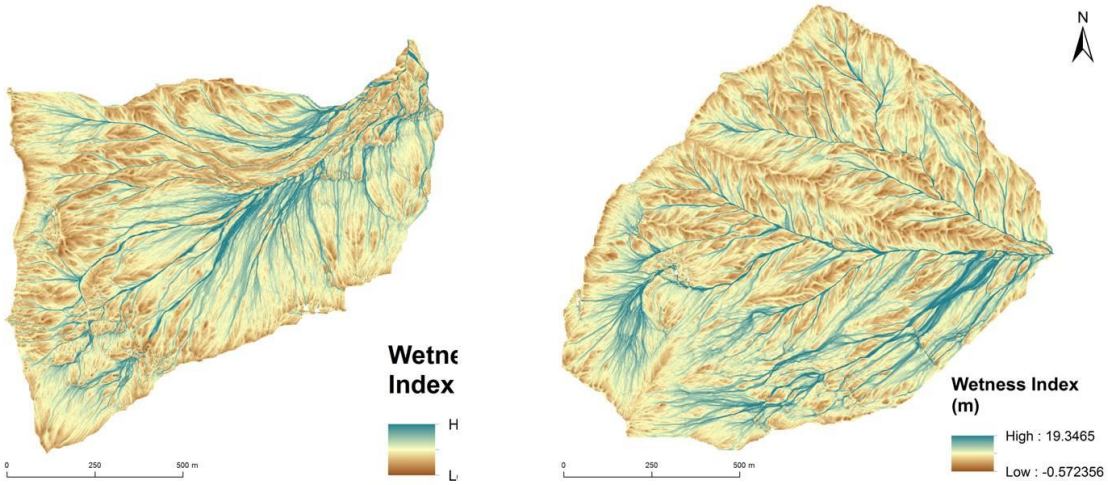

Figure 3.28 - Topographic Wetness Index maps of the study areas A (left) and B (right) of the Miozza basin as derived from the 1m DTMs. To higher values of WI correspond to more saturated areas.

The original DTMs were finally applied in the data processing of the *Aspect* (*Figure 3.29*) and *Mean Curvature* raster files (*Figure 3.30*). The latter has been achieved in the LandSerf 2.3 environment by choosing kernel sizes based again on the findings by Pirotti and Tarolli (2010) (*Paragraph 2.3.5*). In order to be consistent with that work, for the Miozza catchment a moving window of 15x15 cell (in the case of 1 m DTM) and 5x5 cell (in the case of 3 m DTM) has been adopted for the calculation of landform curvature. In this way, both curvature raster files resulted in a 15m scale, which was indicated by the authors to be the best resolution to detect morphologic features in alpine catchments where channels present a bankfull width ranging from 1 to 5 m.

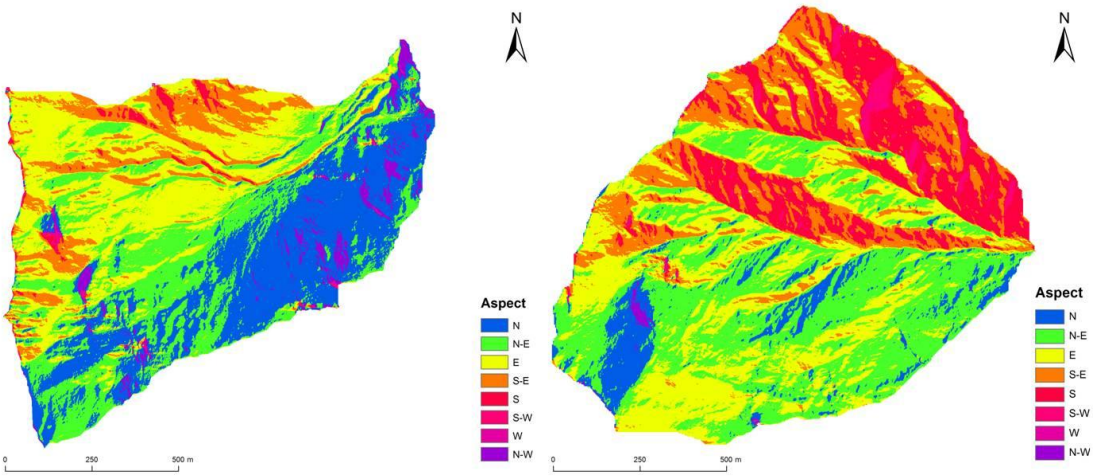

Figure 3.29 - Aspect maps of the study areas A (left) and B (right) of the Miozza basin as derived from the 1m DTMs.

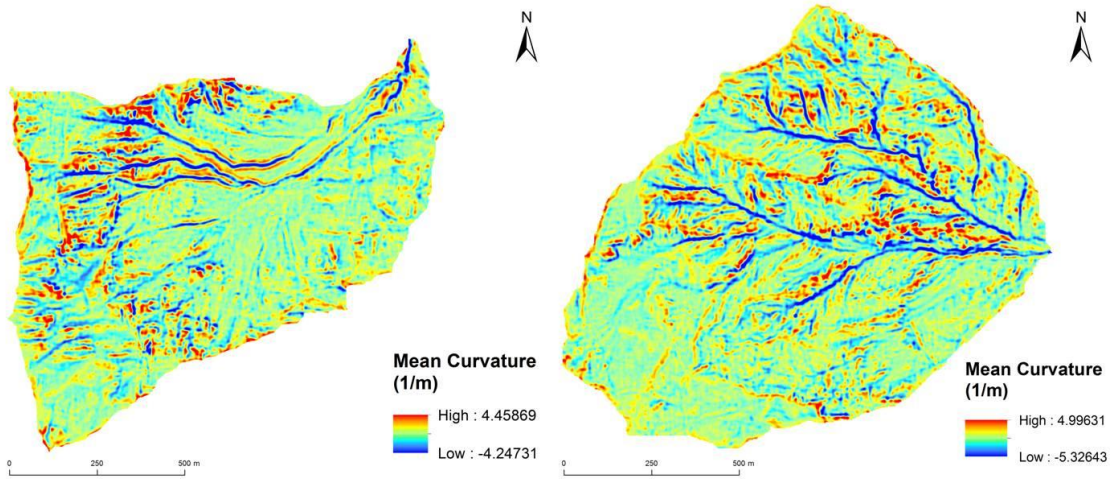

Figure 3.30 - Mean Curvature maps of the study areas A (left) and B (right) of the Miozza basin as derived from the 1m DTMs. Raster files were processed with a 5x5 moving window, using the LandSerf 2.3 software.

As it was done for the Cetus basin, the obtained raster files have been successively extracted on the base of each vegetation class described above. This step allowed to extract such morphometric parameters for each vegetation type considered for both the two sub basin examined, both at 1m and 3m resolutions.

4 RESULTS AND DISCUSSIONS

The analysis of the obtained results will be mainly focused on the slope-area and curvature-area relationships, since they have permitted the best interpretation of the linkage between local morphologies and vegetation types over the study areas. S-A and C-A plots for the Cetus basin have been reported at both the 5 m and 10 m resolutions, but further analysis of the results have been focused on the finer scale due to its higher detail. Concerning the Miozza basin as well, S-A and C-A general plots have been shown either at 1 m and 3 m resolutions, although the diagrams relative to the comparisons among vegetation classes have been reported only at the coarser scale. This because it allows to neglect the noise that is obviously present with the higher resolution of 1 m, which is however well performing (Tarolli and Dalla Fontana, 2009). Other statistics will be illustrated to support the understanding of the most significant relations.

4.1 Cetus basin

Topographic data available for the Cetus basin allowed to perform the data analysis at two levels of resolution, due to the elaboration of the 5 m and 10 m grid sizes DTMs. Therefore, their relative plots will be here reported and compared to each other.

According to the threshold criterion exposed by Ijjaz-Vasquez and Bras (1995) and confirmed by Tarolli and Dalla Fontana (2009), four regions have been detected in each analyzed S-A relation. Region I presents low values of drainage area and a positive slope gradient and it is related to hillslope-diffusive sediment transport, Region II consists in a negative gradient with increasing drainage area that depicts a change in landform toward concave unchanneled valleys, Region III is characterized by a less distinct negative gradient and is related to a debris flow-landslides dominated landscape, and region IV presents a strongly negative gradient featuring the dominance of alluvial channels. Below are reported the slope-area (*Figure 4.1* and *Figure 4.3*) and curvature-area diagrams (*Figure 4.2* and *Figure 4.4*) for the Cetus basin for both 5 m and 10 m resolutions.

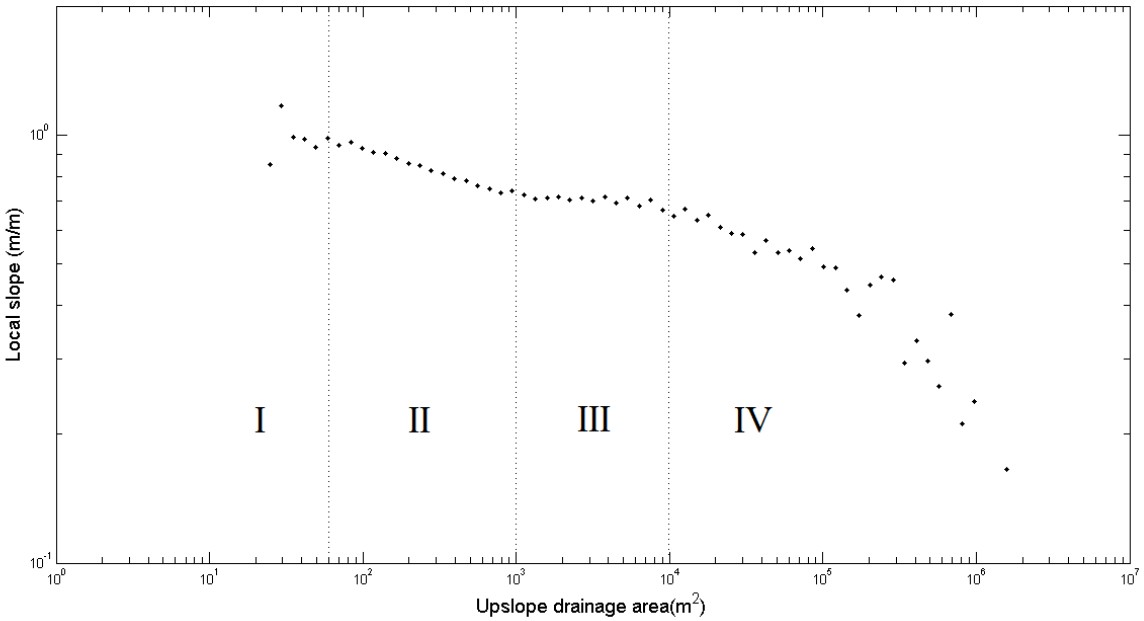

Figure 4.1 - Slope-area (S-A) plot for the Cetus basin at 5 m resolution.

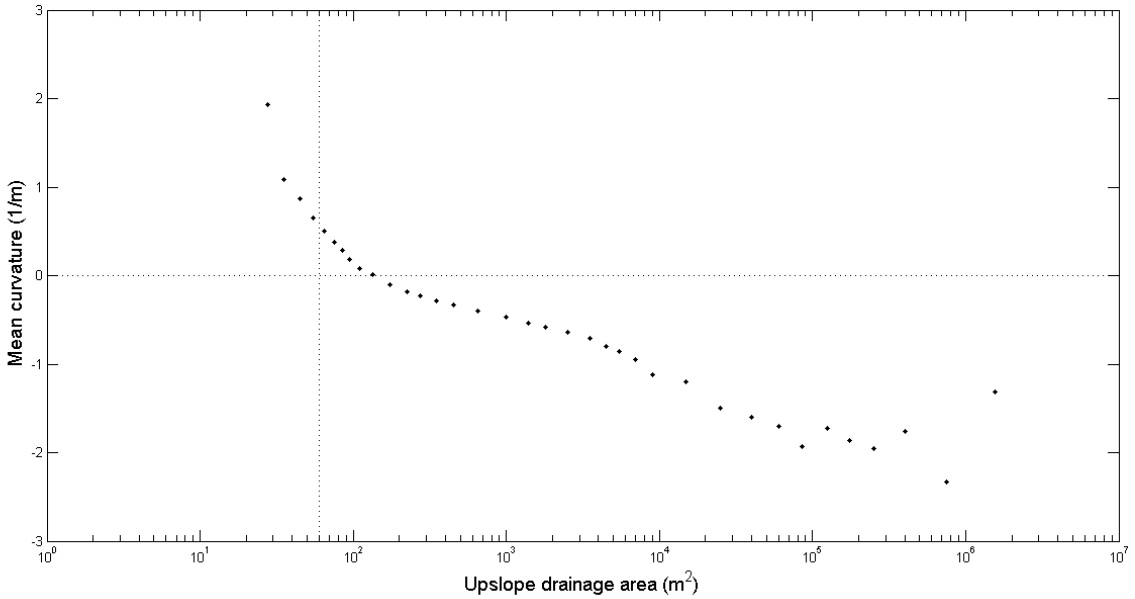

Figure 4.2 - Curvature-area (C-A) plot for the Cetus basin at 5 m resolution.

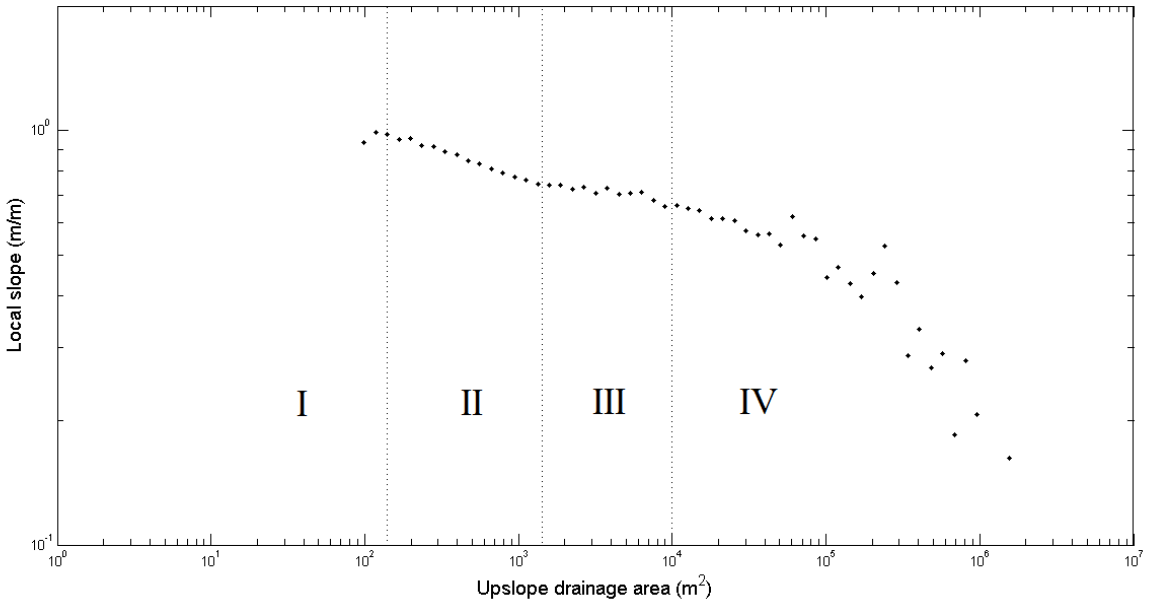

Figure 4.3 - Slope-area (S-A) plot for the Cetus basin at 10 m resolution.

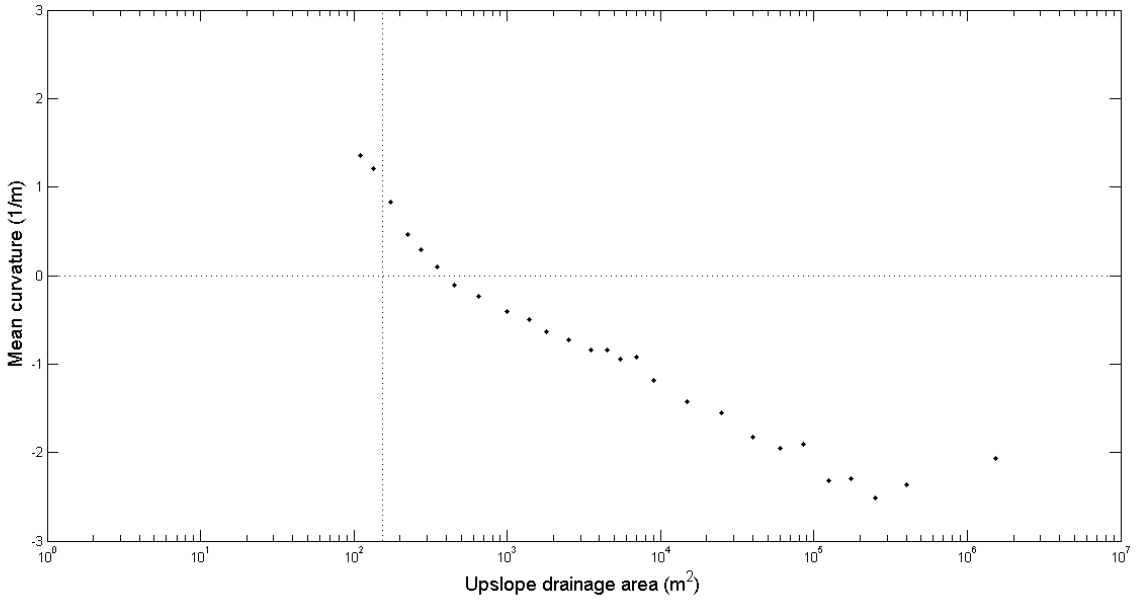

Figure 4.4 - Curvature-area (C-A) plot for the Cetus basin at 10 m resolution.

As it is possible to see from *Figure 4.1* and *Figure 4.3*, the slope-area plots are similar for both resolutions and the abovementioned four regions are easily detectable. Only the turnover point from Region I to Region II is lightly shift toward higher values of drainage area for the 10 m resolution plot (~ 150 m^2) respect to the 5 m resolution plot (~ 60 m^2). This behavior is also recognizable in the results by Tarolli and Dalla Fontana (2009), where the slope-area graphs relative to different grid size resolutions exhibit increasing upslope area values at the hillslope to valley transition coupled with a decrease in resolution. The loss in resolution

indeed, could lead to misreckon the transition from divergent hillslope to convergent valley morphologies due to a smoothed topographic representation. *Figure 4.2* and *Figure 4.4* show the transition from divergent landform profiles, characterized by positive values of curvature, to convergent morphologies with negative curvature values. In the case of the Cetus study area, in opposition to the other areas analyzed in the Miozza basin, no match can be found between the change in the sign of curvature values and the slope-area threshold from hillslope diffusion to valley incision, thus detecting a higher contributing area to mark this change in profile concavity. This transition in landform curvature is rather site specific, therefore a correspondence with the shift from convex hillslope to concave valley described by the S-A relation cannot always be found. Moreover, a progressive decrease in curvature values from the higher to the coarser resolution is detectable, as predicted by Tarolli and Dalla Fontana (2009). Also, a moderate increase in curvature values can be distinguished in *Figure 4.2* in correspondence of Region III of the S-A plot at same resolution; while the C-A relation for the 10 m resolution analysis presents a steeper decrease in values than the one at finer scale (*Figure 4.4*).

Significant results have been obtained from the comparisons of the slope-area and curvature-area plots relative to the different vegetation types, as depicted in *Figure 4.5*, *Figure 4.6*, *Figure 4.8*, and *Figure 4.9* where also the concavity index (θ) values are reported. It is worth remembering that this parameter appears in *Equation 1.16* where it was defined to relate the local slope of a given point on the landscape to its contributing area value.

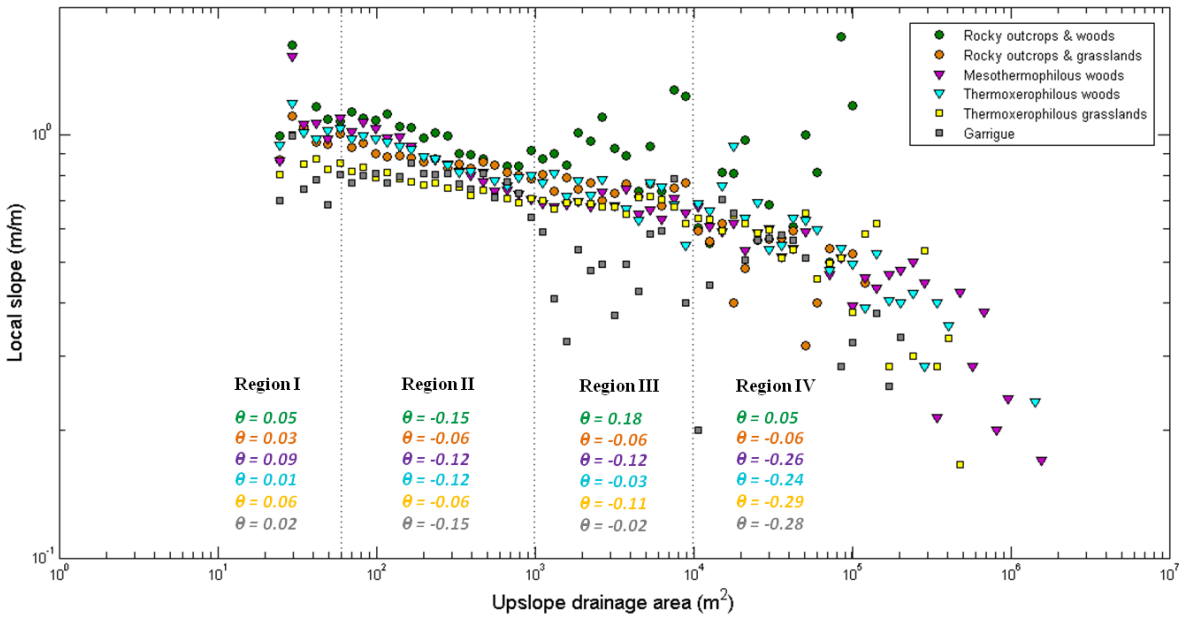

Figure 4.5 - Slope-area plots of the Cetus basin at 5 m resolution, relative to each vegetation type. For the four regions detected the concavity index (θ) corresponding to each vegetation type is displayed as well.

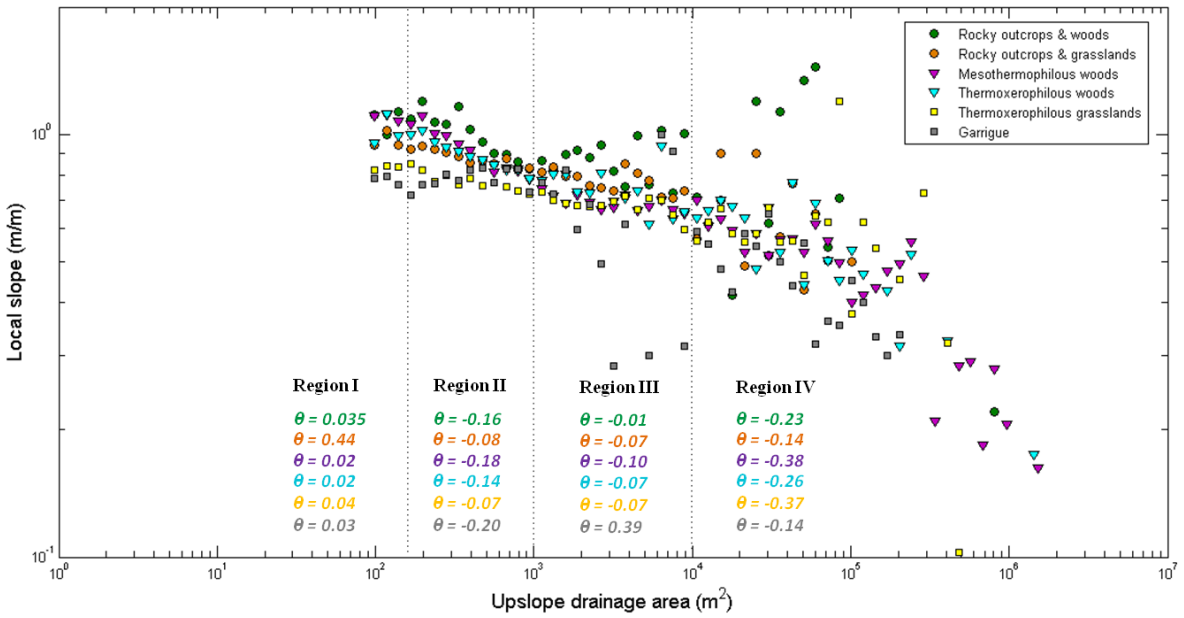

Figure 4.6 - Slope-area plots of the Cetus basin at 10 m resolution, relative to each vegetation type. For the four regions detected the concavity index (θ) corresponding to each vegetation type is displayed as well.

Looking at the graphs above, it emerges that vegetation classes are found to dispose according to different values of slope and drainage area based on their specific attitudes and also the concavity index (θ) values of each vegetation typology vary with their patterns along with the

change in gradient throughout the four regions. What is possible to note from both resolutions is that the classes characterized by the presence of rocky outcrops are mainly located in correspondence of the highest values of local slope and lowest values of drainage area. In particular, the "rocky outcrops and woods" class plots on the steepest slopes, with higher values than the "rocky outcrops and grasslands" class. Moreover, the former also presents the highest negative value of concavity index (θ) in Region II and the highest positive value in Region III of the S-A plot at 5 m resolution; whereas the "Rocky outcrops and grassland" vegetation type presents in the same diagram similar θ values throughout all the four classes. This can be related to the deeper and stronger root system owned by the woody vegetation respect to the herbaceous species, which allows standing species to distribute on steeper terrain morphologies. To what concerns the "thermoxerophilous grasslands" and "garrigue" vegetation classes they are both related to low values of local slope and moderately high values of upslope drainage area, even if the garrigue presents a more cluttered pattern than the other class. This can also be evaluated by looking at their θ values that result to be more constant for the former class and more extreme for the latter whose ranges go from the lowest values of -0.15 (5 m resolution graph) and -0.20 (10 m resolution graph) in Region II to the highest value of -0.02 (5 m resolution graph) and 0.39 (10 m resolution graph) in Region III.
Additionally, a relevant difference can be noticed between the distributions of the mesothermophilous and thermoxerophilous vegetation types (see *Figure 4.7*). As it is easily detectable also by looking at their concavity index (θ) values, both the two classes generally plots for relatively steep slopes in Region I, then turn to less steep slopes in Region II, with a strong negative gradient (θ*=-0.12* for both classes). In Region III they both go back to slightly higher values of slope (especially the thermoxerofilous one) with a less negative gradient and finally go down to lower values of slope in correspondence of the channelized morphology of Region IV. However, although these two classes present a similar pattern, they also diverge in some areas of the diagram: in Region I the mesothermofilous woods are characterized by slightly higher values of slopes than the thermoxerophilous woods; while, in Region III the latter overcome the former, thus presenting higher slope values and a less negative concavity index value (θ*=-0.03*) respect to the one of mesothermophilous vegetation (θ*=-0.12*) that instead remains equal to Region II of the same class. This may lead to an interpretation of the thermoxerophilous vegetation type's behavior which results in the

preference of relatively high values of slope and drainage area that can be congruous with the debris flow-landslide dominated processes typically detected in Region III.

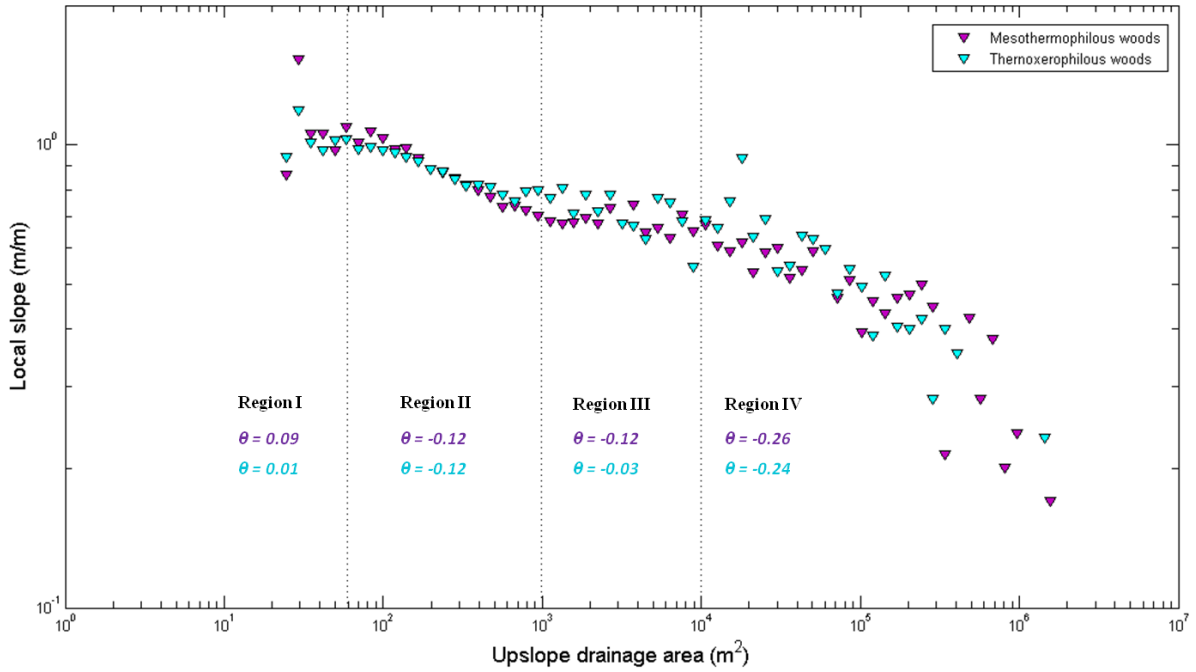

Figure 4.7 - Slope-area plots of the Cetus basin at 5 m resolution, relative to the "Mesothermophilous woods" and "Thermoxerophilous woods" vegetation classes with their concavity index (θ) values.

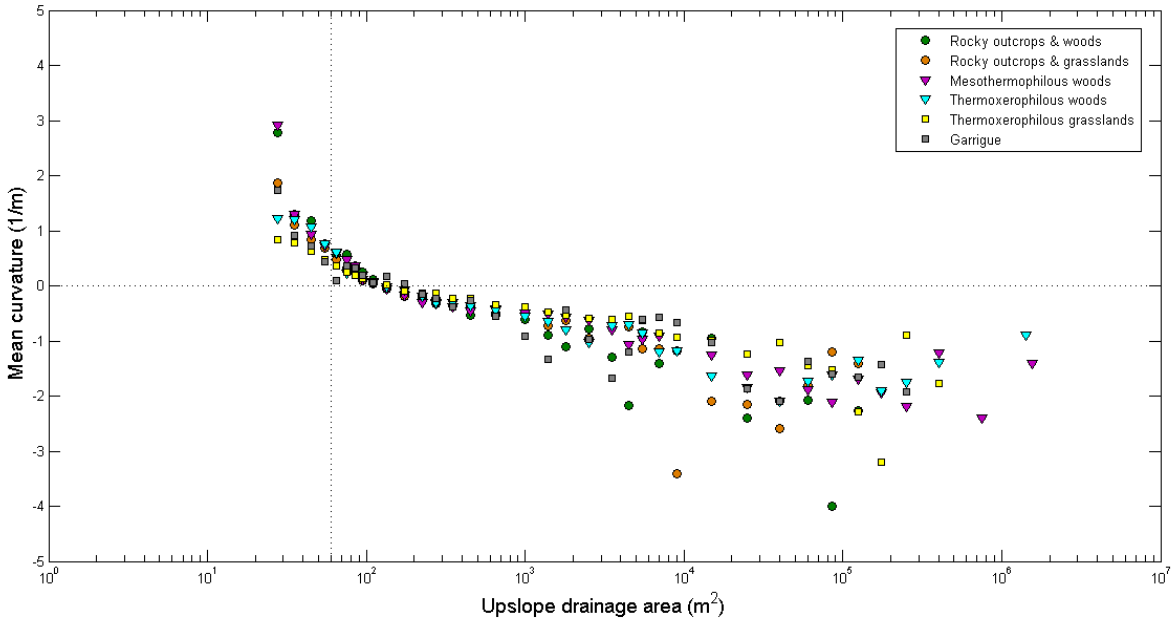

Figure 4.8 - Curvature-area (C-A) relations for the Cetus basin at 5 m resolution, relative to each vegetation type.

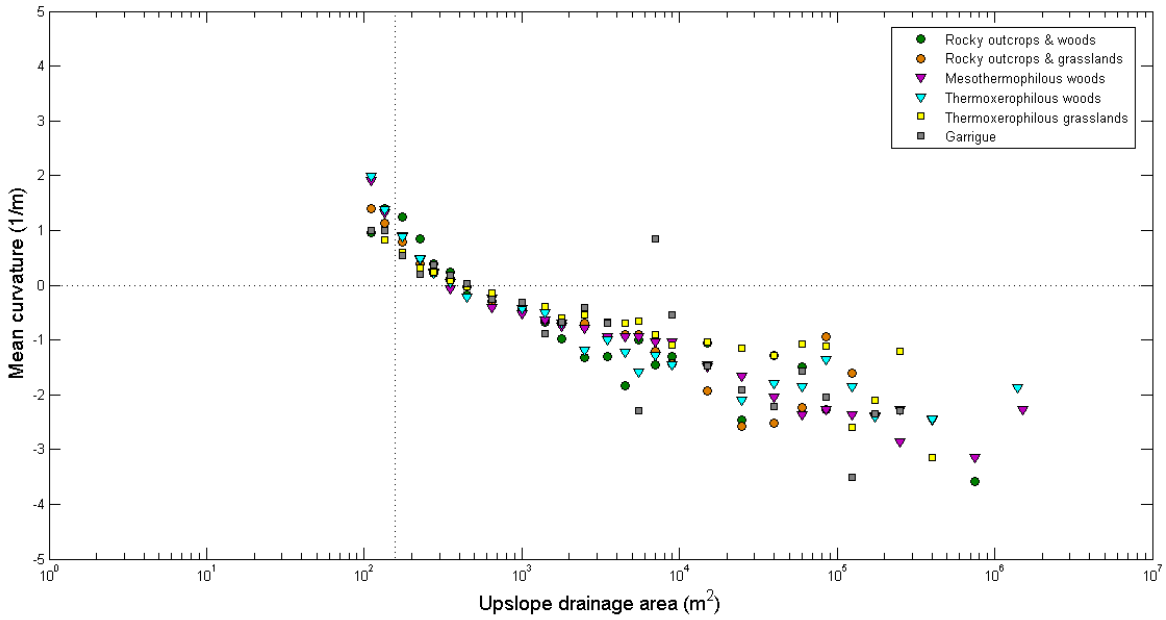

Figure 4.9 - Curvature-area (C-A) relations for the Cetus basin at 10 m resolution, relative to each vegetation type.

To what concerns the C-A relations, change in the sign of curvature from positive to negative values seems to occur with drainage area values slightly higher than those detected from the slope-area hillslope to valley transition, as already indicated by looking at *Figure 4.2* and *Figure 4.4*. Diagrams at both resolutions reveal that vegetation types which presented steeper slopes in the S-A plots (i.e. "Rocky outcrops & woods", "Mesothermophilous woods" and "Thermoxerophilous woods") are related to a higher degree of ridge divergence and valley convergence in their relative C-A plots. These results are consistent with the landform analysis by Yetemen et al. (2010). On the contrary, types of vegetation that plotted over lower values of local slope in the S-A relation, present a smoother gradient in the transition from divergent to convergent profile curvatures in their C-A plots.

Some more sentences have to be spent in the particularly interesting comparison between the S-A plots of the vegetation classes of mesothermophilous and thermoxerophilous woods. To this purpose, further observations are proposed in *Figure 4.10* and *Figure 4.11* only at 5 m resolution, since there are no significant differences at the other scale.

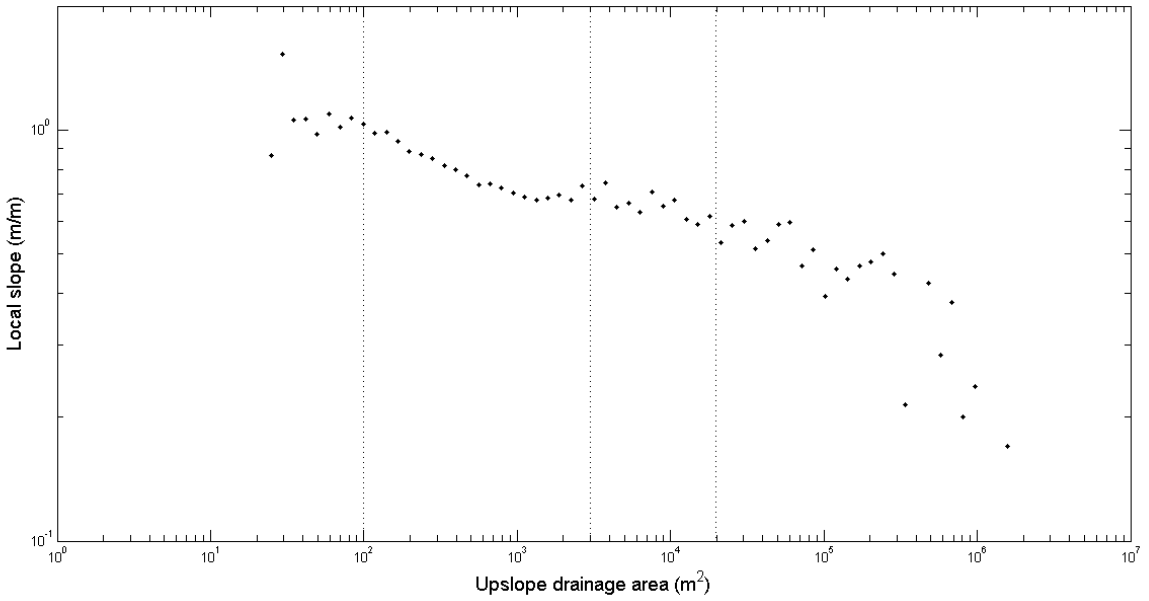

Figure 4.10 - Slope-area relation for the vegetation class "Mesothermophilous woods" at 5 m resolution.

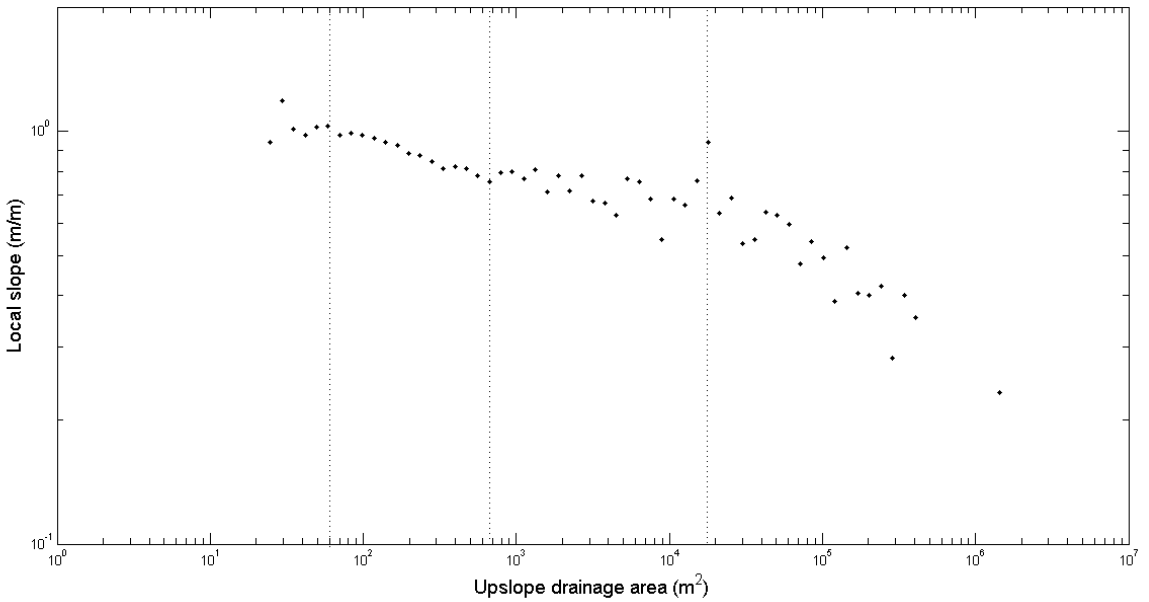

Figure 4.11 - Slope-area relation for the vegetation class "Thermoxerophilous woods" at 5 m resolution.

The threshold from Region I to Region II does not occur at the same values of drainage area for the two classes. This suggests that the hillslope to valley transition may be shift toward higher values of contributing area for the mesothermophilous woods, which also means a more downslope position in the basin. The same class also reaches values of drainage area up to twofold respect to the other vegetation type, as it is appreciable by their statistical analysis furnished in *Table 4.1*. As a matter of facts, looking at the table, except for the minimum

values that are equal for the vegetation classes in analysis, all the other statistical values of drainage area are greater for the mesothermophilus woods than for the thermoxerophilous woods.

Table 4.1 - Statistical analysis of the vegetation classes "Mesothermophilous woods" and "Thermoxerophilous woods" at 5 m resolution, according to their upslope drainage area values (m^2).

	Min. value	Max. value	Mean value	Median	St. deviation
Mesothermophilous woods	25.00	2087879.00	12897.00	231.9294	108290.00
Thermoxerophilous woods	25.00	1825800.00	4056.00	173.4316	54393.00

In addition, from the S-A plots in *Figure 4.10* and *Figure 4.11* is possible to note that Region II is more extended for the mesothermophilous vegetation at the expense of a much restricted Region III, in comparison with the same regions for the thermoxerophilous woods class. This one conversely, distributes well in Region III and also presents slightly higher values of local slope. The plot in Region IV of this vegetation type is characterized by moderately lower values of drainage area respect to the mesothermophilous one.

Furthermore, it has been considered appropriate to report also the box plot analysis for the aspect parameter of the different vegetation types at 5 m resolution, which is reported in *Figure 4.12*.

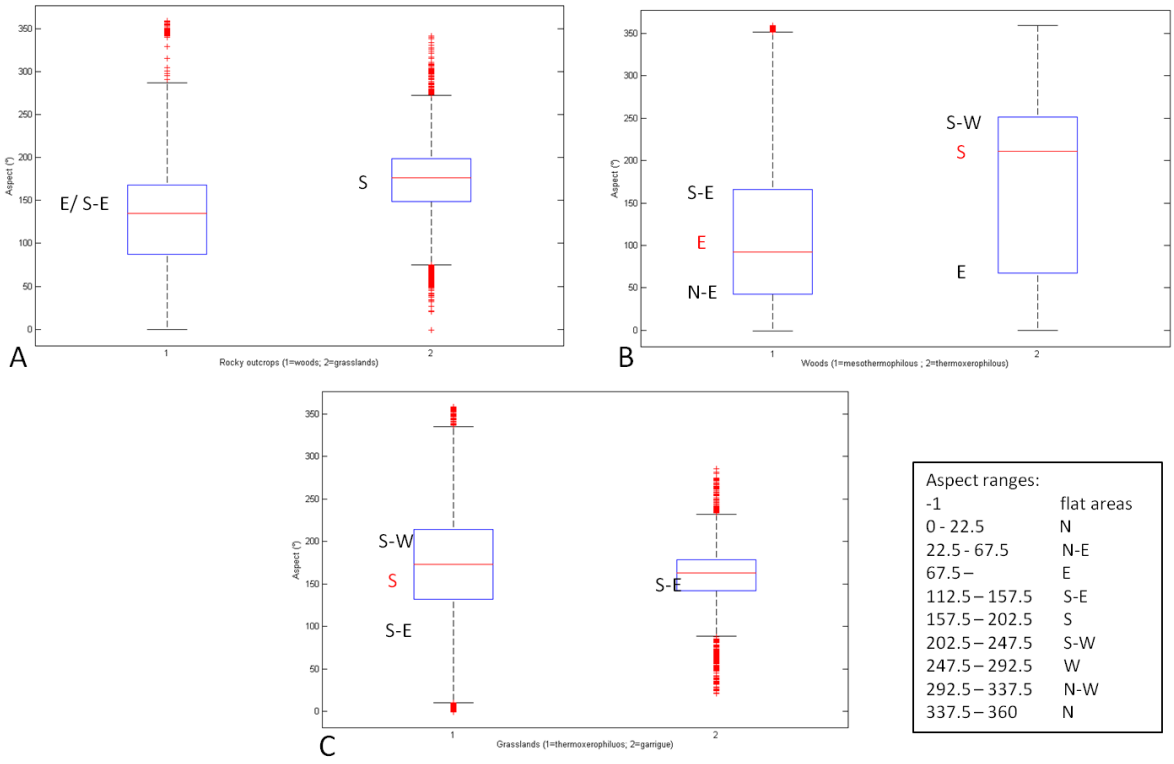

Figure 4.12 - Box plot representation of the aspect parameter at 5 m resolution: A. comparison between the vegetation classes "Rocky outcrops & woods" and "Rocky outcrops & grasslands"; B. comparison between the classes "Mesothermophilous woods" and "Thermoxerophilous woods"; C. comparison between the classes "Thermoxerophilous grasslands" and "Garrigue".

According to the box plot statistical analysis, most of the data are plotted within the square boxes, which represent the distribution from its first to third interquartile range, while the black whiskers represent the remaining part of the distribution. The red horizontal lines are supposed to indicate the median value of the distribution, and the red crosses are the outliers. Moderate differences can be detected from the types of vegetation, since the South-East orientation prevails. In particular, from the diagram in *Figure 4.12-B*, it is noticeable how the mesothermophilous woods better distribute toward the East/North-East aspect values, while the thermoxerophilous vegetation prefers a South/South-West orientation. This behavior is quite easily observable by looking at *Figure 4.13*.

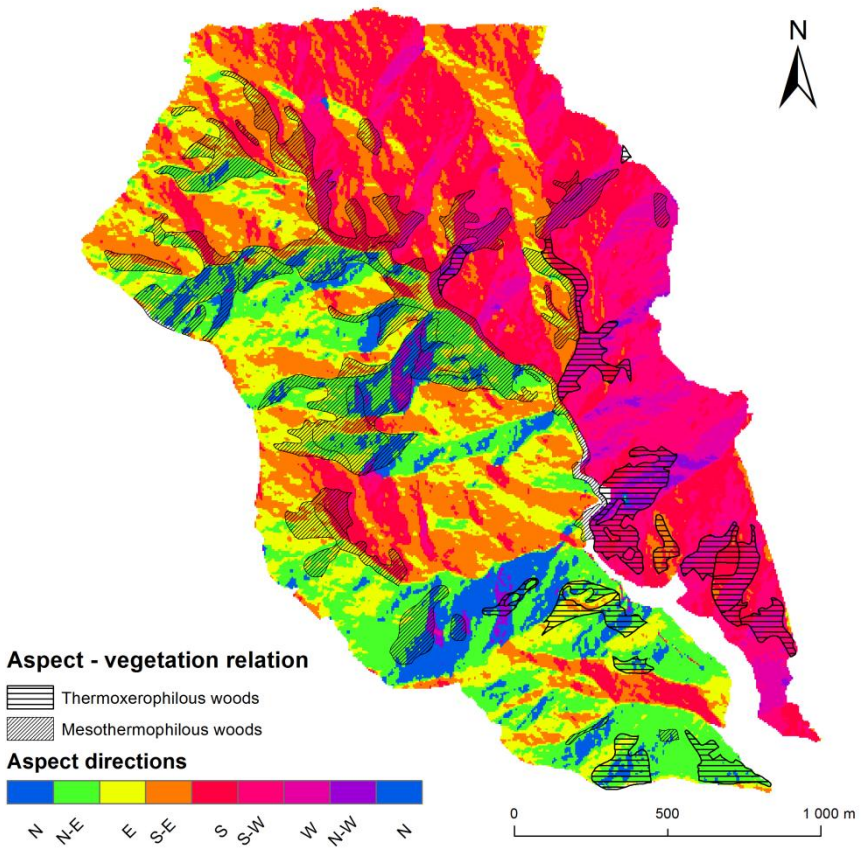

Figure 4.13 - Aspect maps of the Cetus basin obtained from the 5m DTM in relation with the "Mesothermophilous woods" and "Thermoxerophilous woods" vegetation type distribution patterns

Once again, box plots analysis is a useful representation to what concerns the topographic wetness index parameter (TWI) as well. *Figure 4.14* reports the distributions of this topographic indicator along with the different vegetation classes.

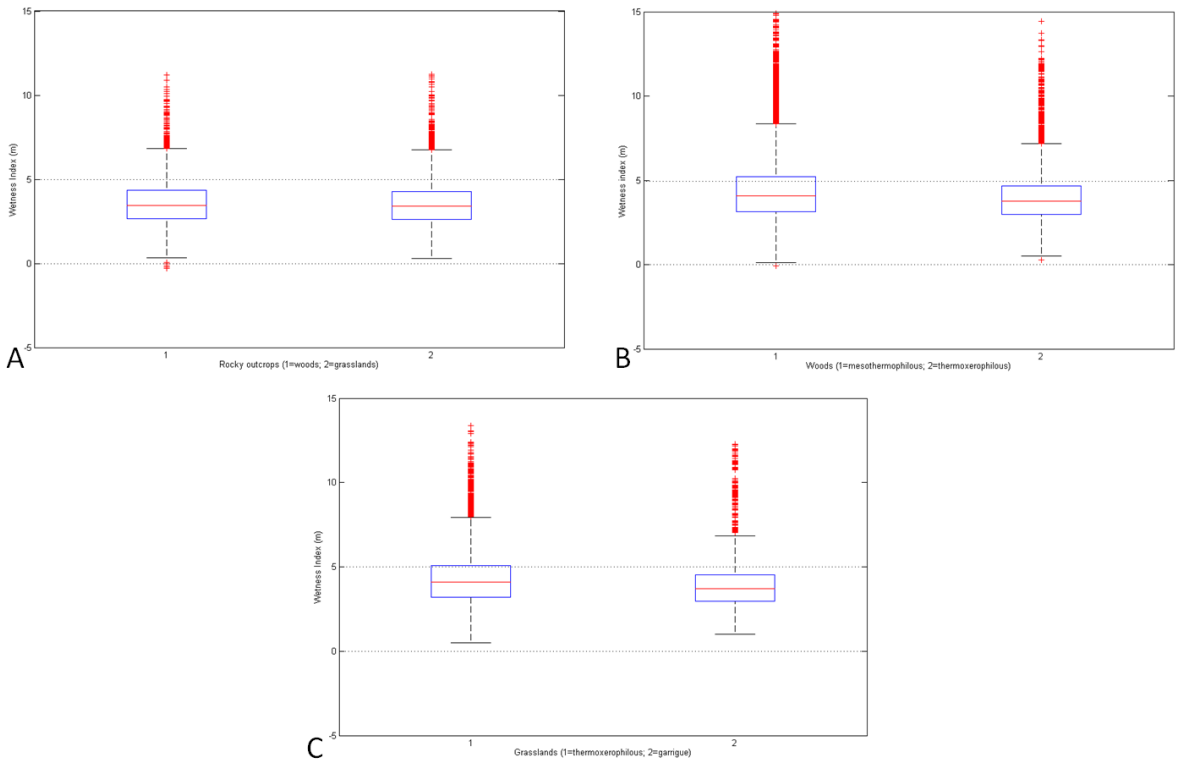

Figure 4.14 - Box plot representation of the Topographic Wetness Index parameter at 5 m resolution: A. comparison between the vegetation classes "Rocky outcrops & woods" and "Rocky outcrops & grasslands"; B. comparison between the classes "Mesothermophilous woods" and "Thermoxerophilous woods"; C. comparison between the classes "Thermoxerophilous grasslands" and "Garrigue".

Although the distributions result quite similar one to the others, the vegetation class of "Mesothermophilous woods" seems to moderately range toward higher values of TWI than the "Thermoxerophilous woods" one, this may be related to the specific moisture vegetative conditions of the former; the same behavior can be detected for the "Termoxerophilous grasslands" respect to the "Garrigue" vegetation types.

To better evaluate this index, its statistical values are also reported for each type of vegetation in *Table 4.2*. From this table, emerges that the mesotermophilus class shows the highest mean and maximum TWI values.

Table 4.2 - Statistical analysis of all the vegetation classes and the whole basin at 5 m resolution, according to their wetness index values (m).

	Min.value	Max.value	St.Deviation	Mean value	Median
Rocky outcrops & woods	-0.2939	11.2108	1.3148	3.5752	3.4594
Rocky outcrops & grasslands	0.2957	11.2300	1.3085	3.5481	3.4057
Mesothermophilous woods	-0.0831	14.8978	1.9815	4.4064	4.0743
Thermoxerophilous woods	0.2581	14.4172	1.5829	3.9697	3.7501
Thermoxerophilous grasslands	0.5120	13.3864	1.5466	4.2532	4.0947
Garrigue	0.9976	12.2771	1.8343	4.0541	3.7142
Whole basin	-0.5900	14.8978	1.6110	4.0708	3.8687

4.2 Miozza basin

Results carried out from the analyses of the two headwater catchments of the Miozza basin according to the resolutions of 1 m and 3 m, are presented in this paragraph. Firstly, the general trends for the slope-area and curvature-area relations are displayed in two distinct subparagraphs, since both resolutions are presented for the data analysis of each study area. In a third subparagraph, the results relative to each sub-basin will be reported and compared, presenting the distributions of each vegetation typology. For these latter evaluations only the 3 m resolution data have been considered, since no significant differences with the finer resolution have been found; moreover, it is worth remembering that a 3 m resolution allows to ignore the noise presented by the higher resolution of 1 m, which is however well performing (Tarolli and Dalla Fontana, 2009).

4.2.1 Study area A

In relation to 1 m and 3 m grid resolutions of the original DTMs results of the S-A plots for the study area A are reported in *Figure 4.15* and *Figure 4.17*, while results of the C-A plots for the same study area are presented in *Figure 4.16* and *Figure 4.18*.

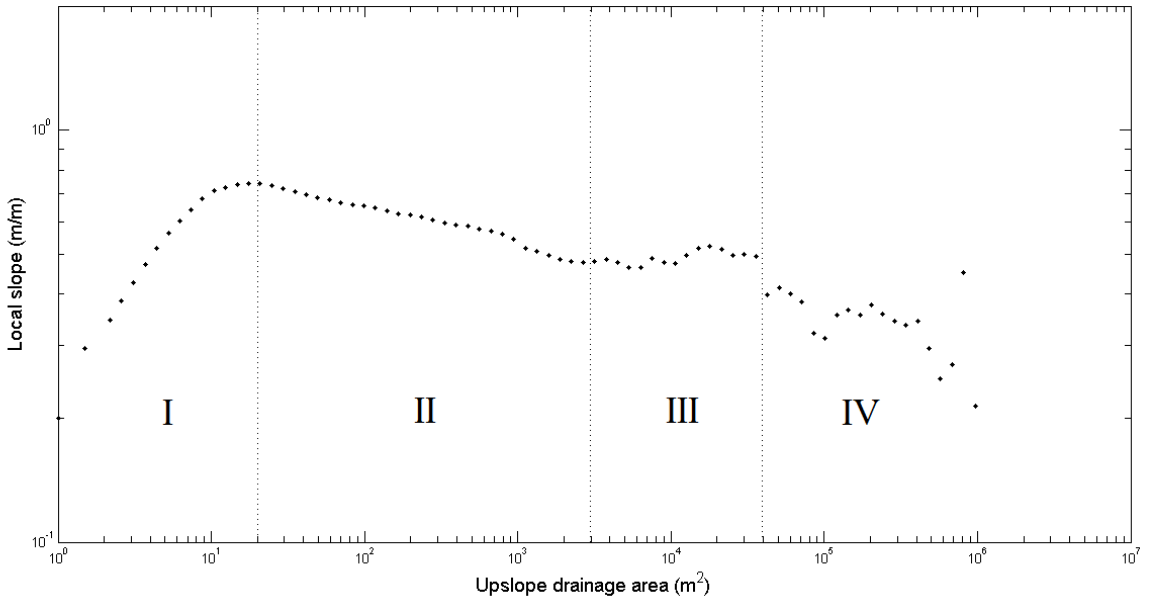

Figure 4.15 - Slope-area (S-A) plot for the study area A of the Miozza basin at 1 m resolution.

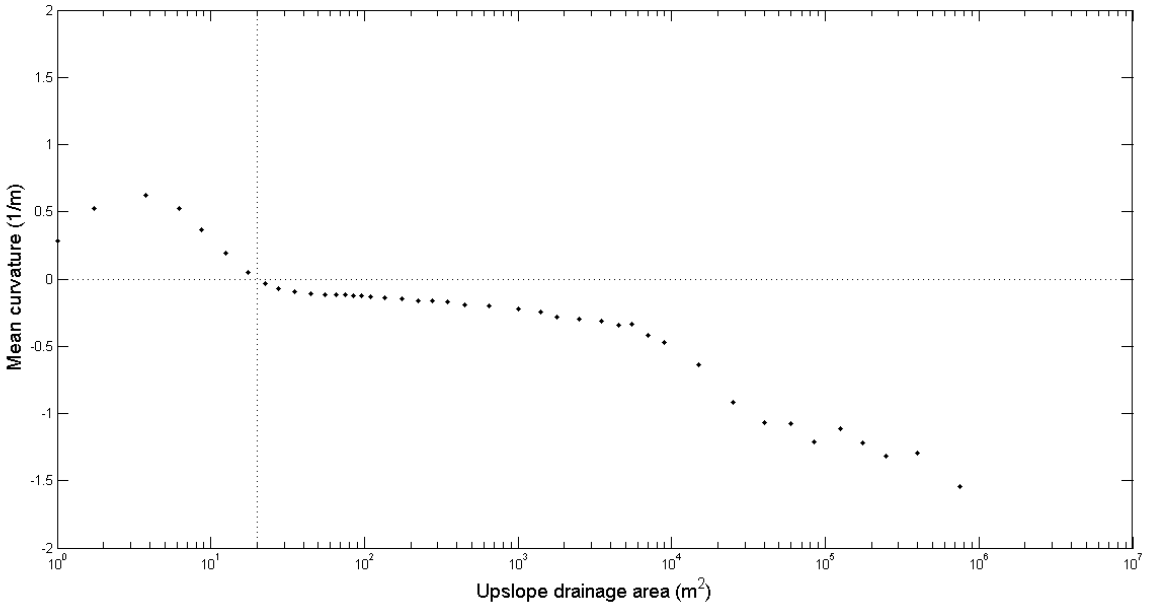

Figure 4.16 - Curvature-area (C-A) plot for the study area A of the Miozza basin at 1 m resolution.

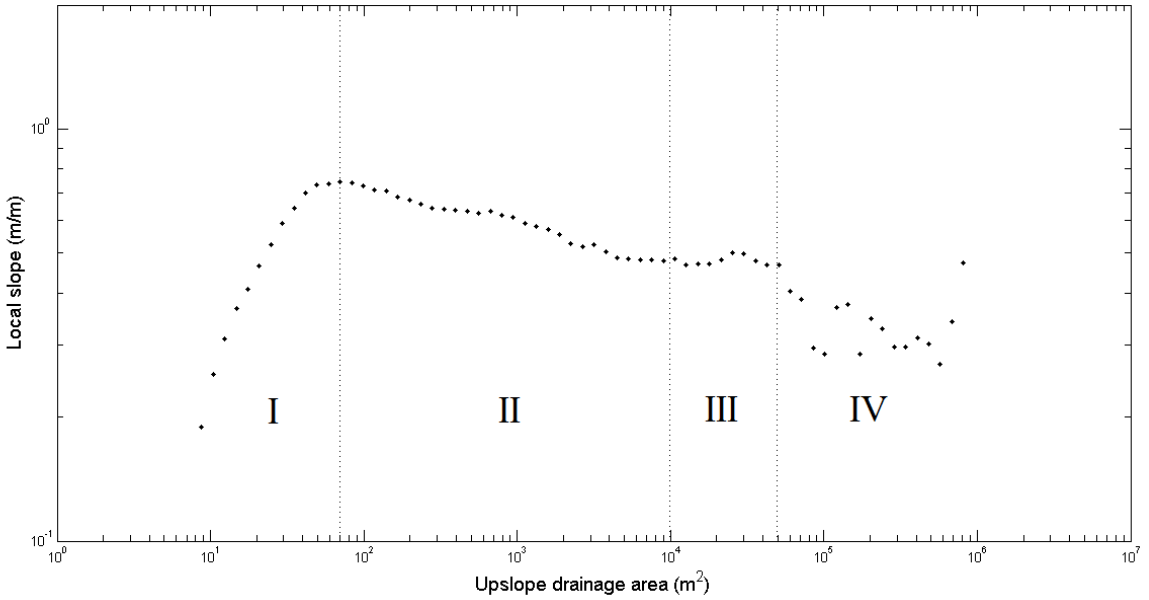

Figure 4.17 - Slope-area (S-A) plot for the study area A of the Miozza basin at 3 m resolution.

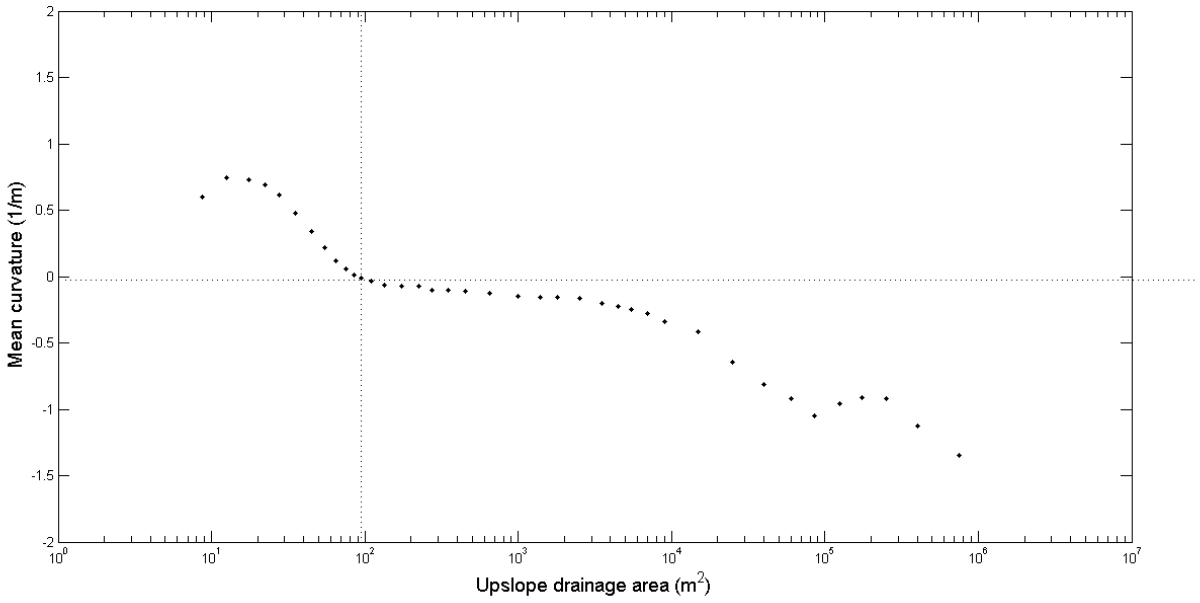

Figure 4.18 - Curvature-area (C-A) plot for the study area A of the Miozza basin at 3 m resolution.

The slope-area relations showed in *Figure 4.15* and *Figure 4.17* illustrate the threshold values detecting the four regions for study area A, with respect to 1 m and 3 m grid sizes of the processed DTMs. Coherently again with Tarolli and Dalla Fontana (2009), differences in resolution exhibit a shift of all the three thresholds (Regions I to II, II to III and III to IV) toward higher values of upslope drainage area, from higher to coarser resolutions, as it has

been registered for the Cetus basin as well. The transition from hillslope-diffusive sediment transport processes of Region I to slope-advective sediment transport processes of Region II occurs at about 20 m^2 of contributing area for the 1 m resolution analysis and 70 m^2 for the 3 m resolution one. While the transitions from Region II to III and from Region III to IV occur respectively at $3 \cdot 10^3$ m^2 and $4 \cdot 10^4$ m^2 for the 1 m resolution, opposing to the 10^4 m^2 and $5 \cdot 10^4$ m^2 of the 3 m resolution scale. This means that, for the coarser resolution, the range of contributing area identifying Region III is narrower than the same region of the finer resolution plot, thus suggesting that the coarser topographic representation may detect a smaller area of the basin to be subject to debris flow-landslides dominated processes.
In opposition to the results obtained for the Cetus study area, *Figure 4.16* and *Figure 4.18* reveals for both resolutions that the change in planform curvature from positive to negative values corresponds well to the hillslope to valley transition of the S-A plots. Moreover, the C-A plots present a steeper decrease in values for drainage area amounts corresponding to Regions III and IV of the S-A plots than those corresponding to Region II.

4.2.2 Study area B

Results of the S-A (*Figure 4.19* and *Figure 4.21*) and C-A (*Figure 4.20* and *Figure 4.22*) plots in relation to 1 m and 3 m grid resolutions of the original DTMs are also reported for the study area B.

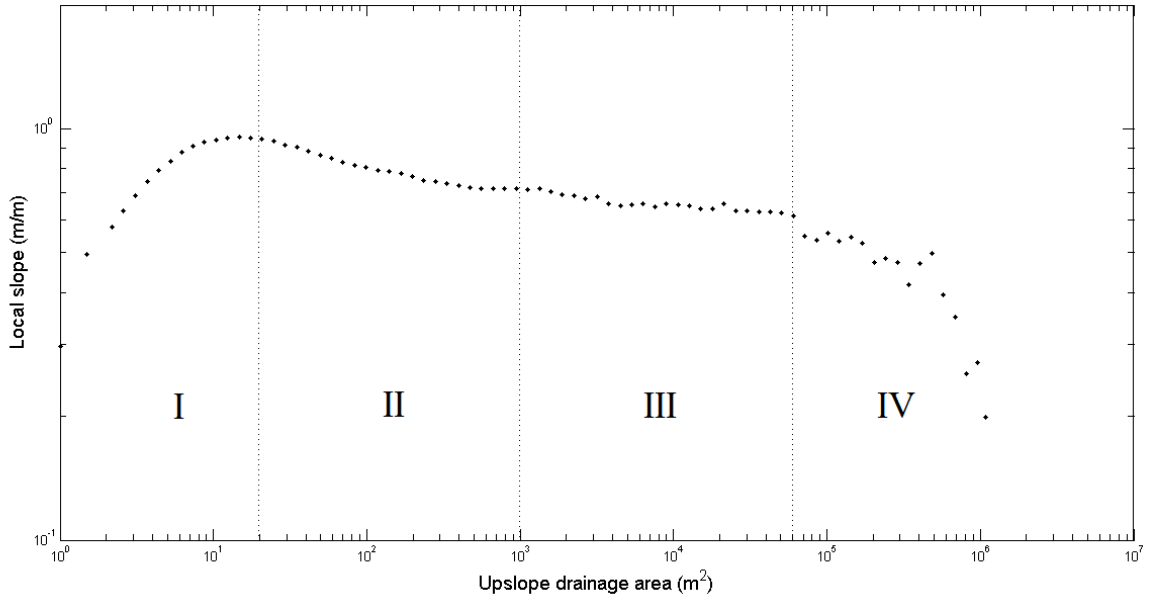

Figure 4.19 - Slope-area (S-A) plot for the study area B of the Miozza basin at 1 m resolution.

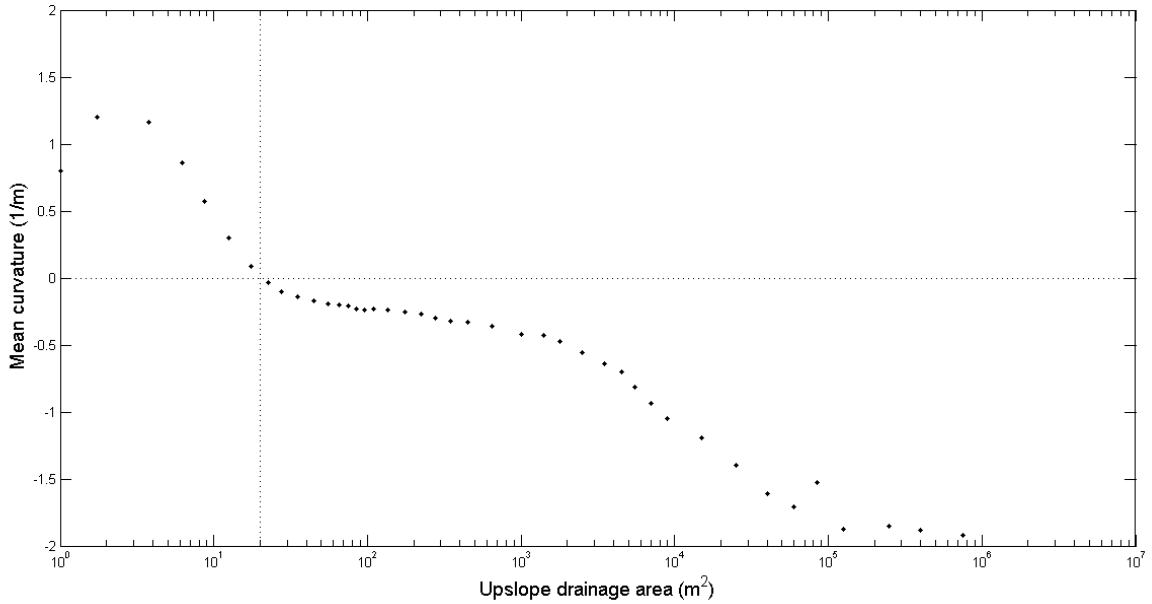

Figure 4.20 - Curvature-area (S-A) plot for the study area B of the Miozza basin at 1 m resolution.

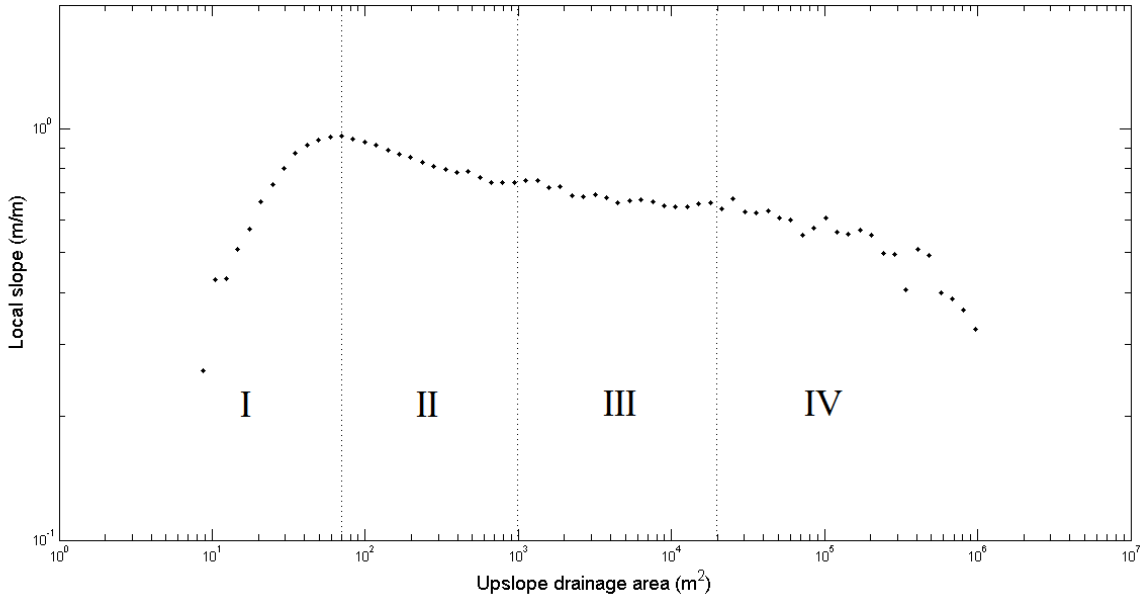

Figure 4.21 - Slope-area (S-A) plot for the study area B of the Miozza basin at 3 m resolution.

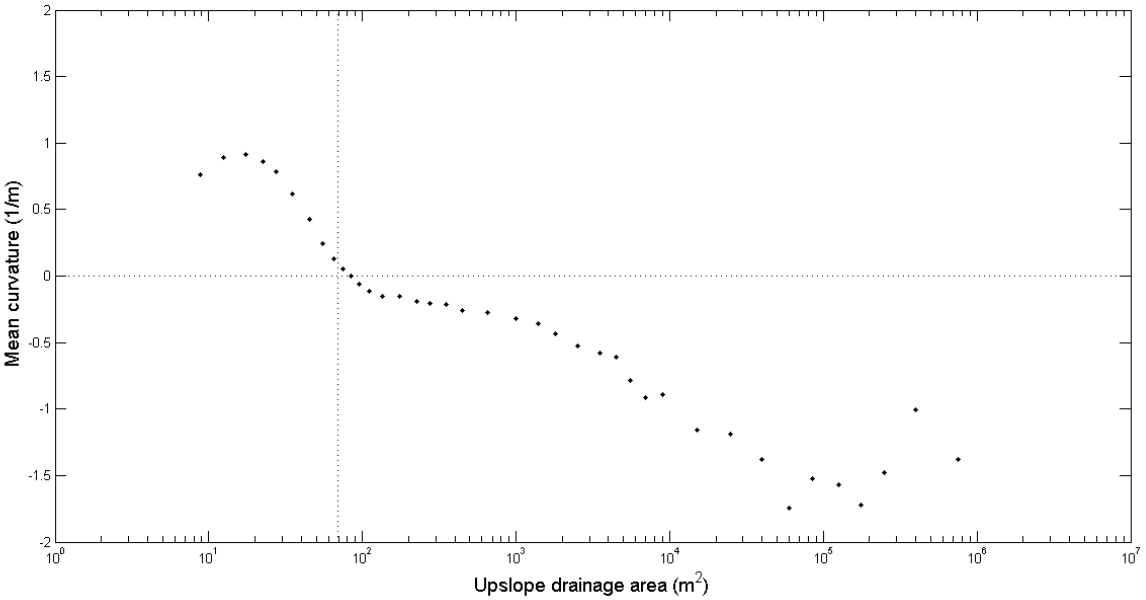

Figure 4.22 - Curvature-area (S-A) plot for the study area B of the Miozza basin at 3 m resolution.

Once again, from the slope-area relations displayed in *Figure 4.19* and *Figure 4.21* are detectable the four regions related to the dominance of different sediment transport processes. In the case of this specific study area B, the shift toward higher values of drainage area with decreasing resolution can only be recognized for the portion of the plot corresponding to the hillslope to valley transition. Indeed, the change from Region I to II is featured by a threshold

value of upslope area of about 20 m^2 for the 1 m resolution plot, in opposition to the value of 60 m^2 for the 3 m resolution diagram. Conversely to the trend showed by the other study areas, in this case the threshold from Region III to IV is characterized by a higher value of drainage area for the finer resolution ($6 \cdot 10^4$ m^2) than the value of the coarser resolution ($2 \cdot 10^4$ m^2). Despite this, the higher resolution data distribute wider in Region III respect to the lower resolution data, since the threshold from Region II to III is the same for both resolution (10^3 m^2). This is consistent to what was detected for the study area A. Dealing with the curvature-area distributions showed in *Figure 4.20* and *Figure 4.22*, also in this case the transition from divergent to convergent curvatures correlates well with the hillslope to valley transition of the S-A diagrams. In addition, negative values of curvature are found to remain close to zero in the portion of the plot corresponding to Region II of the S-A relations, and to diminish with increasing drainage area. Again, a progressive decrease in maximum curvature values from the higher to the coarser resolution is detectable.

4.2.3 Comparison between the two study areas: differences among vegetation typologies

In accordance with the results obtained by Tarolli et al. (2006) and Tarolli (2007), also in the case studies located in the two headwater catchments of the Miozza basin, different vegetation classes distribute along the S-A diagram according to their vegetative inclinations. Generally, in both basins, medium to high forest vegetation classes better distribute for higher values of slopes respect to the shrubs and grasslands typologies. This can be related to the mechanical function exerted by the root systems on soil cohesion, which leads woody vegetation to increase slope stability (Bischetti et al., 2005; Shmidt et al., 2001; Wu 1984a, 1984b). Specific slope-area patterns of each vegetation typology for study areas A and B are shown in *Figure 4.23* and *Figure 4.24*; while curvature-area plots for both the basins are displayed in *Figure 4.25* and *Figure 4.26*. For the sake of simplicity in the comparison, all of those graphs refer to the 3 m resolution analysis.

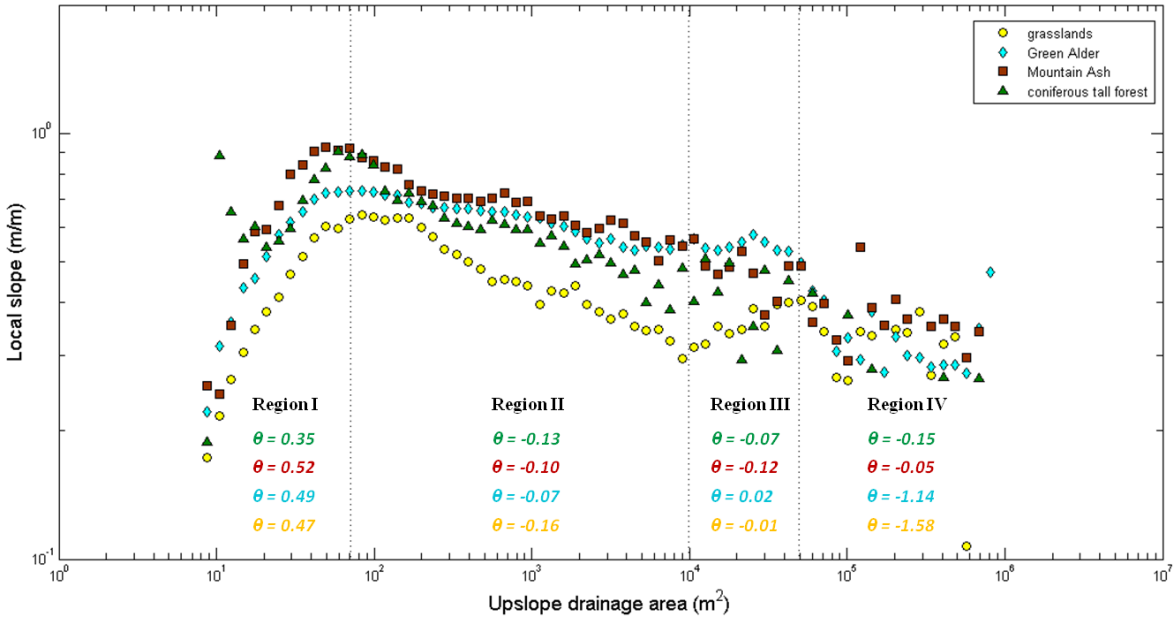

Figure 4.23 - Slope-area plots for the study area A of the Miozza basin at 3 m resolution, relative to each vegetation type. For the four regions detected the concavity index (θ) corresponding to each vegetation type is displayed as well.

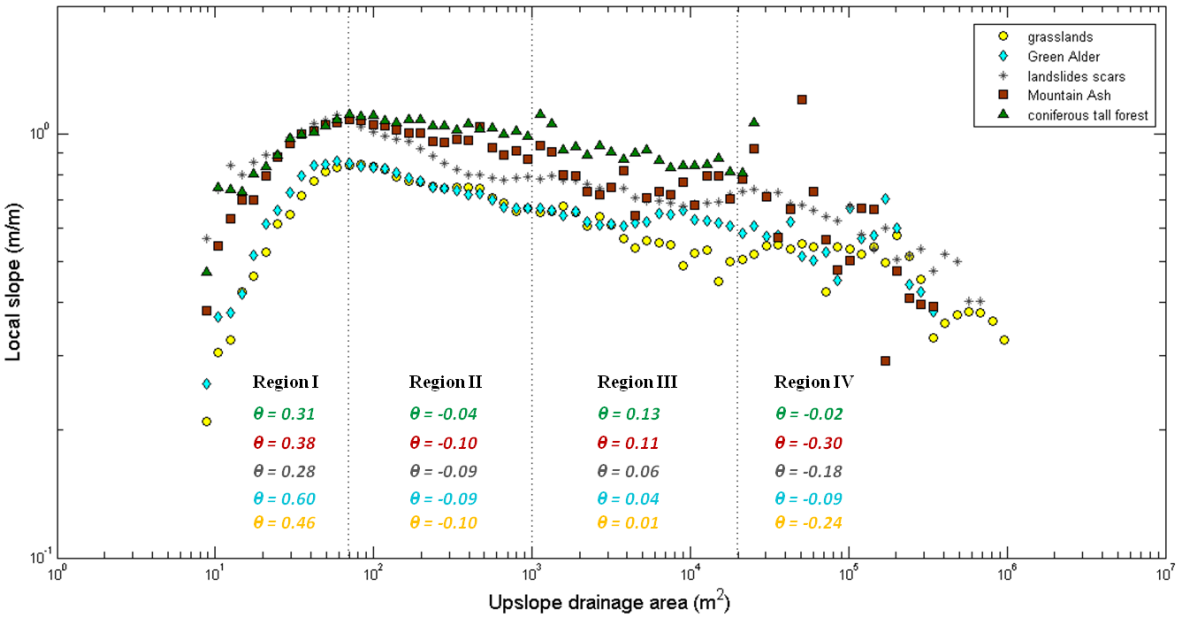

Figure 4.24 - Slope-area plots for the study area B of the Miozza basin at 3 m resolution, relative to each vegetation type. For the four regions detected the concavity index (θ) corresponding to each vegetation type is displayed as well.

Looking at the slope-area diagram of the study area A and also considering the variations in the concavity index (θ) values reported in *Figure 4.23* for each vegetation typology, the class that plots steeper throughout the regions is the one mainly represented by the Mountain Ash (also presenting the highest value of concavity index in Region I, θ=*0.52*), with only an

exception for Region III, where the Green Alder pattern overcomes the Mountain Ash one (exhibiting the only positive θ value for that region). The woody vegetation class of the coniferous forest instead, plots in basin A as steep as the Mountain Ash at the transition from hillslope to valley morphologies, then presents lower values of slope respect to the classes of shrubs and medium forest (respectively Green Alder and Mountain Ash) in Region II and finally reaches even lower values of slope in Regions III and IV. The distribution of this high forest vegetation class is mainly arranged toward low values of drainage area, associated with high slope values. Such distribution for coniferous species can be detected in both basins, even though in the study area B this vegetation type interests steeper slopes in all regions. This behavior can be related to the preferable dry conditions and steep morphologies over which coniferous species such as Norway Spruce and European Larch generally vegetate (Tarolli et al., 2006). Significantly, patterns of the Green Alder vegetation class are similar for both basins. This shrub species generally occupies moderate values of slopes, although it reveals a clear shift toward higher slope values for a given drainage area range which corresponds to the debris flow-landslides dominated area of Region III, where it presents a positive gradient also characterized by the only positive θ value in basin A ($\theta = 0.02$). This sharp change in the Green Alder S-A pattern in Region III that exhibits a sudden increase in slope values with increasing drainagea area, opposed to trends of the other classes that also present uniform negative θ values, can be considered as statistically significant in the identification of a debris flow-subjected area. Hence, this pecularity strongly confirms the correlation, already suggested by Tarolli et al. (2006), between this highly pioneering shrubby species and those areas of the catchments presenting morphological features related to debris-flow or shallow landslides occurrence.

Moreover, for the study area B (*Figure 4.24*), where also the S-A pattern of landslides scars is available, the Green Alder pattern that normally interests lower values of drainage area than the landslide path, shows again an increase in slope values for a given drainage area of about 10^4 m^2 where the patterns of both classes seem to gather to almost overlie to each other. Indeed, Green Alder vegetation class seems to have a quite similar distribution and concavity index value ($\theta=0.04$) respect to the landslide class ($\theta=0.06$), just plotting on lightly lower slope values; thus suggesting an interesting correspondence with the landslide pattern, as it has been already found out by Tarolli et al. (2006). The Mountain Ash vegetation class also presents a similar distribution, but plots on steeper slope values than the Green Alder,

probably due to the higher values of root cohesion presented by the former (Chiaradia and Bischetti, 2007). Respect to the Green Alder's concavity index values reported for regions II and III in basin A, the Mountain Ash presents less dissimilarity; indeed θ for the Green Alder class varies from -0.07 in Region II to 0.02 in Region III, while Mountain Ash θ values change from -0.10 in Region II to -0.12 in Region III. Finally, grasslands distributions are found in both the study areas to correlate well with less steep slopes in all regions, while covering from the lowest to the highest values of upslope area. This is consistent with the ability of grass species to occupy well all the slope gradients, from the convex hillslopes of Region I to the channelized morphologies of Region IV of the S-A diagram. Any particular evidence comes from the concavity index values relative to this vegetation class.

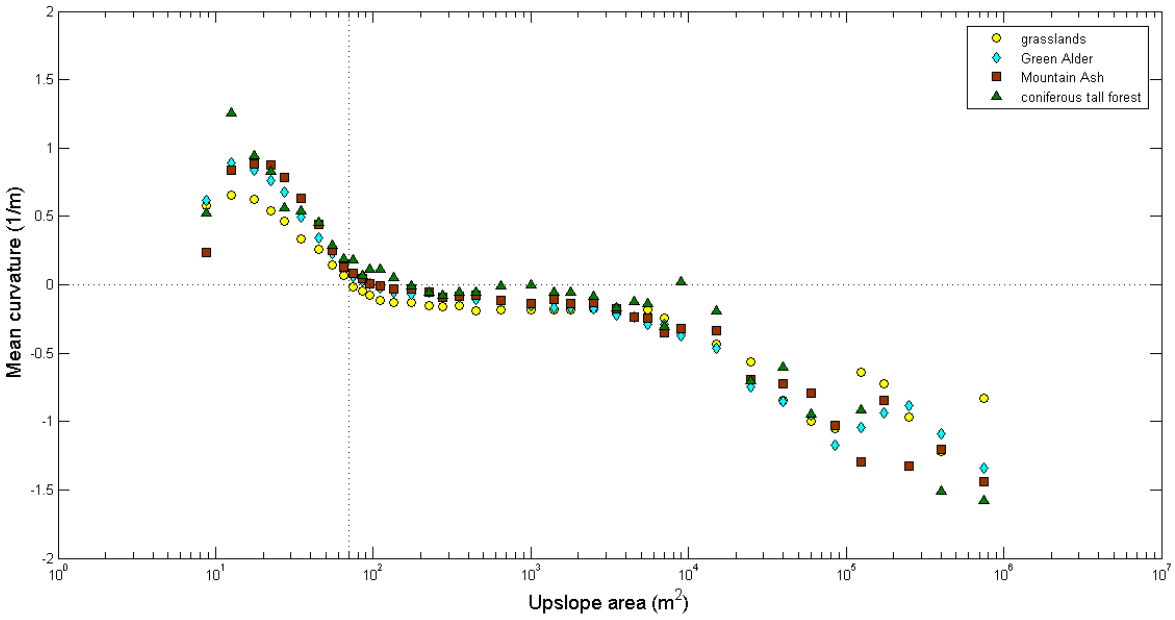

Figure 4.25 - Curvature-area (C-A) relations for the study area A of the Miozza basin at 3 m resolution, relative to each vegetation type.

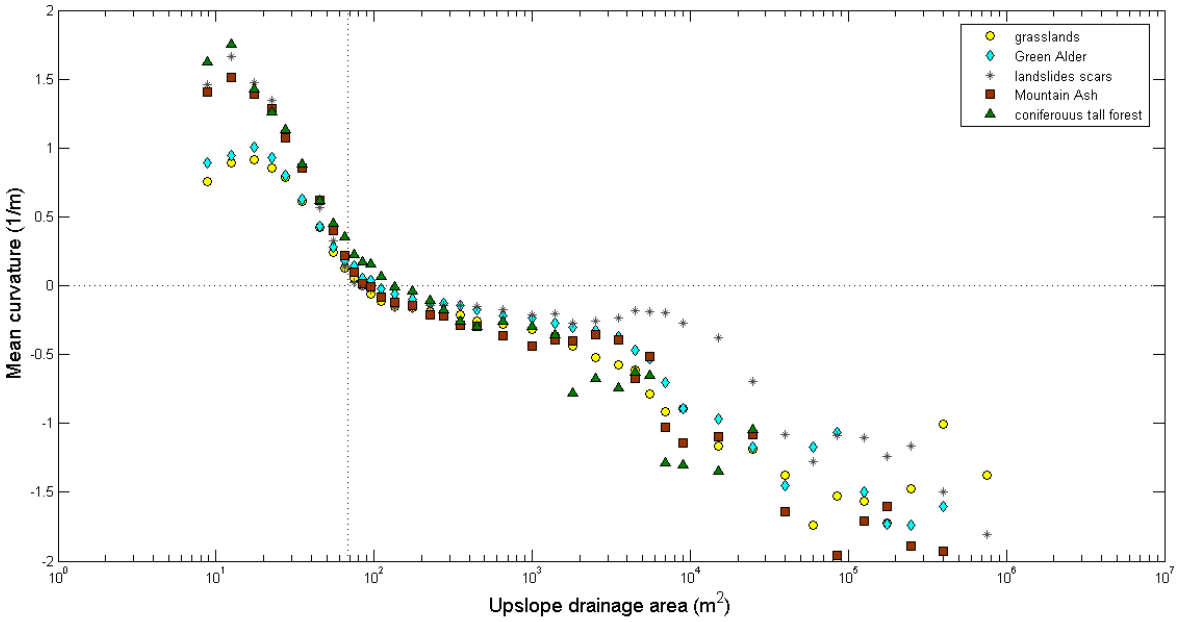

Figure 4.26 - Curvature-area (C-A) relations for the study area B of the Miozza basin at 3 m resolution, relative to each vegetation type.

The landform curvature-upslope area relationships displayed in *Figure 4.25* and *Figure 4.26* strictly reflect the relation between profile morphology and vegetation classes distribution. Actually, higher positive curvature values are associated with a hillslope-divergent morphology presented by woody vegetation such those of the classes "Mountain Ash" and "Coniferous tall forest", while grass and shrubs species appear to be related to lower positive curvature values. Conversely, the valley-convergent morphology beginning after the transition to negative curvature values, presents smoother patterns for the "grasslands" and "Green Alder" vegetation types than the other classes. This trend confirms the results from Yetemen et al. (2010) according to which the classes that distribute over steeper slope values in the S-A plot, present a higher degree of ridge divergence and valley convergence in their C-A distributions.

Further results are presented thanks to the interpretation of the box plots relative to some of the morphometric parameter analyzed. This is shown by the following graphs reported in *Figure 4.27*, *Figure 4.28* and *Figure 4.29*. The figures are structured in order to allow an easy comparison between the two study areas, coherently with the vegetation types characterization.

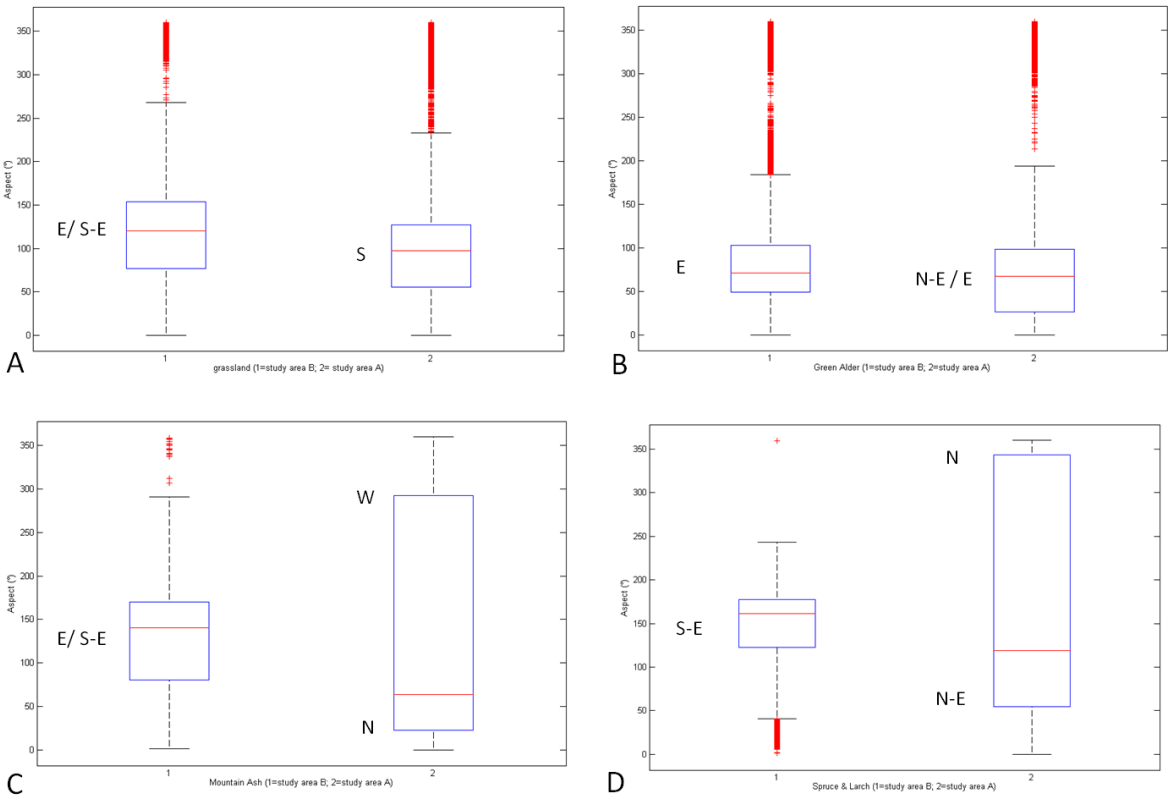

Figure 4.27 - Box plot representation of the aspect parameter at 3 m resolution: A. comparison of the vegetation type "grasslands" between study area A (2) and B (1); B. comparison of the vegetation type "Green Alder" between study area A (2) and B (1); C. comparison of the vegetation type "Mountain Ash" between study area A (2) and B (1); D. comparison of the vegetation type "Spruce & Larch" between study area A (2) and B (1).

From *Figure 4.27* differences in the aspect relative to the two study areas are detectable. Basin A appears to be more oriented toward Northern aspects than basin B, which is instead more oriented toward East, South-East compass directions. Particularly, the vegetation typologies of "Mountain Ash" and "Spruce & Larch" coniferous forest, plotted in *Figure 4.27-C* and *Figure 4.27-D*, show the highest variability in aspect respect to the other classes, especially in basin A.

Furthermore, from the box plot analysis of *Figure 4.28* it is possible to notice a general distribution of the study area A toward lower values of local slope respect to the study area B. This trend results to be true for each vegetation class.

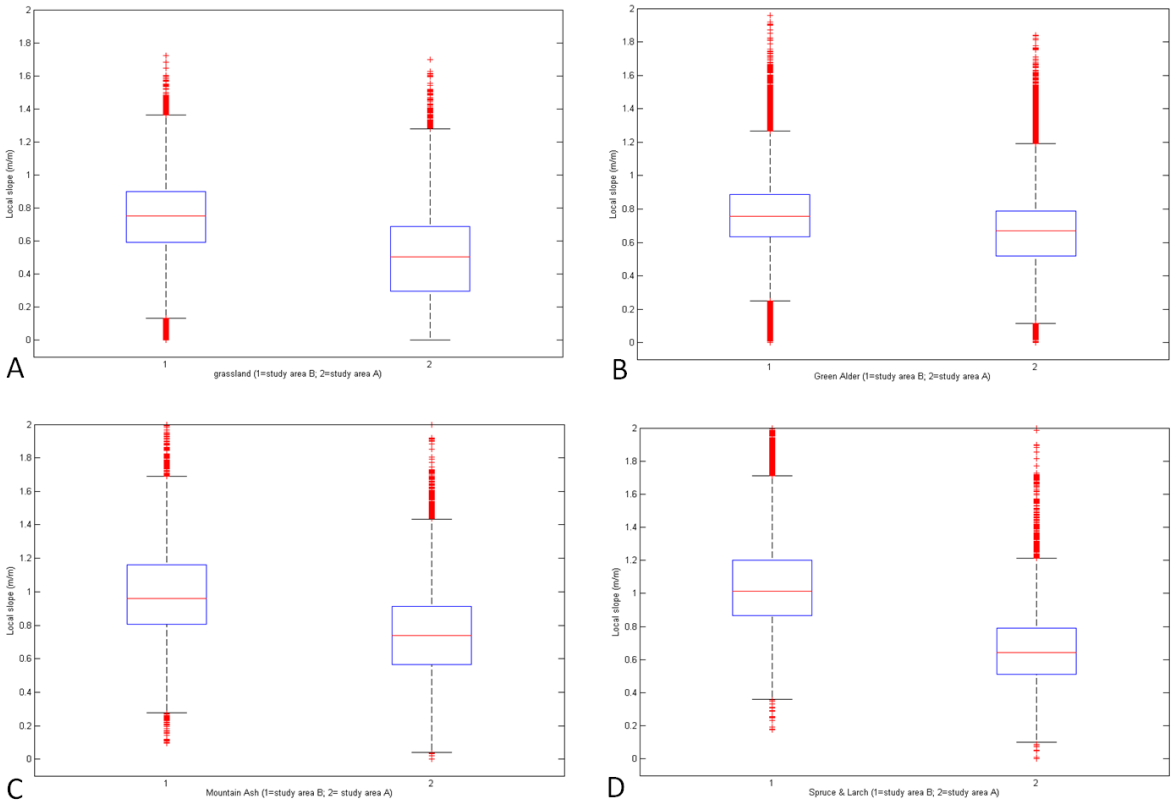

Figure 4.28 - Box plot representation of the local slope parameter at 3 m resolution: A. comparison of the vegetation type "grasslands" between study area A (2) and B (1); B. comparison of the vegetation type "Green Alder" between study area A (2) and B (1); C. comparison of the vegetation type "Mountain Ash" between study area A (2) and B (1); D. comparison of the vegetation type "Spruce & Larch" between study area A (2) and B (1).

The same trend is also confirmed by the values of some statistical parameters reported in *Table 4.3* for the two basins considered as a whole (i.e. computed without a differentiation in types of vegetation).

Table 4.3 - Statistical analysis of the study areas A and B at 3 m resolution, according to their local slope values (m/m).

	Min. value	Max. value	Mean value	Median	St. deviation
Basin A	0	2.2242	0.6348	0.6442	0.2505
Basin B	0	2.4607	0.8341	0.8160	0.2738

Finally, the Topographic Wetness Index characterization of each vegetation type within the study areas can be evaluated by the following series of box plot diagrams. To this regard, *Figure 4.29* shows that the study area A exhibits a general trend of distributions distinctly shift toward higher values of TWI in comparison with the study area B. In further detail, *Figure 4.29-C* and *Figure 4.29-D* reveal a slightly higher TWI values for the distribution of the vegetation types "grasslands" and "Green Alder" in both basins.

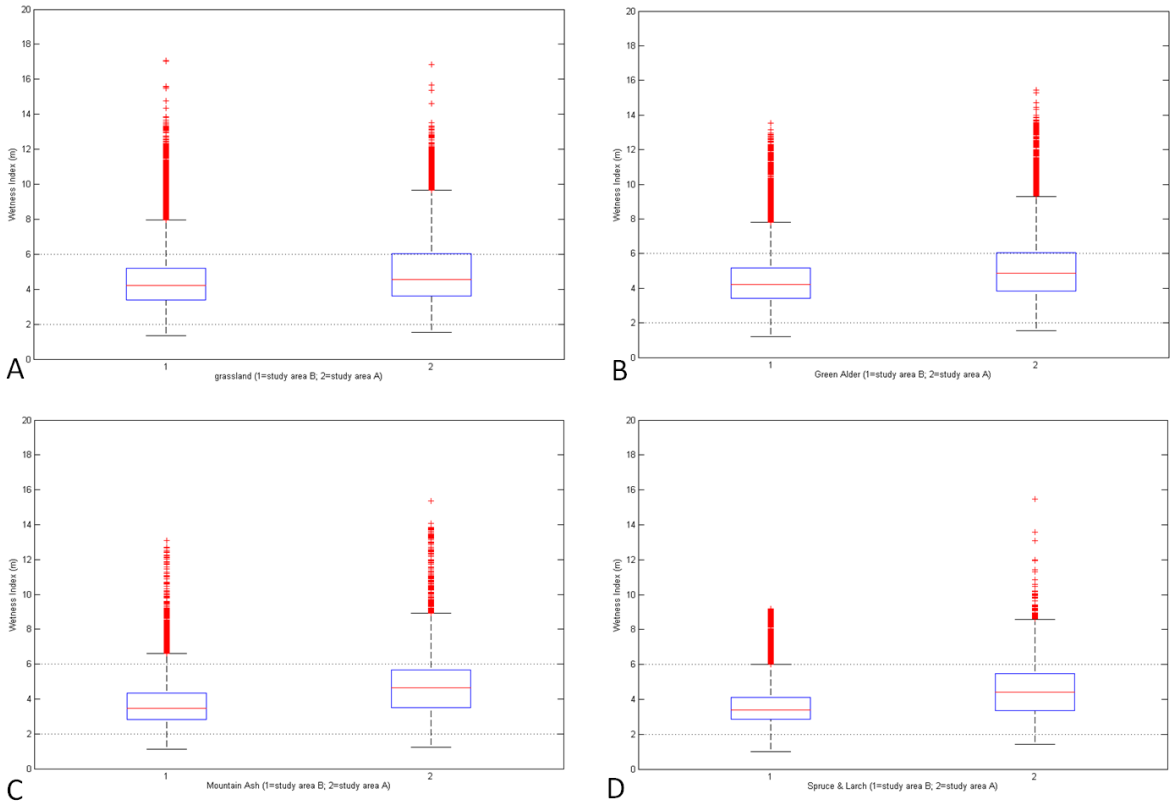

Figure 4.29 - Box plot representation of the Topographic Wetness Index (TWI) parameter at 3 m resolution: A. comparison of the vegetation type "grasslands" between study area A (2) and B (1); B. comparison of the vegetation type "Green Alder" between study area A (2) and B (1); C. comparison of the vegetation type "Mountain Ash" between study area A (2) and B (1); D. comparison of the vegetation type "Spruce & Larch" between study area A (2) and B (1).

These specific observations can be better evaluated by looking at their numerical values, as reported in *Table 4.4*.

Table 4.4 - Statistical analysis of all the vegetation classes and the whole basins A and B at 3 m resolution, according to their topographic wetness index values (m).

	Min. value	Max. value	Mean value	Median	St. Deviation
B grasslands	1.3418	17.0746	4.5145	4.2051	1.6307
A grasslands	1.5400	16.8592	5.0175	4.5568	1.9277
B Green Alder	1.2065	13.5252	4.4554	4.2122	1.4821
A Green Alder	1.5329	15.4410	5.0979	4.8781	1.7119
B Mountain Ash	1.1254	13.0783	3.7568	3.4493	1.3421
A Mountain Ash	1.2267	15.3738	4.7619	4.6384	1.6494
B Spruce & Larch	0.9889	9.1756	3.6194	3.3972	1.1226
A Spruce & Larch	1.4369	15.4643	4.5286	4.4025	1.4484
Whole basin B	0.9889	17.0746	4.4646	4.1654	1.6264
Whole basin A	1.2267	16.8592	4.9833	4.7291	1.7446

As it is possible to notice, the grassland and Green Alder vegetation types present the highest maximum TWI values for both basins. Besides that, the highest median TWI values are presented by Green Alder and the Mountain Ash classes for the study area A.

5 FINAL REMARKS

Focus has been placed on the role of topography in determining distribution patterns of different vegetation typologies, selected through the identification of their specific ecologies, vegetative behaviors, moisture preferences and successional dynamics. The study has been carried out over two distinct study areas, the Mediterranean coastal Cetus basin and the Alpine mountainous Miozza catchment. High resolution LiDAR data and topography derived from conventional cartography have provided the basis upon which develop the analyses of DTMs and topographic attributes, such as aspect, local slope, upslope drainage area, landform curvature and topographic wetness index, also comprehending slope-area and curvature-area relations. Thanks to the available vegetation maps of the study areas it has been possible to relate vegetation types' distribution and surface morphology. In both cases, data analysis allowed the interpretation of the local slope-drainage area diagrams to be consistent with the detection of four regions describing different geomorphic processes, in accordance with the threshold criterion introduced by Ijjaz-Vasquez and Bras (1995) and confirmed by Tarolli and Dalla Fontana (2009). In particular, results for the Cetus basin showed that different vegetation classes specifically distribute along with distinct local slope and upslope area values according to their vegetative attitudes, in such way that it is possible to relate the pattern of each vegetation type to its ecological characteristics. Evidences of this can be found in the distribution of vegetation combined with rocky outcrops that is related to steepest slopes and lower drainage area values; while grasslands and garrigue vegetation types are coupled with lowest values of local slope and moderately high values of upslope area. Moreover, some comparisons between woody vegetation with different thermophilous tolerance can be detected by the slope-area plots, where it is evident a shift of thermoxerophilous vegetation toward values of slope higher than those showed by the mesothermophilous woods in the portion of the diagram which is acknowledged to be related to landslides and debris flow-dominated processes. To some extent, this behavior can be correlated to the higher water stress tolerance that characterizes the vegetation species belonging to the thermoxerophilous class. The analysis relative to the aspects and the topographic wetness index values relative to each vegetation class revealed some differences that could be associated to the vegetative preferences of such classes. In addition, the same investigation also accomplished on two headwater catchments of the Miozza basin, confirms

the results from Tarolli et al. (2006), suggesting a direct link between vegetation typologies and the dominant hillslope erosion processes detected by the slope-area diagram. Particularly significant has been the distribution of woody vegetation on more stable steepest slopes appeared throughout both the study areas, that relates the specific ecology of the main coniferous species of the area (Norway Spruce and European Larch) to the enhanced slope stability that typically characterizes diffusion-dominated portion of the hillslopes. Another relevant association can be detected between the Green Alder and, in a successional dynamic, the Mountain Ash as well, with the landslide scar pattern. The pioneering ability of the Green Alder accounts for a best colonization of the rugged surface subject to landslides events, also due to its seeds dispersal technique and ecological preferences. Though, the Mountain Ash is likely to be considered diffused in successive vegetation stages on the same areas. This specific behavior seems to positively influence the slope stability of the hillslopes.

Finally, the analyzed curvature-area relations uniformly reveal for all the study areas, either the Cetus basin and those located within the Miozza catchment, that vegetation classes that distribute on steepest slopes in the slope-area diagrams, even present the highest degree of ridge divergence and valley convergence in the respective curvature-area plots; thus confirming results by Yetemen et al. (2010).

Investigations from this thesis work provide a further evidence of the relationship between hillslope morphology and vegetation types distribution. Consisting results have been found for both the Mediterranean coastal Cetus basin and the Alpine Miozza catchment, despite of climatic dissimilarities and their different geographic locations. Therefore, this study can be considered as a preliminary analysis of the existing relation between the vegetation characterization of slopes and their dominant erosion processes. According to Marston (2010) suggestions for future directions derived by his research, this work aims to give rise to the development and validation of landscape evolution models that enable feedbacks between biotic and physical processes. Such a mechanistic understanding of these feedbacks is also intimated by Dietrich and Perron (2006) always hoping for the identification of a topographic signature of life, which might be confirmed by the frequency distribution of certain landform properties affected by the biotic activity.

6 REFERENCES

Abrahams A.D., Parsons A.J., Wainwright J. (1994). Resistance to overland flow on semiarid grassland and shrubland hillslopes, Walnut Gulch, southern Arizona. Journal of Hydrology 156 (1–4), 431–446.

Abrahams A.D., Parsons A.J., Wainwright J. (1995). Effects of vegetation change on interrill runoff and erosion, Walnut Gulch, southern Arizona. *Geomorphology 13 (1–4)*, 37–48.

Ackermann F. (1999). Airborne laser scanning – present status and future expectations. ISPRS *Journal of Photogrammetry & Remote Sensing*, 54, 64-67.

Ahlberg J. H., Nilson E.N. (1967). The theory of splines and their applications. Academic Press Inc. Library of Congress Catalog card Number: 66-30115

Arrowsmith J. R., Glenn N., Crosby C. J., Cowgill E. (2008). Current capabilities and community needs for software tools and educational resources for use with LiDAR high resolution topography data. *Arizona State University*.

Band L. E. (1986). Topographic partition of watersheds with digital elevation models. *Water resources research*, 22, 15-24.

Band, L. E., Patterson, P., Nemani, R., Running, S. W. (1993). Forest ecosystem processes at the watershed scale: incorporating hillslope scale, *Agr. Forest Meteorol.*, 63, 93–126.

Barilotti A., Beinat A., Fico B., Sossai E., (2006). Produzione e verifica di DTM da rilievi LiDAR aerei su aree montane ricoperte da foresta. *51° Convegno Nazionale della Società Italiana di Fotogrammetria e Topografia*, Castellaneta Marina 14–16/6, Taranto, Italy, pp.9.

Barling R. D., Moore I. D., Grayson R. B. (1994). A quasi-dynamic wetness index for characterizing the spatial distribution of zones of surface saturation and soil water content. *Water Resources Research*,30, 1029–1044.

Beven K. J. (1987). Towards the use of catchment geomorphology in flood frequency predictions. *Earth Surface Processes Landforms* 12:69-82.

Beven K. J., Wood E. E. (1983). Catchment geography and the dynamics of runoff contributing areas. *Journal of Hydrology* 65:139-158.

Beven, K. J., Kirkby, M. J. (1979). A physically based, variable contributing area model of basin hydrology. *Hydrolological Sciences Bulletin*, 24, 43–69.

Bischetti G.B., Chiaradia E.A., Limonato T., Speziali B., Vitali B., Vullo P., Zocco A. (2005). Root strength and root area ratio of forest species in Lombardy (Northern Italy), Plant and Soil, 278, 11–22, doi: 10.1007/s11104-005-0605-4.

Bogaart, P.W., Troch, P.A. (2006). Curvature distribution within hillslopes and catchments and its effect on the hydrological response. *Hydrology and Eart System Sciences* 10, 925–936.

Braun-Blanquet J. (1932). Plant sociology: the study of plant communities. *McGraw-Hill*, New York.

Briese C. (2010). Extraction of digital terrain models. In Vosselman, G.; Maas, H.G. (eds.) Airborne and terrestrial laser scanning. First ed. *Whittles Publishing*, UK, pp. 135-168.

Burrough P.A., McDonnell R.A. (1998). Principles of Geographic Information Systems. *Oxford University Press*, Oxford (GB).

Butler D.R. (1995). Zoogeomorphology: Animals as Geomorphic Agents. *Cambridge University Press: Cambridge*.

Cain S.A. (1944). Foundations of plant geography. *Harper and Brothers*, New York.

Carter J., Schmid K., Waters K., Betzhold L., Hadley B., Mataosky R., Halleran J. (2012). An introduction to lidar technology, data, and applications. *National Oceanic and Atmospheric Administration (NOAA) Coastal Services Center*. Revised. Charleston, SC: NOAA Coastal Services Center.

Casella V, (2003). Introduzione al laser scanning aereo. In: La tecnica del laserscanning – Teoria ed applicazioni, Crosilla, F. e Galletto, R. , *CISM, Udine,* 1-37.

Cavalli, M., Tarolli, P., Marchi, L., Dalla Fontana, G. (2008). The effectiveness of airborne LiDAR data in the recognition of channel-bed morphology. Catena, 73(3), 249-260.

Chiaradia E.A., Bischetti G.B. (2007). Root cohesion analysis of Green alder and Mountain ash in the Carnia Region, technical note on field surveys and laboratory analysis carried out on spring 2007, *University of Milan*.

Chirico G.B., Western A.W., Grayson R.B., Blöschl G. (2005). On the definition of the flow width for calculating specific catchment area patterns from gridded elevation data. Hydrological Processes 19, 2539–2556

Clements F.E. (1928). Plant succession and indicators. *H.W. Wilson*, New York.

Collins D.B.G., Bras R.L., Tucker G.E. (2004). Modelling the effects of vegetation erosion coupling on landscape evolution. *Journal of Geophysical Research 109*, doi:10.1029/2002JF000028.

Corenblit D., Gurnell A.M., Steiger J., Tabacchi E. (2008). Reciprocal adjustments between landforms and living organisms: extended geomorphic evolutionary insights. *Catena 73*, 261-273.

Corenblit D., Steiger J. (2009). Vegetation as a major conductor of geomorphic changes on the Earth surface: toward evolutionary geomorphology. *Earth surface processes and landforms*, 34, 841-896.

Costa-Cabral, M., Burges S. J. (1994). Digital Elevation Model Networks (DEMON): A Model of Flow Over Hillslopes for Computation of Contributing and Dispersal Areas. *Water Resources Research*, 30(6): 1681-1692.

Cracknell A. P., Ladson W.B. Hayes (1991). Introduction to remote sensing. *Taylor & Francis Group*.

D'Argenio, B., Ferranti, L., Marsella, E., Pappone, G., and Sacchi, M., (1993). From the lost Lagonegro Basin to the present Tyrrhenian: The southern Apennines between compression and extension: Workshop of International Lithosphere Program Task Force "Origin of Sedimentary Basins," 4th, Field Trip Guide Book, 134 p.

Dietrich W. E., Dunne T. (1993). The channel head. *Channel Network Hydrology.* Edited by K. Beven and M. J. Kirkby, pp. 179-219, John Wiley, New York.

Dietrich W. E., Perron J. T. (2006). Topographic signature of life. *Nature.* 439, 411-418.

Dietrich W. E., Wilson C. J., Reneau S. L. (1986). Hollows, colluvium and landslides in soil-mantled landscapes. in *Hillslope Processes* edited by A. Abrahams, pp. 361– 388, Allen and Unwin, St Leonards, NSW,Australia.

Dietrich W.E., Bellugi D.G., Sklar L.S., Stock J.D., Heimsath A.M., Roering J.J. (2003). Geomorphic transport laws for predicting the form and dynamics. In: Wilcock, P., Iverson, R. (Eds.), *Prediction in Geomorphology*. AGU, Washington, D.C, pp. 103–132.

El-Sheimy N., Valeo C., Habib A. (2005). Digital terrain modeling: acquisition, manipulation, and application. *Boston and London: Artech House*.

Evans, I.S. (1979). An integrated system of terrain analysis and slope mapping. Final report on grant DA-ERO-591-73-G0040, University of Durham, England.

Freeman, T. G. (1991), Calculating Catchment Area with Divergent Flow Based on a Regular Grid, *Computers & Geosciences*, 17(3): 413-422.

from high resolution topography using wavelets. *Geophysical Research Letters*. 34, L23S04.

Gabet E.J., Reichman O.J., Seabloom E.W. (2003). The effects of bioturbation on soil processes and sediment transport. *Annual Review of Earth and Planetary Sciences 31*, 249–273.

Gallant JC, Wilson JP. (2000). Primary Topographic Attributes. In *Terrain Analysis: Principles and Applications*, Wilson JP, Gallant J (eds). New York: John Wiley & Sons; 51–85.

Gerten D., Schaphoff S., Haberlandt U., Lucht W., Sitch S. (2004). Terrestrial vegetation and water balance—hydrological evaluation of a dynamic global vegetation model. *Journal of Hydrology*, Volume 286, Issues 1–4, 30 January 2004, Pages 249-270, ISSN 0022-1694, 10.1016/j.jhydrol.2003.09.029.

Godone D., Garnero G. (2013). The role of morphometric parameters in Digital Terrain Models interpolation accuracy: a case study. *European Journal of Remote Sensing*, 46: 198-214. doi: http://dx.doi.org/10.5721/10.5721/EuJRS20134611.

Greenway D.R. (1987). Vegetation and slope stability. In: Anderson, M.G., Richards, K.S. (Eds.), Slope Stability, *Geotechnical Engineering and Geomorphology*. Wiley, Chichester, UK, pp. 187–230.

Gutiérrez-Jurado H. A., Vivoni E. R., Istanbulluoglu E., Bras R. L. (2007). Ecohydrological response to a geomorphically significant flood event in a semiarid catchment with contrasting ecosystems. *Geophysical Research Letters, 34*, L24S25, doi:10.1029/2007GL030994.

Habib, A., Ghanma, M., Morgan, M., Al-Ruzouq R. (2005). Photogrammetric and LiDAR data registration using linear features. *Photogrammetric Engineering and Remote Sensing* 71(6), 699- 707.

Hack J.T., Goodlet J.C. (1960). Geomorphology and forest ecology of a mountain region in the Central Appalacians. *U.S. Geological Survey Professional Paper* 347.4

Haneberg W.C. (1991). Observation and analysis of pore water pressure fluctuations in a thin colluvium landslide complex near Cincinnati, Ohio. *Engineering Geology 31*,159–184.

Harden C.P. (2006). Human impacts on headwater fluvial systems in the northern and central Andes. *Geomorphology 79 (3–4)*, 249–263.

Hengl T., Heuvelink G. B. M., Stein A. (2003). Comparison of kriging with external drift and regression-kriging. Technical note, ITC, Available on-line at http://www.itc.nl/library/Academic_output/

Hilley G. E., Strecker M. R. (2004). Steady-state erosion of critical Coulomb wedges with applications to Taiwan and the Himalaya. *Journal of Geophysical Research 109*, B01411, doi:10.1029/2002JB002284.

Horn B.K.P. (1981). Hill shading and the reflectance map. Proceedings of the IEEE, 69(1), 14-47.

Howard A. D. (1994). A detachment-limited model of drainage basin evolution. *Water Resources Research 30*, 2261–-2285.

Howard A. D. (1997). Badland morphology and evolution: Interpretation using a simulation model, Earth Surace Processes Landforms, 22, 211–227.

Howard A. D. (1999). Incised River Channels (eds Darby, S. E. & Simons, A.) 277–299, *Wiley, New York.*

Hu W., Enving L., Li G. Y., Zhong Z. H. (2008). A metamodel optimization methodology based on multi-level fuzzy clustering space reduction strategy and its applications. *Computers & Industrial Engineering*. Volume 55, Issue 2, Pages 503‑532.

Ijjasz-Vasquez E., Bras R. L. (1995). Scaling regimes of local slope versus contributing area in digital elevation models. *Geomorphology*. 12. 299-311.

Isaaks E.H., Srivastava R.M. (1989). Introduction to applied geostatistics. *Oxford press.*

Istanbulluoglu E., Bras R. L. (2005). Vegetation-modulated landscape evolution: Effects of vegetation on landscape processes, drainage density, and topography. *Journal of Geophisical Research.* Vol. 110, F02010.

Istanbulluoglu E., Tarboton D. G., Pack R. T., Luce C. (2004). Modeling of the interactions between forest vegetation, disturbances and sediment yields, *Journal of Geophysical Research, 109,* F01009, doi:10.1029/2003JF000041.

Istanbulluoglu, E., Yetemen, O., Vivoni, E.R., Gutiérrez-Jurado, H.A., Bras, R.L. (2008). Ecogeomorphic implications of hillslope aspect: Inferences fromanalysis of landscape morphology in central New Mexico. *Geophysical Research Letters* 35, L14403.

Jantsch E. (1980). The Self-Organizing Universe, Pergamon, Oxford.

Jenson S, Domingue J. (1988). Extracting topographic structure from digital elevation data. Photogrammetric Engineering and Remote Sensing 54(11): 1593–1600.

Jenson, S. K. (1991), Applications of Hydrologic Information Automatically Extracted From Digital Elevation Models. *Hydrological Processes*, 5(1): 31-44.

Jenson, S. K. and J. O. Domingue (1988), Extracting Topographic Structure from Digital Elevation Data for Geographic Information System Analysis. *Photogrammetric Engineering and Remote Sensing*, 54(11): 1593-1600.

Karel W.,Kraus K. (2006). Quality parameters of digital terrain models. In Semina on Autmated Quality Control of Digital Terrain Models, *EuroSDR Seminar*, 18-19 August 2005, Aalborg, Denmark.

Keim R.F., Skaugset A.R., (2003). Modeling effects of forest canopies on slope stability. *Hydrological Processes 17*, 1457–1467.

Kirkby M. (1995). Modelling the links between vegetation and landforms. *Geomorphology*, 13. 319-335.

Kirkby M.J. (1971). Hillslope process–response models based on the continuity equation. In: Brunsden, D. (Ed.), Slopes, Form and Process. Special Publication 3. *Institute of British Geographers*, London, pp. 15–30.

Kleidon A., Fraedrich K., Heimann M. (2000). A green planet cersus a desert world: estimating the maximum effect of vegetation on the land surface climate. *Climatic Change 44*, 471-493.

Klipp E., Nayegandhi A. (2007). USGS Hosts Airborne-Lidar Technology and Applications Workshop in Louisiana. *Sound Waves* monthly newsletter, Coastal and Marine Research News from across the USGS.

Kruckerberg A.R. (2002). Geology and plant life: the effects of landforms and rock types on plants. *University of Washington Press*, Seattle.

Lammers, R. B., Band. L.E. (1990). Automating object representation of drainage basins. *Computers & Geosciences*. 16(6): 787-810.

Lancaster S. T. (1998). A nonlinear river meandering model and its incorporation in a landscape evolution model, Ph.D. thesis, *Mass. Inst. Of Technol.*, Cambridge.

Langbein W. B., Schumm S.A. (1958). Yield of sediment in relation to mean annual precipitation. *Eos Trans AGU, 39*, 1076– 1084.

Lashermes B., Foufoula-Georgiou E., Dietrich W.E. (2007). Channel network extraction

Lea, N. L., (1992). An aspect driven kinematic routing algorithm. in Overland Flow: Hydraulics and Erosion Mechanics, Edited by A. J. Parsons and A. D. Abrahams, Chapman & Hall, New York.

Li J., Heap A. D. (2008). A review of spatial interpolation methods for environmental scientists. Geoscience Australia, Department of Resources, Energy and Tourism; Minister for Resources and Energy.

Liu, X. (2008). Airborne LiDAR for DEM generation: some critical issues. *Progress in Physical Geography: an international review of geographical work in the natural and environmental sciences,* 32 (1). pp. 31-49. ISSN 0309-1333.

Mark D. M. (1988). Network models in geomorphology. *Modelling Geomorphological Systems*, edited by M. G. Anderson, John Wiley, New York, 1988.

Marston R.A. (2010). Geomorphology and vegetation on hillslopes: Interactions, dependencies, and feedback loops. *Geomorphology*, 116, 206-217.

Marston R.A., Dolan L.S., (1999). Effectiveness of sediment control structures relative to spatial patterns of soil loss in an arid upland watershed. *Geomorphology 31 (1)*,313–324.

Martz, L. W., Garbrecht J. (1992), Numerical Definition of Drainage Network and Subcatchment Areas From Digital Elevation Models. *Computers and Geosciences*. 18(6): 747-761.

Matheron G. (1960). Krigeage d'un Panneau Rectangulaire par sa Peripherie. *Note geostatistique*, 28, CG. Ecole des Mines de Paris, Paris.

Moglen G. E., Eltahir E. A. B., Bras R. L. (1998). On the sensitivity of drainage density to climate change. *Water Resources Research, 34*, 855–862.

Montgomery D. R. (2001). Slope distributions, threshold hillslopes, and steady-state topography. *American Journal of Sciences*, Vol. 301, p. 432-454.

Montgomery D. R., Dietrich W. E. (1992). Channel initiation and the problem of landscape scale. *Science*. 255, p. 826-830.

Montgomery D. R., Foufoula-Georgiou E. (1993). Channel network source representation using digital elevation models. *Water Resources Research*. Vol. 29, No.12, p. 3925-3934.

Montgomery D.R., Dietrich W.E. (1994). Landscape dissection and drainage area-slope thresholds. *Process Models and Theoretical Geomorphology*, edited by M. J. Kirkby, pp. 221-246, John Wiley, New York, 1994.

Moore I.D., Grayson R.B., Ladson A.R. (1991). Digital Terrain Modeling: a review of hydrological, geomorphological, and biological applications. *Hydrological Processes* 5(1): 3–30.

Moore, I. D., Norton, T. W., Williams, J. E. (1993). Modelling environmental heterogeneity in forested landscapes, *Journal of Hydrology*., 150, 717–747.

Moore, I., Gessler, P., Nielsen, G., & Peterson, G. (1993). Soil attribute prediction using terrain analysis. *Soil Science Society of America Journal*, 57, 443–452.

Morris, D. G., Heerdegen R.G. (1988), Automatically Drained Catchment Boundries and Channel Netowrks and their Hydrological Applications. *Geomophology*, 1: 131-141.

Mukai, T., Nakamura, A.M., Sakai, T. (2006). Asteroidal surface studies by laboratory light scattering and LIDAR on HAYABUSA. *Advances in Space Research* 37(1), 138-141.

O'Callaghan JF, Mark DM. (1984). The extraction of drainage networks from digital elevation data. Computer Vision, Graphics and ImageProcessing 28: 323–344.

O'Loughlin, E. M. (1986). Prediction of surface saturation zones in natural catchments by topographic analysis. *Water Resources Research*, 22, 794–804.

Parsons A.J., Abrahams A.D., Simanton J.R., (1992). Microtopography and soil-surface materials on semi-arid piedmont hillslopes, southern Arizona. *Journal of Arid Environments 22*, 107–115.

Parsons, A.J., Abrahams, A.D.,Wainwright, J., (1996). Responses of interrill runoff and erosion rates to vegetation change in southern Arizona. *Geomorphology, 14 (4),* 311–317.

Pfeifer, N., Briese, C. (2007). Geometrical aspects of airborne laser scanning and terrestrial laser scanning. *International Archives of Photogrammetry, Remote Sensing and Spatial Information Sciences* 36 (part 3/W52), 311-319.

Phillips J.D. (2006). Evolutionary geomorphology: thresholds and nonlinearity in landform response to environmental change. *Hydrology and Earth System Science*, 10: 731-742.

Pignatti G., Terenzuolo P.G., Varese P., Semerari P., Lombardi V.N. (2004). Criteri per la definizione di tipi forestali nei boschi dell'Appennino meridionale. Forest@ 1 (2): 112-127. [online] URL: http://www.sisef.it/

Pirotti F., Guarnieri A., Vettore A. (2013). State of the Art of Ground and Aerial Laser Scanning Technologies for High-Resolution Topography of the Earth Surface. *European Journal of Remote Sensing*, 46: 66-78, doi: http://dx.doi.org/10.5721/EuJRS20134605

Pirotti F., Tarolli P. (2010). Suitability of LiDAR point density and derived landform curvature maps for channel network extraction. *Hydrological processes*. 24,, 1187–1197

Poorter H., Nagel O. (2000) The role of biomass allocation in the growth response of plants to different levels of light, CO2, nutrients and water: a quantitative review. *Australian Journal of Plant Physiology* 27 , 1191–1191.

Prosser I. P., Dietrich W. E. (1995). Field experiments on erosion by overland flow and their implication for a digital terrain model of channel initiation. *Water Resources Research, 31*, 2867–2876.

Quinn, P., K. Beven, P. Chevallier and O. Planchon (1991), The Prediction of Hillslope Flow Paths for Distributed Hydrological Modeling Using Digital Terrain Models. *Hydrological Processes*,5: 59-80.

Ramirez J.R. (2006). A new approach to relief representation. *Surveying and Land Information Science* 66(1), 19-25.

Reinhardt L., Jerolmack D., Cardinale B.J., Vanackler V., Wright J. (2010) Dynamic interactions of life and its landscape: feedbacks at the interface of geomorphology and ecology. *Earth surface processes and landforms*. 35, 78-101.

Reutebuch, S.E., Andersen, H.E., McGaughey, R. J. (2005). Light detection and ranging (LIDAR): an emerging tool for multiple resource inventory. *Journal of Forestry* 103(6), 286-292.

Riestenberg M.M., (1994). Anchoring of thin alluvium on hillslopes in Cincinnati by roots of sugar maple and white ash. *U.S. Geological Survey Bulletin*, 2059E.

Roering J.J., Almond P., Tonkin P., McKean J. (2004). Constraining climatic controls on hillslope dynamics using a coupled model for the transport of soil and tracers: Application to loess-mantled hillslopes, South Island, New Zealand. *Journal of Geophysical Research 109*, doi:10.1029/2003JF000034.

Roering J.J., Kevin M.S., Stock J.D., Dietrich W.E., Montgomery D.R. (2003). Shallow landsliding, root reinforcement, and the spatial distribution of trees in the Oregon Coast Range. *Canadian Geotechnical Journal 40 (2)*, 237–253.

Roering J.J., Kirchner J.W., Dietrich W.E. (1999). Evidence for nonlinear diffusive sediment transport on hillslopes and implications for landscape morphology. *Water Resources Research, 35*, 853– 887.

Roering J.J., Kirchner J.W., Sklar L.S., Dietrich W.E. (2001). Hillslope evolution by nonlinear creep and landsliding: An experimental study. *Geology, 29*, 143– 146.

Roering J.J., Schmidt K.M., Stock J.D., Dietrich W.E., Montgomery D.R., (2003). Shallow landsliding, root reinforcement, and the spatial distribution of trees in the Oregon Coast Range. *Canadian Geotechnical Journal*, 2003, 40(2): 237-253, 10.1139/t02-113 .

Schmidt K.M., Roering J.J., Stock J.D., Dietrich W.E., Montgomery D.R., Schaub T. (2001). The variability of root cohesion as an influence on shallow landslide susceptibility in the Oregon Coast Range. C*anadian Geotechnical Journal 38*, 995–1024.

Sheng, Y., Gong, P., Biging, G. S. (2003). Orthoimage production for forested areas from large-scale aerial photographs. *Photogrammetric Engineering and Remote Sensing* 69(3), 259-266.

Shepard D. (1968). A two-dimensional interpolation function for irregularly-spaced data. *Proceedings of the 1968 ACM National Conference*. pp. 517–524. doi:10.1145/800186.810616.

Sibson R. (1981). A brief description of natural neighbor interpolation (Chapter 2). in V. Barnett: Interpreting Multivariate Data. Chichester: John Wiley, pp. 21-36.

Sidle R.C., Ochiai H., (2006). Landslides: processes, prediction, and land use. Water Resources Monograph 18. *American Geophysical Union*, Washington, DC.

Smith T. R., Bretherton, F. P. (1972). Stability and the conservation of mass in drainage basin evolution. *Water Resource Research*. 8, 1506–-1529.

Stavi I., Lavee H., Ungar E.D., Sarah P. (2009). Ecogeomorphic feedbacks in semiaridrangelands: a review. *Pedosphere 19 (2)*, 217–229.

Stephenson N.L. (1990). Climatic Control of Vegetation Distribution: The Role of the Water Balance. *The American Naturalist Vol. 135*, No. 5, pp. 649-670 Published by: The University of Chicago Press.

Stock J., Dietrich W. E. (2003). Valley incision debris flows: Evidence of a topographic signature. *Water Resources Research*. Vol. 39, No. 4, 1089.

Tarboton D.G. (1997). A new method for the determination of flow directions and contributing areas in grid digital elevation models. Water Resources Research, 33, pp. 309–319.

Tarboton D.G., Bras R.L., Rodriguez-Iturbe I. (1991), On the Extraction of Channel Networks from Digital Elevation Data. *Hydrologic Processes.* 5(1): 81-100.

Tarboton, D. G. (1989), The analysis of river basins and channel networks using digital terrain data. Sc.D. Thesis, Department of Civil Engineering, M.I.T., Cambridge, MA

Tarboton, D. G., Bras R.L., Rodriguez-Iturbe I. (1991), On the Extraction of Channel Networks from Digital Elevation Data. *Hydrologic Processes.* 5(1): 81-100.

Tarboton, D. G., Bras R.L., Rodriguez-Iturbe I. (1992), A Physical Basis for Drainage Density. *Geomorphology.* 5(1/2): 59-76.

Tarolli P. (2007). Green Alder pattern in Relation to Slope-Area Scaling Regimes of a Headwater Basin in the Eastern Italian Alps. *Eos Trans. AGU, 88(52)*, Fall Meet. Suppl., Abstract H51H-0877.

Tarolli P., Dalla Fontana G. (2009). Hillslope-to-valley transition morphology: new opportunities from high resolution DTMs. *Geomorphology* 113*:* 47–56. DOI:10.1016/j.geomorph. 2009.02.006.

Tarolli P., Arrowsmith J.R., Vivoni E.R. (2009). Understanding earth surface processes from remotely sensed digital terrain models, *Geomorphology*, 113, 1-3, ISSN: 0169-555X.

Tarolli P., **Cavalli M.** (2013). Introduction to the special issue: "High resolution topography, quantitative analysis and geomorphological mapping", *European Journal of Remote Sensing*, 46, 60-64, ISSN: 2279-7254.

Tarolli P., Istanbulluoglu E., Dalla Fontana G. (2006). Linking the topography signature of LiDAR-derived vegetation types and geomorphic processes as preliminary steps in integrating landscape evolution with vegetation dynamics. *Eos Trans. AGU*, 87 (52), Fall Meet. Suppl., Abstract H13A-1349.

Tarolli, P., Tarboton D. G. (2006). A new method for determination of most likely landslide initiation points and the evaluation of digital terrain model scale in terrain stability mapping. *Hydrological Earth System Science,* 10: 663-677, www.hydrol-earth-syst-sci.net/10/663/2006/

Tarolli, P., Tarboton D. G. (2006). A new method for determination of most likely landslide initiation points and the evaluation of digital terrain model scale in terrain stability mapping. *Hydrological Earth System Science,* 10: 663-677.

Tucker G. E., Bras R. L. (1998). Hillslope processes, drainage density, and landscape morphology. *Water Resources Research 34*, 2751–2764.

Tucker G. E., Bras R. L. (1999). Dynamics of vegetation and runoff erosion, in A 3D Computer Simulation Model of Drainage Basin and Floodplain Evolution: Theory and Applications, technical report, *U.S. Army Corps of Eng. Construct. Eng. Res. Lab.*, Champaign, Ill.

Tucker G. E., Bras R. L. (2000). A stochastic approach to modeling the role of rainfall variability in drainage basin evolution, *Water Resources Research, 36*, 1953–1964.

Tucker G. E., Lancaster S. T., Gasparini N. M., Bras R. L., Rybarczyk S. M. (2001a). An object-oriented framework for distributed hydrologic and geomorphic modeling using triangular irregular networks, *Computer Geosciences*, 27, 959– 973.

Tucker G.E., Lancaster S., Gasparini N., Bras R. (2001b). The Channel-Hillslope integrated Landscape Development Model (CHILD), in Landscape Erosion and Evolution

Modeling, edited by R. S. Harmon and W. W. Dow III, pp. 349– 384, Kluwer Acad., Norwell, Mass.

Venturini C. (2001). CARTA GEOLOGICA DELLE ALPI CARNICHE, Scala 1:25.000. Coordinamento Scientifico e redazione: Corrado Venturini, SELCA , Firenze, 2001.

Vico G., Porporato A. (2009), Probabilistic description of topographic slope and aspect. *Journal of geophisical research*, vol. 114, F01011, doi:10.1029/2008JF001038, 2009

Wainwright J., Parsons A.J., Abrahams A.D. (2000). Plot-scale studies of vegetation, overland flow and erosion interactions: case studies from Arizona and New Mexico. *Hydrological Processes* 14, 2921–2943.

Wallis, C., D. Watson, D. G. Tarboton and R. Wallace (2009), Parallel Flow-Direction and Contributing Area Calculation for Hydrology Analysis in Digital Elevation Models. *Submitted to PDPTA'09, The 2009 International Conference on Parallel and Distributed Processing Techniques and Applications*, Las Vegas, Nevada, USA, July 13-16.

Walsh R.P.D., Voight P.J. (1977). Vegetation litter: an underestimated variable in hydrology and geomorphology. *Journal of Biogeomorphology* 4 (3), 253–274.

Watkins, D. (2005). LiDAR Types and Uses: with a Case Study in Forestry. *State College, PA, USA: Department of Geography, Pennsylvania State University*.

Webster R., Oliver M. A. (2001). Geostatistics for environmental science. *John Wiley and Sons, LTD*. Toronto, Canada, 271 p.

Webster, T.L., Dias, G. (2006). An automated GIS procedure for comparing GPS and proximal LiDAR elevations. *Computers & Geosciences* 32(6), 713-726.

Wehr, A., Lohr, U. (1999). Airborne laser scanning - an introduction and overview. ISPRS *Journal of Photogrammetry and Remote Sensing* 54(4), 68-82.

Weitkamp, C. (2005). LiDAR: Introduction. In Fujii, T. and Fukuchi, T.; editors, *Laser Remote Sensing*, Boca Raton, London, New York and Singapore: Taylor & Francis, 1-36.

Whipple K. X., Meade B. J. (2004). Controls on the strength of coupling among climate, erosion, and deformation in two-sided, frictional orogenic wedges at steady state. *Journal of Geophysical Research 109*, F01011, doi:10.1029/2003JF000019.

White, J. D. and Running, S. W. (1994). Testing scale-dependent assumptions in regional cosystem simulations, *J. Veg. Sci.*, 5, 687–702.

Willett S. D. (1999). Orography and orogeny: The effects of erosion on the structure of mountain belts. Journal of Geophysical Research 104, 28957-28981.

Willgoose G.R., (1994). A statistic for testing the elevation characteristics of landscape simulation models. *Journal of Geophysical Research*. 99, 13, 987–13, 996.

Willgoose G.R., Bras R.L., Rodríguez-Iturbe I. (1991). A physically based coupled network growth and hillslope evolution model, 1, Theory. *Water Resources Research 27*, 1671–1684.

Wilson L. (1973). Variations in mean annual sediment yield as a function of mean annual precipitation. *American Journal of Science*. 273, 335-349.

Wolock, D. M., G. M. Hornberger, and T. J. Musgrove. (1990). Topographic effects on flow path and surface-water chemistry of the Llyn-Brianne catchments in Wales. *Journal of Hydrology* 115:243-259.

Wolock, D. M., G. M. Hornberger, K. J. Beven, and W. G. Campbell. (1989). The relationship of catchment topography and soil hydraulic characteristics to lake alkalinity in the northeastern United-States. *Water Resources Research* 25:829-837.

Wood JD. (1996). The geomorphological characterisation of digital elevation models. PhD Thesis. *University of Leicester, UK*. http://www.soi.city.ac.uk/ jwo/phd.

Wu T.H. (1984a). Effect of vegetation on slope stability. In Soil Reinforcement and Moisture Effects on Stability, Transportation Research Record 965, Transportation Research Board, Washington, USA, 37–46 pp..

Wu T.H. (1984b). Soil movement on permafrost slopes near Fairbanks, Alaska, *Can. Geotech. J.*, *21*, 699–709.

Wu T.H., McOmber R.M., Erb R.T., Beal P.E. (1988). Study of soil-root interaction. *Journal of Geotechnical Engineering* 114 (2), 1351–1375.

Yetemen O., Istanbulluoglu E., Vivoni E.R. (2010). The implications of geology, soils, and vegetation on landscape morphology: Inferences from semi-arid basins with complex vegetation patterns in Central New Mexico, USA. *Geomorphology, 116*, 246-263.

Zhang W., Montgomery D.R. (1994). Digital elevation model grid size, landscape representation and hydrologic simulations. *Water Resources Research*, 30, 1019-28.

Ziadat F.M. (2007). Effect of Contour Intervals and Grid Cell Size on the Accuracy of DEMs and Slop Derivatives. *Transactions in GIS* 11(1), 67-81.

Zinko U., Seibert J., Dynesius M. and Nilsson C. (2005). Plant species numbers predicted by a topography based groundwater-flow index. *Ecosystems*, 8, 430–441.

Acknowledgements

I would like to particularly thank Prof. Paolo Tarolli for having led me to this significant achievement, always sharing his knowledges with all of us students and arousing our curiosity about current scientific issues. I would have never managed to arrange this theses work without his guide. I also offer thanks to Prof.ssa Maria Cristina Rulli for her kind collaboration. Moreover, a special thank goes to Prof. Tarolli's assistant and also my dear friend, Dott. Massimo Prosdocimi, whose support comforted me in the worst moments. I'm really pleased to affirm that we have shared the hardest times and the most hilarious ones as well for the last two years and I hope we'll keep on trust each other like we have done so far. One more thank is addressed to my parents Patrizia and Francesco for their efforts in supporting me and my whole family. Finally, I'd like to thank all of my closest ones!